Multiphysics Simulation of Fission Gas Production and Release in Light Water Reactor Fuel

by

Michael Rose

A dissertation submitted in partial fulfillment
of the requirements for the degree of
Doctor of Philosophy
(Nuclear Engineering and Radiological Sciences)
in the University of Michigan
2017

Doctoral Committee:

Professor Thomas J. Downar, Chair
Professor Fei Gao
Dr. Frederick N. Gleicher, Idaho National Laboratory
Assistant Research Scientist Brendan M. Kochunas
Professor Annalisa Manera
Professor Katsuyo S. Thornton

mprose@umich.edu

ORCID iD: 0000-0003-4515-0291

ACKNOWLEDGEMENTS

I have many people to thank for helping me throughout my studies at the University of Michigan. Foremost I thank Professor Downar for giving me the opportunity to study and work at the University of Michigan, and for his dedication to and guidance in solving interesting problems.

Frederick Gleicher was my mentor at Idaho National Lab (INL); he taught me much about MOOSE and BISON, as well as C++ and finite element methods in general. He also helped me code the beginnings of Redwing. The rest of my committee; Professors Manera, Gao, Thornton, and Brendan Kochunas; gave me guidance and suggestions in developing Redwing and performing the research for this dissertation.

I owe thanks to the MPACT, MOOSE, and BISON developers who created the software platform that I used for nearly all of my research; to INL for the use of their computer clusters to obtain my results, and their extremely responsive support staff; and to Drs. Kevin Clarno and Ben Collins of Oak Ridge National Laboratory, who gave me guidance in performing multiphysics simulations.

I also owe many thanks to my officemates: Andrew Hall, Thomas Saller, and Aaron Wysocki for all of their homework help; Shane Stimpson for his help with learning MPACT and blocking my mouse laser with a sticky note; Mitchell Thomas Hellman Young for helping me to learn various and sundry things about computing; Tim Grunloh and Dan Walter for many mentally stimulating conversations, and many not; Dan Jabaay for always letting me interrupt his work; Tim Nguyen for his help with our NEUP project; and everyone else on the 4th floor of the Engineering Research Building 1 (AKA the ERB) for all of their suggestions and help.

Finally, I would like to acknowledge the generous financial support I received during my studies. This material is based upon work supported under an Integrated University Program Graduate Fellowship, which provided me funding for three years. I also received support from a Nuclear Regulatory Commission fellowship for two years.

TABLE OF CONTENTS

Acknowledgments . . . . . **ii**

List of Figures . . . . . **v**

List of Tables . . . . . **ix**

Abstract . . . . . **xi**

Chapter

1 Introduction **1**

A Background 1
A.1 MPACT 2
A.2 MOOSE and BISON 2
A.3 Redwing 3
B Original Contributions 4
C Dissertation Outline 4

2 Governing Equations and Models of the Important Physical Phenomena . . **6**

A General Governing Equations 6
A.1 Neutron Transport 6
A.2 Nuclide Inventory Evolution due to Fuel Depletion 7
A.3 Thermomechanics 9
B Governing Equations and Models for Fission Gas Behavior 11
B.1 Fission Gas Production and Transmutation in UO_2 Fuel 11
B.2 Fission Gas Migration and Release in UO_2 Fuel 15
C Further Neutronic Phenomena and Their Models 17
C.1 Resonance Shielding and Doppler Feedback 17
C.2 The Neutronic Rim Effect 18
D Further Thermomechanical Phenomena and Their Models 19
D.1 Cladding Strain 19
D.2 Fuel Strain 19
E Quantities of Interest for Evaluating Redwing 20

3 Modeling and Simulation Background **21**

A Model Domain 21

B Meshing . . . 21
B.1 MPACT . . . 21
B.2 BISON . . . 22
C Solution Methods in Individual Programs . . . 23
C.1 MPACT . . . 23
C.2 BISON . . . 24
D Data Transfer and Spatial Mapping Methods for Coupling . . . 26
D.1 MPACT to BISON: Volume-to-Point Mapping . . . 26
D.2 BISON to MPACT: Volume-to-Volume Mapping . . . 28
E Overview of Multiphysics Coupling Methods . . . 29
F Description of Coupled Depletion Algorithm in Redwing . . . 30
G Overview of Fission Gas Integral Quantities . . . 32
H Successive Fission Gas Coupling Algorithms . . . 33
I Design of Redwing for Simulating Fuel Pin Arrays . . . 42
J Validation of Redwing . . . 43

4 General Coupled Fuel Depletion Simulation Results . . . 46

A Watts Bar Nuclear 1 Single Pin Model Specifications . . . 47
B Watts Bar Nuclear 1 Single Pin Results . . . 51
B.1 Cladding Lift-off . . . 51
B.2 Cases Simulated . . . 53
B.3 Results . . . 53

5 Fission Gas Coupling Results: Single Watts Bar Fuel Pin . . . 61

A Watts Bar Fuel Pin Model Specifications . . . 62
B Constant Power Analysis . . . 62
B.1 Sensitivity Study of the Radial Fuel Mesh . . . 62
B.2 Sensitivity Study of the Redwing Time Step . . . 70
B.3 Effect of Fission Gas Coupling . . . 73
B.4 Fissionable Nuclide-Dependent Fission Gas Source in Sifgrs . . . 77
C Transient Fission Gas Release Triggered by a Reactor Shutdown . . . 85
C.1 Sensitivity Study of the Redwing Time Step . . . 86
C.2 Stability of Simulations with Shutdown . . . 87
C.3 Effect of Fission Gas Coupling . . . 91
C.4 Effect of Thermal Hydraulics Coupling . . . 96

6 Fission Gas Coupling Results: Pin Array . . . 97

7 Conclusions and Future Work . . . 102

A Conclusions . . . 102
B Future Work . . . 103

Bibliography . . . 105

LIST OF FIGURES

2.1 Transmutation and decay chains for xenon and krypton. Atoms move to the right via neutron capture, and down due to beta decay. Data are taken from the MPACT depletion library [1]; the data displayed for each nuclide are the independent fission yield fractions for ^{235}U and the half-lives. 12
2.2 Independent thermal fission yields of various elements from ^{235}U and ^{239}Pu. Vertical lines indicate Z = 36 and 54, which correspond to krypton and xenon, respectively. [2] 13
2.3 The radial profile of the total Pu concentration in three UO_2 fuel pin at the specified burnups. The markers indicate measured data and the line is a model prediction [3]. 18

3.1 Example meshes for a Redwing depletion problem. The MPACT mesh is 3D and the BISON mesh is 2D. There is a cross section of the MPACT mesh (left), a slice down the centerline of the MPACT mesh near the middle of the fuel rod (center), and the BISON mesh near the middle of the fuel rod (right). Red is fuel, gray is cladding, and light blue is coolant. Note that there is no coolant region in the BISON mesh. 23
3.2 MPACT algorithm for solving a depletion step, which advances the neutron transport and nuclide depletion solutions from time t_i to time t_{i+1}. 24
3.3 This is an illustration of mapping data fields between MPACT and BISON in both directions. It is a 2D-RZ BISON fuel pin mesh slicing through a 3D MPACT pin mesh. On the left, the BISON mesh is the thin black lines and the MPACT mesh is the heavy red lines. At the top right, a BISON node is denoted by a red X, and the large rectangle is an MPACT mesh region. At the bottom right, the MPACT mesh element is an empty rectangle and each BISON centroid is denoted by a red X. 27
3.4 Design of Redwing for runs with multiple pins; the gray boxes are parts of the program and the arrows indicate data transfer. 43
3.5 This is the rod-averaged linear power during the bump test [4]. 44
3.6 Experimental and simulated thermocouple temperature for the Risø AN3 experiment during the bump test. "FG" coupling refers to fission gas coupling. The data have been shifted so that the beginning of the ramp occurs at $t = 0$. . . 45
3.7 Experimental and simulated fractional fission gas released for the Risø AN3 experiment during the bump test. The data have been shifted so that the beginning of the ramp occurs at $t = 0$. 45

4.1 Left: the pin geometry, right: the axial details of the WBN1 single-pin model (note that this is a full assembly, but the model was a single pin) [5]. 49
4.2 Watts Bar Nuclear 1 single pin model power history 50
4.3 These are two cross sections along the centerline of the BISON mesh for a single-pin WBN1 Redwing simulation at constant power. The pin on the left is at t = 1280 days, and the pin on the right is at 1825 days. This particular model had 16 mesh elements between the centerline and fuel surface in the MPACT mesh and the maximum Redwing time step was 20 days. 52
4.4 These are the radial profiles of fission rate density and power density at the rod midplane in the fuel. This figure compares BISON (DFG0) to Redwing with one-way coupling (DFG1) and variable-κ. DFG0 uses the fast flux from the DFG1 fixed-κ case. 55
4.5 The pin-averaged κ vs. time for the case with variable κ (which is based on data from the MPACT depletion library). Also displayed is the κ value used for BISON and Redwing fixed-κ cases. 56
4.6 The net fission gas produced in two single-pin WBN1 DFG1 coupling cases. This shows the significant effect of using fixed-κ or variable-κ on the fission gas production. 56
4.7 The fast neutron flux averaged over the pin's cladding for three single-pin WBN1 cases. 57
4.8 The axially-averaged gap width for four single-pin WBN1 cases. 58
4.9 The average fuel temperature for four single-pin WBN1 cases. 59
4.10 The fission gas released as a percentage of the fission gas generated for all six single-pin WBN1 cases. 59

5.1 This is the average fuel temperature for four radial meshing cases of the WBN1 constant power simulations. The cases are reported as the number of MPACT radial mesh elements / the number of BISON radial mesh elements. 64
5.2 The axially-averaged gap width for four radial meshing cases of the WBN1 constant power simulations. 65
5.3 The maximum cladding hoop strain for four radial meshing cases of the WBN1 constant power simulations. 66
5.4 The neutron transport eigenvalue (for an infinite pin array) for four radial meshing cases of the WBN1 constant power simulations. 66
5.5 The net fission gas produced for four radial meshing cases of the WBN1 constant power simulations. 67
5.6 The fission gas released for four radial meshing cases of the WBN1 constant power simulations. 67
5.7 This is the percent fission gas relased for four radial meshing cases of the WBN1 constant power simulations. The quantity displayed is relative to the net fission gas produced. 68
5.8 The fuel fission gas inventory for four radial meshing cases of the WBN1 constant power simulations. 68
5.9 The L^2-norm (over the BISON mesh) of the power density rate-of-change for four radial meshing cases of the WBN1 constant power simulations 69

5.10 This is the percent fission gas relased for four time step cases of the WBN1 constant power simulations. The quantity displayed is relative to the net fission gas produced. 16/27 radial fuel meshing was used. 72
5.11 This is the L^2-norm of the power density rate-of-change for four time step cases of the WBN1 constant power simulations. 16/27 radial fuel meshing was used. 72
5.12 This is a comparison between coupled and decoupled fission gas cases of net fission gas generated near the end of life for the WBN1 fuel pin model. 74
5.13 This is a comparison between several plenum fission gas (FG) quantities near the end of life for the WBN1 fuel pin model: the FG released and plenum inventory for the case with coupled FG and 2 way coupling, and the FG released for 2 way coupling with decoupled FG and 1 way coupling with decoupled FG. 75
5.14 This is a comparison between coupled and decoupled fission gas cases of the L^2-norm of the power density rate-of-change for the WBN1 fuel pin model. . . 75
5.15 This is a comparison between coupled and decoupled fission gas cases of the neutron transport eigenvalue (for an infinite pin array) near the end of life for the WBN1 fuel pin model. 76
5.16 This is the decay coefficient ($\bar{\lambda}$) in Eq. (5.11) calculated from the output of Redwing and BISON simulations of a WBN1 single-pin model. The time-dependent value as well as its average are shown. 80
5.17 This is the net fission gas generated for several cases of the WBN1 simulation with constant power. "BISON nuc dep" refers to BISON simulations with a fissionable nuclide-dependent source, listed along with the decay constant. "BISON adj source" is a BISON simulation with a simple fission gas source of 0.3070 $\dot{F}$. "BISON std source" is a BISON simulation with the standard fission gas source of 0.3017 $\dot{F}$. 81
5.18 This is the fission gas released to the plenum for several cases of the WBN1 simulation with constant power. 82
5.19 This is a comparison of the average fuel temperature and the average gap width for several cases of the WBN1 simulation with constant power. On the right-hand side of the plots, the Redwing and $1.5 \cdot 10^{-9} \mathrm{s}^{-1}$ decay constant cses show the beginning of cladding lift-off. 83
5.20 This is the power history for the shutdown cases. The power percentage is relative to the average pin power in WBN1. 85
5.21 The fractional fission gas released as a percentage of net fission gas production for the single-pin shutdown case. The legend shows the Redwing time step, which was varied for the period from t = 903.5 days (i.e. immediately after the shutdown) to 960 days. 87
5.22 The L^2-norm (over the BISON mesh) of the rate of change of the power density for the single-pin shutdown case with equilibrium Xe treatment. The legend shows the Redwing time step immediately after the shutdown. 88
5.23 The L^2-norm (over the BISON mesh) of the power density rate of change for the single-pin shutdown case with transient Xe treatment. The legend shows the Redwing time step immediately after the shutdown. 89

5.24 The maximum temperature evolution for the single-pin shutdown case with equilibrium Xe treatment. The legend shows the Redwing time step immediately after the shutdown. 89
5.25 The maximum temperature evolution for the single-pin shutdown case with transient Xe treatment. The legend shows the Redwing time step immediately after the shutdown. 90
5.26 This is a comparison of the percent fission gas released between equilibrium and transient Xe treatments. 91
5.27 The L^2-norm (over the BISON mesh) of the power density rate of change for the single-pin shutdown case. The legend shows the coupling methods for each case: one-way (MPACT to BISON), two-way with decoupled fission gas, and two-way with coupled fission gas. 93
5.28 The fractional fission gas released as a percentage of net fission gas production for the single-pin shutdown case. The legend shows the coupling methods for each case: one-way (MPACT to BISON), two-way with decoupled fission gas, and two-way with coupled fission gas. 93
5.29 The average fuel temperature for the single-pin shutdown cases. The legend shows the coupling methods for each case: one-way (MPACT to BISON), two-way with decoupled fission gas, and two-way with coupled fission gas. . . 95
5.30 The neutron transport eigenvalue for the single-pin shutdown cases. The legend shows the coupling methods for each case: one-way (MPACT to BISON), two-way with decoupled fission gas, and two-way with coupled fission gas. . . 95
5.31 The L^2-norm (over the BISON mesh) of the power density rate of change for the single-pin shutdown case. Both cases had two-way coupling with fission gas coupled; one had prescribed TH and one had coupled TH. 96

6.1 A cutaway view of the midplane of the pin array model. Red is fuel, blue is moderator, gray is Zircaloy, and white is helium in the fuel/cladding gap. Reflective boundary conditions for neutron transport were set on all four sides of the domain. 98
6.2 The neutron transport eigenvalue (k_{eff}) for the pin array problem, comparing coupled and decoupled fission gas results. 100
6.3 This is a comparison of the hottest and coldest pin powers for the pin array simulation; fission gas coupling had an insignificant effect on the pin power distribution. 100
6.4 This is a comparison between coupled and decoupled fission gas cases of the plenum fission gas inventory for the pin array simulation; results for the hottest and coldest pins are shown. 101

LIST OF TABLES

2.1 Thermal fission yield percentages for ^{134}Xe, ^{135}I, ^{135}Xe from important fissionable nuclides . . . 13

4.1 Labels for Redwing Coupling Cases . . . 46
4.2 Code versions used for this chapter . . . 47
4.3 Watts Bar Nuclear 1 single pin model specifications . . . 48
4.4 Mesh and time discretization for the single-pin Watts Bar model . . . 51

5.1 Labels for Redwing Coupling Cases . . . 61
5.2 Mesh and time discretization for the single-pin Watts Bar base case . . . 62
5.3 Number of radial mesh elements in fuel for the Watts Bar fuel pin model . . . 63
5.4 Wall times for radial mesh sensitivity study run on one Fission node . . . 63
5.5 Relative differences in quantities of interest and absolute difference in k_{eff} compared to the most refined case at t = 1280 days for the MPACT/BISON radial mesh sensitivity study . . . 70
5.6 Wall times for time step sensitivity study using one Fission node . . . 70
5.7 Relative differences in quantities of interest and absolute difference in k_{eff} compared to the most refined case for the time step sensitivity study . . . 71
5.8 Relative differences in quantities of interest and absolute difference in k_{eff} caused by fission gas coupling at t = 1280 days. . . . 73
5.9 Relative differences in quantities of interest of WBN1 simulations at 4.3 years of burnup compared to BISON with a standard fission gas source of 0.3017 $\dot{F}$; the abbreviations for the other simulations are: "RW fix-κ" for the Redwing with fixed κ, "adj src" for BISON with an adjusted source of 0.3070 $\dot{F}$, and "FNDS" for BISON with a fissionable nuclide-dependent source with two decay constants. . . . 84
5.10 Relative differences in quantities of interest of WBN1 simulations at 5.5 years of burnup compared to BISON with a standard fission gas source of 0.3017 $\dot{F}$. 84
5.11 Wall times for post-shutdown time step sensitivity study using one Fission node 86
5.12 Relative differences in quantities of interest and absolute difference in k_{eff} for post-shutdown time step sensitivity study at t = 1103.5 days. . . . 86
5.13 Relative differences in quantities of interest and absolute difference in k_{eff} caused by fission gas coupling at t = 1103.5 days. . . . 92

6.1 Wall times for pin array simulations using five Fission nodes . . . 97

6.2 Relative differences in quantities of interest and absolute difference in k_{eff} for the hottest pin in the array caused by fission gas coupling 99

ABSTRACT

Along with a recent trend in nuclear engineering of coupling codes to perform high-fidelity, multiphysics simulations, the MOOSE application Redwing was developed to couple the neutron transport and core simulator MPACT and the fuel performance program BISON in order to simulate light water reactor (LWR) fuel pins. Redwing enables two-way data transfer of intrapin fields such as power density and temperature in order to improve the prediction of fission gas release and the overall accuracy of the simulation. An original algorithm was developed to enable transfer of fission gas data between MPACT and BISON, referred to as fission gas coupling. A fuel pin model based on the Watts Bar Nuclear 1 reactor was created, and several aspects of the model were studied: radial mesh and time step sensitivity, the effect of fission gas coupling on a single pin at constant power, and the effect of fission gas coupling on a fuel pin array that undergoes a shutdown. The results show that fission gas coupling has a significant effect on the solution for fuel pins at high power and high burnup, causing an approximate 9% increase in fission gas released to the plenum. It was hypothesized that changes in output quantities of interest (QOIs) were mainly due to a change in the fission gas source. So, a fissionable nuclide-dependent fission gas source was implemented in the Sifgrs module of BISON to test this; results showed some improvement in QOIs compared to standard BISON simulations. Although the fissionable nuclide-dependent source did not have the same effects as enabling fission gas coupling

in Redwing, results showed that improving the fission gas source prescription for BISON can capture some effects of fission gas coupling. The fissionable nuclide-dependent source requires further study to validate it. Apart from fission gas coupling, this research illustrated a few little-discussed ways that coupling neutron transport, nuclide depletion, and fuel performance simulations can effect QOIs usually associated with fuel performance. For one, capturing the time dependence of the recoverable energy released per fission has a significant effect on several QOIs in high-burnup fuel. Another important physical quantity derived from the neutron transport solution is the fast neutron flux in the cladding, which has a large effect on cladding creep rate.

CHAPTER 1

Introduction

A Background

Energy production in nuclear reactors is a result of free neutrons fissioning heavy metal nuclei in the fuel. The most fundamental aspect of reactor modeling and simulation is to predict the behavior of free neutrons, which is described by the Boltzmann transport equation. However, it is important to capture many other physical phenomena in order to perform a physically accurate simulation of a reactor: fuel depletion, fuel chemistry, thermal fluids, solid heat conduction and structural mechanics, etc. Therefore nuclear reactor modeling and simulation requires a multi-disciplinary analysis. The traditional approach to nuclear reactor modeling and simulation is to develop programs to simulate each relevant physics component separately. This has generally required the use of conservatisms in the calculation to account for limitations in the model fidelity and the approximate treatment of feedback effects.

Over the past few decades, there has been a trend to combine physical models or to couple programs into a single program in order to simulate multiple physical phenomena simultaneously (i.e. multiphysics). For example, neutron transport and fuel depletion models have already been combined in validated programs, such as DeCART [6] and MPACT [7,8]. This makes it possible to obtain more physically accurate solutions to fuel depletion problems. Currently, work is underway at multiple institutions to couple neutron transport, fuel depletion, and fuel performance (i.e. fuel thermomechanics and various related phenomena); examples include this work, Idaho National Laboratory's (INL's) Rattlesnake and BISON coupled via MAMMOTH [9], and the Virtual Environment for Reactor Applications (VERA) software, developed by the DOE Consortium for Advanced Simulation of LWRs (CASL) Hub [10].

Because considerable effort has been invested in developing and validating existing software packages, researchers are developing methods to couple these software packages,

rather than writing entirely new software. Unfortunately, the component programs generally employ very different spatial meshes, time discretization, and solution methods (there are some exceptions, such as INL's Rattlesnake/BISON software package, which can run simulations with a single spatial mesh). Therefore, component programs may require extensive changes in order to use them in a coupled, multiphysics framework. The work for this dissertation is concerned with coupling the programs MPACT and BISON in order to obtain multiphysics solutions for LWR fuel simulations.

A.1 MPACT

The Michigan PArallel Characteristics-based Transport (MPACT) software package, is a three-dimensional (3D) neutron transport and core analysis program [7, 8]. The development of MPACT began at the University of Michigan (UM) and is now under the joint development of Oak Ridge National Laboratory (ORNL) and UM as part of the DOE CASL Simulation Hub. It was designed to perform high-fidelity light water reactor (LWR) fuel cycle simulations via whole-core pin-resolved solutions to the integral Boltzmann transport equation. The integral transport simulation is usually obtained from the method of characteristics (MOC). MPACT has options to perform 2D or 3D MOC calculations. For the purposes of this research, 2D MOC calculations are employed. Still, a 3D model may be simulated with 2D MOC by employing the 2D-1D method, in which multiple 2D MOC solutions are coupled to a 1D axial neutron diffusion solver [11].

A.2 MOOSE and BISON

The fuel performance program BISON [12] is a MOOSE application based on the finite element method. INL's Multiphysics Object-Oriented Simulation Environment, or MOOSE, is a parallel computational framework designed to solve systems of coupled, nonlinear partial differential equations (PDEs) [13]. MOOSE and all its applications use the finite element method along with the Jacobian-free Newton-Krylov method. Multiphysics simulations with MOOSE or MOOSE applications may be anywhere from loosely- to fully-coupled, and they may use explicit or implicit time integration.

The BISON program is a MOOSE application designed for fuel performance simulations [12]. BISON is used to simulate coupled multiphysics and multiscale fuel behavior, for either 2D axisymmetric and 3D geometries. Although BISON is mostly used to simulate individual LWR fuel rods, which is the focus of this work, there has also been significant effort in validating this software for TRISO-coated fuel particles. The LWR fuel rod model can be either a smeared column or a stack of individual fuel pellets with explicit

dishes and chamfers.

BISON can employ many engineering-scale physical models in a single simulation of a fuel rod, although the user may choose to forego many of the models. BISON solves equations for the temperature and displacement fields, which mutually depend upon many auxiliary models. Fuel models include temperature- and burnup-dependent thermal properties, fission product swelling, densification, thermal and irradiation creep, fracture, and fission gas production and release; cladding models include plasticity, irradiation growth, and thermal and irradiation creep. There are also models which pertain to pellet-clad interaction: gap heat transfer, mechanical contact, and the evolution of fuel-cladding plenum pressure and volume, gas temperature, and fission gas release [14].

A.3 Redwing

Redwing is a MOOSE-based application developed at the University of Michigan as part of the work for this dissertation; it enables coupling between MPACT and BISON. Development of Redwing began in May of 2013 at Idaho National Laboratory as a collaboration between me and Frederick Gleicher, and after November of 2013 I became the sole developer. A Redwing depletion simulation potentially includes many physical phenomena; nearly all of the relevant theory is already contained in the theory manuals for MPACT [8] and BISON [15]. Redwing is currently under active development; beside the source code, the Redwing repository also includes example problems, regression tests, and a user's manual.

Redwing simulates the depletion of single fuel pins or small rectangular arrays of fuel pins. Redwing couples the solutions on the MPACT and BISON meshes by mapping and transferring spatially-dependent data fields via function and subroutine calls. An operator split method is used to couple the MPACT and BISON solutions. In most Redwing simulations, the MPACT to BISON data transfers include fission rate density, power density, and fast neutron flux. The BISON to MPACT data transfer includes temperature in any region of the fuel pin and an axially-dependent coolant density for each fuel pin. Along with these data transfers, fission gas coupling may be enabled, which entails two-way exchange of density fields of certain xenon and krypton nuclides. Enabling the transfer of additional data fields is also planned; these fields include burnup, density, and potentially others. Details of the coupled solution algorithm may be found in Chapter 2.

Redwing has a limited capability to parallelize a simulation with MPI, by decomposing the MPACT domain by space and angle in MPACT. MPACT and BISON have extensive options for parallelization with MPI and OpenMP. Like all MOOSE applications, Redwing

can be run with 2D RZ or 3D BISON meshes of each fuel pin. Each fuel pin in the MPACT domain can exchange data with a separate BISON fuel pin, all in a single coupled run; this is enabled by MultiApps and Transfers, two MOOSE data structures.

B Original Contributions

A software package named Redwing was created to couple MPACT [7, 8] and BISON [12] for LWR fuel depletion simulations with two-way data transfer. Redwing provides the foundation for the research described in this dissertation. There are a few original aspects of the coupling of MPACT and BISON that will be explained in the following chapters.

One of the important physical fields in the solution of fuel depletion problems is the fission gas distribution. Both MPACT and BISON calculate a distribution of fission gas in the fuel. By properly exchanging fission gas data between the two programs, one may obtain a combined neutronics and thermomechanics solution with consistent fission gas distributions on each program's mesh; this more accurate fission gas distribution means that the overall coupled solution is more accurate (i.e. not only the fission gas release prediction). The primary original contribution of this research was to provide the fuel performance program with a full physics, detailed spatial prediction of fission gas isotopics during fuel depletion and to enable the movement of fission gas in the neutronics program according to BISON's fission gas release model. Throughout this document, this will be referred to as fission gas coupling. Additionally, results suggested that much of the discrepancy between BISON and Redwing in the fission gas release prediction may be eliminated by prescribing a fission gas source that is linearly dependent on the fission density rates of the main fissionable nuclides. This is referred to as a fissionable nuclide-dependent source, and was implemented in BISON as a code patch. It is a seconday contribution of this research.

Furthermore, this research has shown that certain parameters, such as the energy released per fissioning atom (κ), are significant for coupled neutronics and thermomechanics simulations of nuclear fuel. This work has demonstrated that κ has significant effects on the solution to the fuel performance problem; the difference in the MPACT and BISON developer's assumed value(s) of κ is enough to cause significant changes in the solution.

C Dissertation Outline

Chapter 2 provides background information on the governing equations of neutron transport and fuel performance. Chapter 3 goes over details of modeling and simulation with

Redwing, including meshing, data transfer, and coupling algorithms. Chapter 4 shows general results from PWR fuel depletion simulations with BISON and coupled MPACT and BISON; none of these results were obtained with fission gas coupling. Chapter 4 delves into the details of the fission gas coupling algorithm developed for this dissertation. Chapter 5 shows Redwing results for a single fuel pin problem with fission gas coupling, along with BISON results obtained with a fissionble nuclide-dependent fission gas source. Chapter 6 presents results for an array of single pins. Chapter 7 details the conclusions and suggested future work.

CHAPTER 2

Governing Equations and Models of the Important Physical Phenomena

A General Governing Equations

A.1 Neutron Transport

For steady-state and depletion simulations, MPACT approximately solves the eigenvalue form of the Boltzmann transport equation [16]:

$$\hat{\mathbf{\Omega}} \cdot \nabla \psi(\mathbf{r}, \hat{\mathbf{\Omega}}, E) + \Sigma_{\mathrm{t}}(\mathbf{r}, E, T)\psi(\mathbf{r}, \hat{\mathbf{\Omega}}, E) = \int_{4\pi} d\Omega' \int_0^\infty dE' \Sigma_{\mathrm{s}}(\mathbf{r}, \hat{\mathbf{\Omega}}' \cdot \hat{\mathbf{\Omega}}, E' \rightarrow E, T)\psi(\mathbf{r}, \hat{\mathbf{\Omega}}', E') + \frac{\chi(\mathbf{r}, E)}{4\pi k_{\mathrm{eff}}} \int_{4\pi} d\Omega' \int_0^\infty dE' \nu(\mathbf{r}, E')\Sigma_{\mathrm{f}}(\mathbf{r}, E', T)\psi(\mathbf{r}, \hat{\mathbf{\Omega}}', E'), \tag{2.1a}$$

with the specified boundary conditions:

$$\psi(\mathbf{r}, \hat{\mathbf{\Omega}}, E) = 0 \quad \text{for} \quad \mathbf{r} \in \partial\mathcal{D}, \quad \hat{\mathbf{\Omega}}' \cdot \hat{\mathbf{\Omega}} < 0, \quad E > 0. \tag{2.1b}$$

This equation is used to solve for the angular neutron flux, $\psi(\mathbf{r}, \hat{\mathbf{\Omega}}, E)$, and the neutron transport eigenvalue, k_{eff}. The independent variables are: $\mathbf{r}$, the spatial position; $\hat{\mathbf{\Omega}}$, the direction of neutron flight; and E, the neutron energy. The coefficients of $\psi(\mathbf{r}, \hat{\mathbf{\Omega}}, E)$ are macroscopic neutron cross sections: $\Sigma_t(\mathbf{r}, E)$ is the total cross section, $\Sigma_s(\mathbf{r}, \hat{\mathbf{\Omega}}' \cdot \hat{\mathbf{\Omega}}, E' \rightarrow E)$ is the scattering cross section, and $\Sigma_f(\mathbf{r}, E)$ is the fission cross section. Other quantities are: $\chi(\mathbf{r}, E)$, the fission spectrum; $\nu(\mathbf{r}, E)$, the neutron yield per fission; T, the temperature, and $\mathcal{D}$, the problem domain. In order for this equation to be tractable on a computer, MPACT utilizes a discrete-ordinates and multigroup formulation of Eq. (2.1). In the context of

this work, MPACT solves an axially-intergrated transport equation using 2D MOC; the planar 2D MOC solution fields are coupled via a 3D coarse mesh finite difference (CMFD) solution [8].

The angular neutron flux may be integrated over all directions of neutron flight to obtain the scalar neutron flux, as shown in Eq. (2.2):

$$\phi(\mathbf{r}, E) = \int_{4\pi} d\Omega' \, \psi(\mathbf{r}, \hat{\mathbf{\Omega}}, E). \tag{2.2}$$

A.2 Nuclide Inventory Evolution due to Fuel Depletion

As a nuclear reactor operates, the fuel slowly depletes. Neutron absorption, fissions of heavy metal atoms, and subsequent decays of fission products cause the nuclide inventory of the fuel to slowly evolve as it depletes. The evolution of the nuclide inventory is modeled with the nuclide depletion equations. These equations are also known as the nuclide transmutation equations. The solution to these equations is a space- and time-dependent vector of nuclide number densities. Eqs. (2.3) are the nuclide depletion equations [17]:

$$\begin{aligned}\frac{\partial N_i(\mathbf{r},t)}{\partial t} = &\sum_{j=1}^{N_{\text{nuc}}} l_{ij}\lambda_j N_j(\mathbf{r},t) + \bar{\phi}(\mathbf{r},t)\sigma_{\text{a},i-1}(\mathbf{r},t)N_{i-1}(\mathbf{r},t) + \bar{\phi}(\mathbf{r},t)\sum_{j=1}^{N_{\text{nuc}}} y_{ij}\sigma_{\text{f},j}(\mathbf{r},t)N_j(\mathbf{r},t) \\ &- (\lambda_i + \bar{\phi}(\mathbf{r},t)\sigma_{\text{a},i}(\mathbf{r},t))N_i(\mathbf{r},t) + M_i(N_i,\mathbf{r},t) \quad (i = 1,...,N_{\text{nuc}}),\end{aligned} \tag{2.3}$$

where

$N_i(t) \equiv$ number density of nuclide i,

$\lambda_i \equiv$ radioactive decay constant for nuclide i,

$\sigma_{\text{a},i} \equiv$ one-group (i.e. condensed) neutron absorption cross section of nuclide i,

$\sigma_{\text{f},i} \equiv$ one-group neutron absorption cross section of nuclide i,

$\bar{\phi} \equiv$ one-group neutron scalar flux,

$l_{ij} \equiv$ the fraction of radioactive decays by nuclide j which lead to the birth of nuclide i,

$y_{ij} \equiv$ the fission yield, or the fraction of fissions of nuclide j which lead to the the birth of nuclide i,

$M_i \equiv$ the net migration rate of nuclide i into a given region of the fuel, and

$N_{\text{nuc}} \equiv$ the number of nuclides.

The cross sections are condensed to one group and the scalar flux $\bar{\phi}$ is integrated over all energy groups. In the context of reactor depletion, the one-group flux and condensed cross sections are time- and space-dependent, because they depend on the flux spectrum in the fuel; however, they are written without time dependence due to the quasi-static approximation used in MPACT. When Eqs. (2.3) are solved in MPACT, the flux and cross sections are assumed to be constant. Because this would be a poor assumption throughout an entire fuel cycle, Eqs. (2.3) are solved in steps (e.g. one step is 30 days), along with the neutron transport equation. To increase the accuracy of the overall MPACT solution, the neutron transport equation and the nuclide depletion equations are coupled via the predictor-corrector method, such that each set of equations is solved twice per depletion step.

The nuclide depletion equations may be augmented by adding a heterogeneous term, M_i, which describes the migration of atoms throughout the nuclear fuel. In the high-temperature and high-radiation environment of nuclear fuel, many atoms migrate over time. The migration of an atom may be the result of a number of physical phenomena, including thermal diffusion, gradients in the oxygen-to-uranium ratio, pore migration, or collisions with energetic fission products. For atoms of nuclide i migrating via thermal diffusion, M_i would be described by Fick's second law:

$$M_i = \nabla \cdot D_i \nabla N_i \tag{2.4}$$

where D_i is the nuclide diffusion coefficient, which depends on the temperature and composition of the fuel. This can explain the behavior of several fission product species. For many migrating nuclides, M_i is a more complex, nonlinear term.

Eqs. (2.3) may be expressed in matrix notation:

$$\frac{\mathrm{d}\mathbf{N}}{\mathrm{d}t} = A\mathbf{N} + \mathbf{M} \tag{2.5}$$

where A is a square matrix with a row corresponding to each nuclide. These will be referred to as the augmented nuclide depletion equations. The normal nuclide depletion equations do not include the heterogeneous term, so they would be expressed as:

$$\frac{\mathrm{d}\mathbf{N}}{\mathrm{d}t} = A\mathbf{N} \tag{2.6}$$

Most reactor depletion codes (e.g. MPACT) solve the normal nuclide depletion equations, without consideration of nuclide migration in space. This allows for a simpler solution method. It is also important to consider the linearity of the nuclide depletion equations. In many reactor depletion codes, including MPACT with the quasi-static assumption,

Eqs. (2.6) are linear; however, if the neutron flux and nuclide number densities are both considered to be parts of the solution, then these are nonlinear equations, even without the migration term. A nonlinear migration term is also possible for nuclides whose migration cannot be modeled as simple diffusion.

Eq. (2.1) is an eigenvalue equation, so the solution, the neutron flux, may be scaled arbitrarily. However, Eqs. (2.3) require a neutron flux value that is scaled to the proper power level for the entire domain $\mathcal{D}$ (e.g. a single fuel pin, a fuel assembly, or a reactor). The formula which can be used to relate the scalar neutron flux to a given power level, P, is Eq. (2.7):

$$P = \int_{\mathcal{D}} d\mathbf{r} \int_0^\infty dE \phi(\mathbf{r}, E) \sum_{i=1}^{N_{\text{nuc}}} \kappa_i \Sigma_{\text{f},i}(\mathbf{r}, E, T). \tag{2.7}$$

The power level is an input quantity in reactor depletion simulations, hence a domain-wide scaling factor for the scalar neutron flux may be obtained from this equation. κ_i is the recoverable energy released per fission, which is dependent on the fissioning nuclide. This quantitiy is difficult to quantify exactly because it depends on the reactor configuration. As a rule of thumb, this quantity is about 200 MeV per fission for all fissionable nuclides [16]. In the context of this research, small differences in κ_i can be significant; this will be explained later.

A.3 Thermomechanics

Heat transfer and solid mechanics phenomena have strong mutual influence in nuclear fuel, so they are usually treated together as thermomechanics. The solution to a heat transfer problem is the temperature field, and the solution to a solid mechanics problem is the displacement (i.e. displacement of an infinitesimal piece of the fuel or cladding) field. In a thermomechanics simulation, the influence of the temperature on the solid mechanics and the influence of the displacement on the heat transfer must both be resolved in order to obtain the correct overall solution. The thermomechanics solution may be though of as a vector that combines the heat transfer and solid mechanics solutions, as shown in Eq. (2.8). Most BISON models include the assumption of symmetry about a z-axis along the fuel centerline, so the solution depends on the radial coordinate r and the axial coordinate z; this is known as an axisymmetric model or cylindrical geometry.

$$\mathbf{T}(r,z,t) = \begin{bmatrix} T(r,z,t) \\ u_r(r,z,t) \\ u_z(r,z,t) \end{bmatrix} \tag{2.8}$$

where

$$\begin{aligned} T(r,z,t) &\equiv \text{The temperature field} \\ u_r(r,z,t) &\equiv \text{The radial displacement field} \\ u_z(r,z,t) &\equiv \text{The axial displacement field} \end{aligned} \tag{2.9}$$

The equation that provides the temperature solution is the heat equation, Eq. (2.10), in which the dependence of T on r, z, and t are implied [15].

$$\rho(T,\mathbf{u})c_p(T)\frac{\partial T}{\partial t} - \nabla \cdot k(T)\nabla T - q''' = 0 \tag{2.10}$$

where $\mathbf{u}$ is the displacement field, $\rho(T,\mathbf{u})$ is the density, $c_p(T)$ is the specific heat capacity, $k(T)$ is the thermal conductivity. Many of the coefficients of this equation depend on temperature, making heat transport a nonlinear problem. Displacement of the material can result in a change in density at a point as well as changes the shape of the problem domain, which is not reflected in Eq. (2.10).

The principal equation for the mechanics portion of the solution is Cauchy's equation, Eq. (2.11), which is basically a statement that the system is in static equilibrium [15]. The Cauchy stress tensor S is the solution to this equation.

$$\nabla \cdot S + \rho\mathbf{f} = \mathbf{0} \tag{2.11}$$

Note that this equation does not include the displacement field, which is one of the solution variables to the thermomechanics problem. The displacement field is related to the strain tensor by Eq. (2.12), where $\nabla_{\mathbf{X}}$ is the gradient operator with respect to the material coordinates and superscript T is the transpose operator.

$$\epsilon = \frac{1}{2}\left[\nabla_{\mathbf{X}}\mathbf{u} + (\nabla_{\mathbf{X}}\mathbf{u})^T + (\nabla_{\mathbf{X}}\mathbf{u})^T \cdot \nabla_{\mathbf{X}}\mathbf{u}\right] \tag{2.12}$$

If it is possible to assume that only infinitesimal strains occur, Eq. (2.12) may be simplified; the nonlinear term can be neglected, and the gradients defined in spatial and material coordinates become indistinct, so the subscript $\mathbf{X}$ can be dropped. So, the relationship between

the displacement field and the strain tensor can be expressed as in Eq. (2.13).

$$\epsilon = \frac{1}{2}\left[\nabla \mathbf{u} + (\nabla \mathbf{u})^T\right] \tag{2.13}$$

Nearly all results in this dissertation are from simulations using finite strain mechanics. Also, the strain tensor yielded by Eq. (2.13) or Eq. (2.12) must be modified to account for strains due to thermal expansion, fuel densification, and irradiation swelling and growth.

The relationship between strain and stress is complicated if plastic deformation occurs during a simulation. In this case, the approach taken in BISON is to compute the Cauchy stress tensor increment for a time step, which is a function of the strain increment for the time step, the modulus of elasticity $E(T)$, the shear modulus $\mu(T)$, and a few plasticity parameters expressed as a vector $\mathbf{p}(T)$; this functional relationship is shown in Eq. (2.14).

$$\Delta S = f(\Delta\epsilon, E(T), \mu(T), \mathbf{p}(T)) \tag{2.14}$$

If no plastic deformation occurs, then linear elasticity may be assumed; this means that there is a linear relationship between the Cauchy stress tensor and the strain tensor, as shown in Eq. (2.15).

$$S = E(T)\epsilon \tag{2.15}$$

Like with Eq. (2.10), these equations have many dependencies on temperature, demonstrating the coupling of solid mechanics and heat transfer.

B Governing Equations and Models for Fission Gas Behavior

Fission gas is usually taken to mean the noble gases xenon and krypton, but it may also include rubidium and cesium [18]. Any xenon or krypton nuclides may be considered fission gas; the most important nuclides are ^{131}Xe-^{136}Xe and ^{83}Kr-^{86}Kr [19]; and the MPACT depletion libraries contain a wider range of nuclides: ^{128}Xe-^{137}Xe and ^{80}Kr-^{88}Kr [1], some of which are quite short-lived.

B.1 Fission Gas Production and Transmutation in UO_2 Fuel

Like other fission products, fission gas production and transmutation is governed by the nuclide depletion equations, Eqs. (2.3). Fission gas nuclides of the same element may be thought of as chains, where a fission gas atom moves through the chain by absorbing a

free neutron. To illustrate the important fission gas nuclides, relevant data were extracted from the MPACT depletion library [1] and arranged in transmutation chains, shown in Fig. 2.1. Some precursor nuclides of bromine, tellurium, and iodine are included in the chains because they may transmutate into fission gas nuclides via beta decay. Note that some fission product nuclides do not appear in Fig. 2.1 because they have been lumped with their daughters; to lump a nuclide i with its daughter means to add the independent fission yield fraction of i to that of its daughter and then set yield fraction of n to zero. This effectively means any atoms of nuclide i created by fission instantly decay to the daughter nuclide; for example, ^{133}I does not appear because it is lumped with ^{133}Xe. Generally, a fission product which has a small effect on reactivity and a half-life of less than a day may be lumped with its daughter.

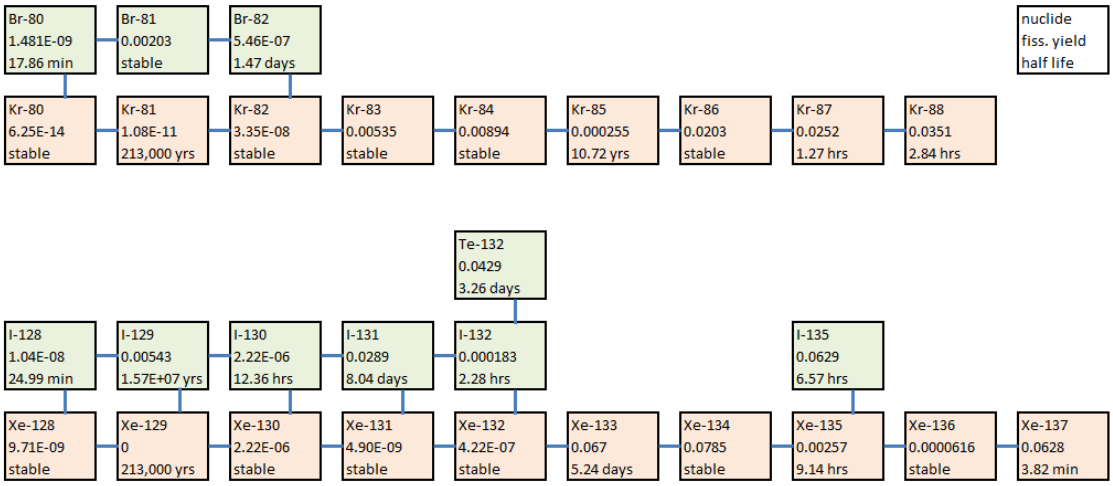

Figure 2.1: Transmutation and decay chains for xenon and krypton. Atoms move to the right via neutron capture, and down due to beta decay. Data are taken from the MPACT depletion library [1]; the data displayed for each nuclide are the independent fission yield fractions for ^{235}U and the half-lives.

Fission gas nuclides are a common fission product. In general, about 30% of fissions in LWR fuel directly result in the birth of a fission gas atom. Throughout the life of LWR fuel, most of the fissioning atoms are either ^{235}U or ^{239}Pu. There are significant differences in the yields of fission gas nuclides from these two fissile nuclides; Fig. 2.2 shows the fission yield vs. atomic number (Z) for thermal fission of ^{235}U and ^{239}Pu. Other nuclides which contribute significantly the total number of fissions are ^{238}U, ^{240}Pu, ^{241}Pu, and ^{242}Pu. To further demonstrate how yields differ among fissioning nuclides, Table 2.1 lists the fission yields of ^{134}Xe, ^{135}I, ^{135}Xe. This table also shows how fission yields can be quite different for daughter nuclei which differ by only one nucleon.

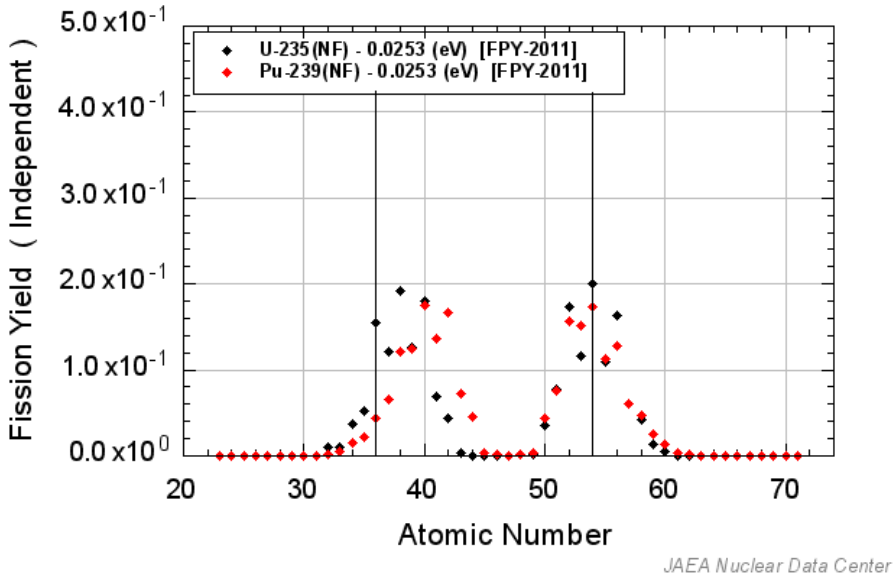

Figure 2.2: Independent thermal fission yields of various elements from ^{235}U and ^{239}Pu. Vertical lines indicate Z = 36 and 54, which correspond to krypton and xenon, respectively. [2]

Table 2.1: Thermal fission yield percentages for ^{134}Xe, ^{135}I, ^{135}Xe from important fissionable nuclides

Fission gas nuclide	^{235}U	^{238}U	^{239}Pu	^{240}Pu	^{241}Pu	^{242}Pu
^{134}Xe	7.8487	7.4584	7.6646	7.6103	7.8815	7.3862
^{135}I	6.2887	7.0150	6.5468	6.7358	6.9542	7.4257
^{135}Xe	0.2566	0.0269	1.0664	0.5002	0.2269	0.1058

In MPACT, Eqs. (2.3) (minus the migration term) are solved with a high-order time integration method. So, MPACT provides a highly accurate solution for fission gas production and transmutation, as long as fission gas migration is insignificant. Due to the importance of ^{135}Xe in reactor operations, MPACT provides a special treatment called equilibrium xenon. When the equilibrium xenon treatment is used, the ^{135}Xe concentration yielded by the nuclide depletion solver is overwritten by the equilibrium value. The ^{135}Xe equilibrium concentration is determined by the neutron flux; this concentration is obtained after each flux calculation by solving the ^{135}I-^{135}Xe decay chain. The equations for the equilibrium values may be found in Duderstadt and Hamilton [16]. One advantage of equilibrium xenon is that it tends to stabilize the coupled neutron transport and neutron depletion problem [20]. If ^{135}Xe is treated like the other nuclides, it is referred to as transient xenon.

The current method for treating fission gas behavior in BISON is the Simple Integrated

Fission Gas Release and Swelling (Sifgrs) model [15, 21]. In Sifgrs, fission gas is treated in a lumped fashion, so that the number densities of the individual nuclides are not tracked. Another simplification is that no distinction if made between production of gas from fission and the destruction of these gases via transmutation and decay; instead, Sifgrs only has a prescription for the net production rate resulting from all of these phenomena. In the case of ^{135}Xe, for example, the destruction rate is high due to the high absortion cross section, and ^{135}Xe atoms tend to reach an equilibrium concentration about two days after a change in the reactor power level. In contrast, Sifgrs assumes that fission gas builds up steadily over time.

The net fission gas production rate prescription in Sifgrs was taken from the FALCON code [22], which contains several fission gas release models. One of the more accurate models is the Forsberg-Massih model [23]; this model relies on an empirical formula for the production rate of stable fission gas nuclides, Eq. (2.16), originally published by White and Tucker in 1983 [24].

$$\beta_{stable} = 2.9 \cdot 10^{16} \left(2.606 + \frac{0.6386}{1 + \frac{375.0E}{W_{\mathrm{R}}}} \right) W_{\mathrm{R}} \tag{2.16}$$

where

$$\beta_{stable} \equiv \text{the production rate of stable fission gas nuclides} \left[\frac{\text{FG atoms}}{\text{m}^3\text{s}} \right]$$

$$E \equiv \text{the fractional enrichment of } UO_2$$

$$W_{\mathrm{R}} \equiv \text{the power per unit mass of fuel} \left[\frac{\text{W}}{\text{g}} \right]$$

Eq. (2.16) is simplified in a few steps to obtain the net fission gas production rate, β, used in FALCON and Sifgrs. First, E is set to 0.03, which is valid because β_{stable} depends weakly on E for low-enriched fuel. Second, the dependence on W_{R} is replaced with a dependence on fission rate density $\dot{F}$, although the literature [24] does not explicitly show how this is done. Lastly, the fractional yield of fission gas atoms (i.e. the factor in front of $\dot{F}$) is adjusted upward slightly to account for unstable fission gas nuclides. These simplifications result in Eq. (2.17).

$$\beta = 0.3017\dot{F} \tag{2.17}$$

Eq. (2.17) provides a fairly accurate prediction of the net fission gas production rate; however, assuming a fixed yield of fission gas atoms over the lifetime of fuel is incorrect due to the changing composition of fuel with burnup.

B.2 Fission Gas Migration and Release in UO_2 Fuel

Fission gas migration in UO_2 is a complex process, but the basic migration path of the fission gas during thermal release may be described concisely. After Xe and Kr are born inside UO_2 fuel grains, they diffuse towards the surface of the fuel grains; their diffusion rates are heavily temperature-dependent, hence the name "thermal release". Xe and Kr are nearly insoluble in UO_2, so they mainly exist in nanometer-sized bubbles inside the grains. Most Xe and Kr atoms which reach the surface form intergranular gas bubbles. These gas bubbles expand over the surface of the grains, eventually coalescing and forming a tunnel network, through which gas is released to the fuel/cladding plenum [15].

At the engineering scale, the scale of the simulations in this dissertation, a diffusion model does not capture the behavior of the fission gas well, for two reasons. First, diffusion can describe fission gas migration within UO_2 grains, but because UO_2 grains are on the order of micrometers in diameter, they are considered to be below the engineering scale; tracking the diffusion of fission gas through explicitly-modeled fuel grains would be prohibitively computationally expensive. Therefore fuel grains are not explicitly modeled in BISON. Second, the fission gas travels very quickly throught the bubble tunnel network relative to other important phenomena at the engineering scale. So, the term M_i in Eq. (2.3) for fission gas cannot be modeled using Eq. (2.4), nor can it be modeled as advection without explicitly modeling the bubble tunnel network. Instead, M_i is nonlinear and does not have an analytic form. Even if the rest of the coupled problem is ignored, and only the problem expressed by Eqs. (2.3) is considered, M_i is nonlinear.

Instead of explicitly modeling the fuel grains, Sifgrs calculates the concentrations of fission gas inside grains and in grain face bubbles at each quadrature point of the BISON mesh. All fission gas starts inside fuel grains; in order to determine the amount that moves into grain-face bubbles, a single diffusion problem for an idealized spherical fuel grain is solved for each BISON mesh point. This diffusion problem represents all fuel grains in the vicinity of that mesh point. In order to solve the diffusion problem, Sifgrs tracks the spatially-dependent fuel grain radius, r_{gr}, and accesses to the local temperature at each mesh point.

Sifgrs calculates and stores a few other spatially-dependent quantities that are relevant to fission gas production and release. This includes the number of grain-face bubbles per unit grain-face area, N_{gf}, and the number of fission gas atoms per bubble, n_{g}. The surface-to-volume ratio of a fuel grain may be determined from the grain radius, as shown in Eq. (2.18):

$$\zeta = \frac{3}{r_{\mathrm{gr}}}(1 - \nu_0), \tag{2.18}$$

where ν_0 is the initial fuel porosity. These quantities can be related to the volumetric number density of fission gas atoms in fuel, as shown in Eq. (2.19):

$$\sum_{i=1}^{N_{\mathrm{FG}}} N_i = \frac{1}{2} n_{\mathrm{g}} N_{\mathrm{gf}} \zeta + N_{\mathrm{ig}} + N_{\mathrm{hbs}}, \tag{2.19}$$

where N_{FG} is the number of different fission gas nuclides, N_{ig} is the number density of intragranular fission gas atoms, and N_{hbs} is the number density of fission gas atoms in high-burnup structures. The factor of $\frac{1}{2}$ accounts for the fact that grain-face bubbles are shared by adjacent grains.

Sifgrs also calculates the fission gas release rate per unit volume. In Sifgrs, it is assumed that thermal fission gas release is controlled by grain face saturation. At each BISON mesh point, the projected area of grain-face bubbles A_{gf} is stored. A projected area is used because the bubbles are not flat. The product of N_{gf} and A_{gf} are restrained below a saturation value, F_{sat}:

$$F_{\mathrm{sat}} \geq N_{\mathrm{gf}} A_{\mathrm{gf}}. \tag{2.20}$$

If the product on the RHS is above F_{sat}, then it is assumed the bubbles have formed a tunnel network connecting the given mesh point to the fuel surface, and a certain amount of fission gas is instantly transported to the fuel/cladding plenum in order to maintain the product at F_{sat}. The rate of fission gas release which maintains the product at F_{sat} is expressed in Eq. (2.21) [19]:

$$\frac{\mathrm{d}n_{\mathrm{fgr}}}{\mathrm{d}t} = n_{\mathrm{g}} \frac{N_{\mathrm{gf}}}{A_{\mathrm{gf}}} \frac{\mathrm{d}A_{\mathrm{gf}}}{\mathrm{d}t}, \tag{2.21}$$

where n_{fgr} is the number of fission gas atoms thermally released to fuel/cladding plenum. Fission gas also undergoes athermal and transient release, the latter of which is the result of microcracking. To make a connection between the Sifgrs models and the migration term of Eq. (2.3), the rates of fission gas release due to the three mechanisms may be summed to yield the migration rate of all fission gas nuclides, which is shown in Eq. (2.22):

$$\sum_{i=1}^{N_{\mathrm{FG}}} M_i = -\frac{1}{2} \frac{\mathrm{d}n_{\mathrm{fgr}}}{\mathrm{d}t} \zeta - \dot{R}_{\mathrm{ath}} - \dot{R}_{\mathrm{tran}}, \tag{2.22}$$

where $\dot{R}_{\mathrm{ath}}$ and $\dot{R}_{\mathrm{tran}}$ are the athermal and transient fission gas release rates per unit volume. The migration rates of all fission gas nuclides must be summed on the LHS due to the lumped treatment of fission gas in Sifgrs.

An interesting consequence of the Sifgrs model is that any fuel mesh point is spatially coupled to every point in the fuel/cladding plenum, due to the assumption that released

fission gas is well-mixed. More details on the Sifgrs model may be found in the BISON theory manual and the relevant journal article [15, 21].

Fission gas release can have a significant effect on the thermomechanical behavior of the fuel rod. For one, the grain-face bubbles cause fuel swelling, which leads for fuel/-cladding gap closure and pellet-cladding mechanical interaction. Also, fission gas release causes an increase in the fuel/cladding plenum pressure as well as decrease in thermal conductivity of the gas mixture in the plenum, which has negative implications for fuel integrity.

C Further Neutronic Phenomena and Their Models

C.1 Resonance Shielding and Doppler Feedback

Energy and spatial self-shielding in fuel rods are important phenomena which affect the neutron flux field. At the fuel rod level, spatial self-shielding refers to the phenomenon of low-energy neutrons streaming from the moderator into the fuel being preferentially absorbed near the surface of the fuel, where they first encounter absorbing nuclei. Depending on the strength of the absorber, this can result in a neutron flux depression in the fuel interior. Energy self-shielding refers to the lower part of the neutron energy spectrum being shielded by absorption occuring at higher neutron energies. This occurs because almost all neutrons are born from fission at high energies, so they must scatter off of nuclei several times and avoid absorption in order to reach lower energies.

The most difficult aspect of self-shielding to accurately capture is shielding due to cross section resonances; in the resonance energy region, heavier nuclides' cross sections vary greatly with energy, which can result in a large amount of error in the multigroup approximation. When the temperature of the fuel changes, resonance shielding increases due to Doppler broadening of the resonances, and neutron absorption rates are significantly affected. Therefore, when considering changing fuel temperature due to multiphysics coupling, it is important to capture the resonance shielding effect accurately.

Special treatments are employed in reactor simulations to accurately capture the effect of resonance shielding. For this work, the subgroup method was employed, which is based on the Intermediate Resonanace Approximation [25]. Each energy group in the slowing down range is divided into subgroups, and a fixed source problem is solved for each resonance category (i.e. resonance isotope), in each subgroup. The results of the subgroup calculation are used to correct the multigroup cross sections in the resonance energy range.

C.2 The Neutronic Rim Effect

The neutronic rim effect is a large increase in the fission rate density field near the surface of the fuel (i.e. the rim region) as burnup progresses. For low-enriched fuels, the resonance in the ^{238}U absorption cross section at 6.68 eV results in significant spatial self-shielding of low energy neutrons, which results in a higher neutron flux in the rim region. As the fuel depletes, neutron capture in ^{238}U and subsequent decay results in the birth of ^{239}Pu. As this is occuring, the already existing ^{239}Pu is converted into heavier plutonium isotopes with the absorption of more neutrons [26]. These plutonium isotopes provide extra fissile material with a higher absorption cross sections than ^{235}U in the rim region (see Fig. 2.3); this results in more spatial self-shielding, which in turn results in a higher local rate of plutonium production. Hence, there is a positive feedback loop between spatial self-shielding and plutonium creation which shifts the fission rate and power density toward the surface of the fuel rod. The region of high fission rate density in the rim evolves to be typically 100-200 μm thick [18]; because this is quite small at the engineering scale, the rim effect is difficult to model.

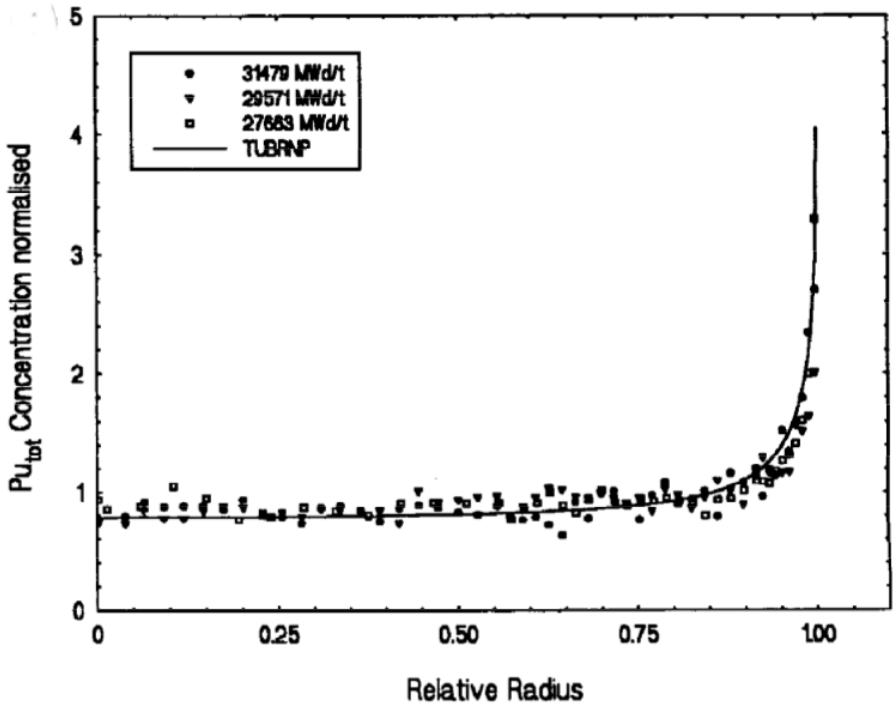

Figure 2.3: The radial profile of the total Pu concentration in three UO_2 fuel pin at the specified burnups. The markers indicate measured data and the line is a model prediction [3].

The rim effect significantly affects the thermomechanical behavior of the fuel due to the large effect that fission rate density and power density have on a number of physical

phenomenon. First of all, shifting the power density to the rim region allows heat to be rejected from the fuel rod more quickly, resulting in a lower average fuel temperature. Additionally, over time, the higher fission rate density in the rim region results in higher local burnup, which leads to locally higher swelling and lower thermal conductivity.

D Further Thermomechanical Phenomena and Their Models

D.1 Cladding Strain

Strain is a measurement of the deformation of a material due to applied stress. There are two primary causes of strain in the cladding: creep and growth. Creep is the slow, permanent deformation of a material due to stresses less than the yield stress. Cladding creep is driven by coolant pressure, and is accelerated by high temperatures and collisions between nuclei and fast neutrons. It includes primary and secondary creep. Creep results in a decrease in the inner and outer diameter of the cladding, which contributes to the closure of the fuel-cladding gap. It is a slow process, with a strain rate of only about 10^{-10}s^{-1} to 10^{-9}s^{-1}

Growth in the cladding is a volume-conserving phenemonon caused by the microscropic restructuring of Zircaloy due to irradiation; it causes lengthening in the axial direction. Growth is also a slow process, with an axial strain rate of only about 10^{-10}s^{-1}.

D.2 Fuel Strain

In the fuel rod models used in this work, there are four phenomena which result in fuel strain or displacement: thermal expansion, densification, relocation, and swelling. All four phenomena affect the timing of the fuel-cladding gap closure. Thermal expansion happens instantaneously and is a function of the temperature. Fuel densification is a function of both burnup and temperature; BISON uses the ESCORE empirical model to compute fuel densification [22].

In this work, fuel densification is complete at 5 MWD/kgHM. Throughout the beginning of fuel life, up to a burnup of about 18 MWD/kgHM, the fuel undergoes relocation. This refers to the radial strain in the fuel caused by radial cracking. In this work, another ESCORE empirical model is used to calculate the relocation strain without explicitly modeling cracks in the fuel. Lastly, there is the phenomenon of swelling, which has the greatest effect by the end fo fuel life. Swelling is caused by the buildup of gaseous and solid fission

products, and leads to a steady increase in fuel volume after densification is complete; by the end of fuel rod life, swelling can cause the fuel volume to increase by 3-4% [27].

E Quantities of Interest for Evaluating Redwing

The coupled simulations performed in this dissertation have a large amount of data which can be considered part of the solution: there are many spatially-dependent quantities, as well as quantities which come from spatial integrals or averages over the fuel or cladding. Most of the analysis is focused on spatial integrals or averages, in order to more easily draw conclusions. Henceforth, these will be referred to as quantities of interest (QOIs). Because the main contribution of this dissertation is a novel fission gas coupling method, there are several fission gas-related QOIs, including some which are indistinct in BISON simulations.

- Net fission gas production (i.e. fission gas produced minus that which decays in fuel)
- Fuel fission gas inventory
- Fission gas released to the plenum
- Fission gas inventory in plenum
- Average gap width

Other QOIs examined in this work are those which are important to nuclear reactor operation and safety. Many of these quantities are outlined in the Nuclear Regulatory Commission's Standard Review Plan document [28]. These quantities include:

- k_{eff}
- The maximum fuel temperature, which is one of the main indicators of fuel integrity
- The average fuel temperature
- The maximum strain on the cladding. According to the NRC [28], the uniform strain must be limited to 1%, not including creep and irradiation growth. This limit is in place to preserve cladding integrity. With the simulations discussed in this document, the strain in the cladding cannot be separated into various causes; however, the 1% limit is still a useful reference value.

CHAPTER 3

Modeling and Simulation Background

A Model Domain

The model domain for MPACT can vary greatly in size: from a small axial segment of a fuel pin to a full reactor core [8]. The model domain of a BISON simulation is a single fuel pin, but it is possible to include multiple BISON fuel pins in a single simulation if BISON is coupled with another program. Due to BISON's ability to predict the deformation of the fuel and cladding according to the models outlined in Chapter 2, the BISON mesh deforms over time, causing the domain to change shape.

It should be noted that the BISON domain does not have an expicit mesh for the coolant channel, although BISON can perform a 1D enthalpy rise calculation along the length of the fuel pin. The modeling domain of Redwing is single fuel pins or small rectangular arrays of fuel pins due to limitations in parallelization during simulation.

B Meshing

B.1 MPACT

MPACT discretizes the domain with an sub pin-level mesh, composed of flat (i.e. constant) source regions; flat source regions are commonly employed in MOC calculations [8]. See Fig. 3.1 for an example of an MPACT flat source region mesh. The flat source mesh is further discretized by characteristic rays, which are used to solve for the discretized angular neutron flux. The characteristic ray mesh is currently not exposed to the coupling software; rather, data stored on the flat source mesh are exposed. Each data field stored on the flat source mesh consists of one value per mesh element; hence each data field may be thought of as flat or volume-averaged over a mesh element. Most of the data stored on the flat source mesh comprise the multigroup scalar flux; MPACT stores one flux value per energy group

per flat source mesh element. Some data relevant to multiphysics coupling are derived from the scalar multigroup flux and stored on the flat source mesh; these derived data include fission rate density, power density, and fast neutron flux.

Other data, such as *neutron* cross sections, temperature, and nuclide densities, are stored as flat quantities on the cross section (XS) mesh. The XS mesh is coarser than the flat source mesh. The relationship between the flat source mesh and the XS mesh is simple for cylindrical pin cells; an XS mesh element is the union of all flat source regions in a given radial and axial location (i.e. the XS mesh element is a ring of flat source regions with the azimuthal boundaries removed).

B.2 BISON

MOOSE, and therefore BISON, is based on the Galerkin finite element method [29]. BISON simulations generally employ quadrilateral elements for 2D axisymmetric simulations and hexahedral elements for 3D simulations. For both 2D and 3D meshes, quadratic Lagrange basis functions are employed [26] to represent the solution and auxiliary fields, and constant monomial basis functions are employed to represent other fields. Data fields are stored at the nodes or quadrature points of the finite elements, and each data field has a piecewise continuous representation over the entire finite element mesh. The number of finite elements comprising the BISON mesh of a single fuel rod can vary greatly, depending on the desired mesh refinement, the dimensionality of the simulation, and whether the fuel pellets are modeled as discrete or smeared. A coarse, axisymmetric 2D mesh with smeared pellets could contain $O(10^3)$ finite elements, whereas a fine 3D mesh with discrete pellets could contain $O(10^9)$ or more finite elements. See Fig. 3.1 for an example of a 2D BISON mesh which extends axially and radially.

The dependent variables (i.e. solution fields) stored on the BISON mesh are the displacement and temperature; additional auxiliary variables which BISON obtains from the solution are described in the theory manual [15]. BISON represents the fuel and cladding with separate mesh blocks. The fuel/cladding plenum and coolant region are not meshed in BISON.

BISON has a single channel (i.e. the space surrounding a fuel rod) enthalpy-rise model for calculating the coolant temperature axial profile. The enthalpy-rise model uses a separate, 1D mesh to solve for the coolant temperature based on the inlet temperature, mass flux, and channel cross-sectional area. BISON then maps the coolant temperature to nodes on the outer surface of the cladding mesh and stores it. Section 14 of the BISON theory manual [15] contains details of this model.

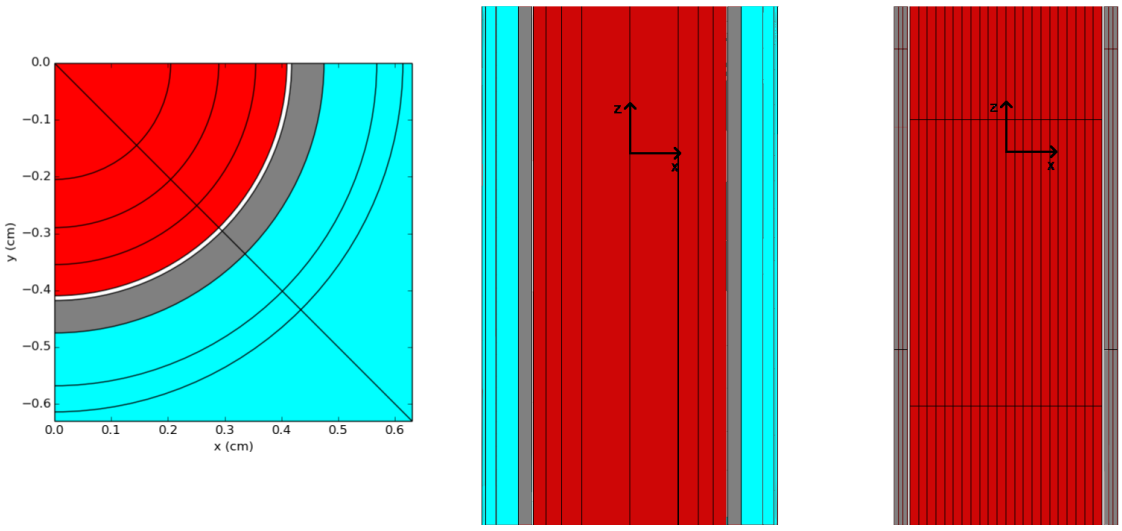

Figure 3.1: Example meshes for a Redwing depletion problem. The MPACT mesh is 3D and the BISON mesh is 2D. There is a cross section of the MPACT mesh (left), a slice down the centerline of the MPACT mesh near the middle of the fuel rod (center), and the BISON mesh near the middle of the fuel rod (right). Red is fuel, gray is cladding, and light blue is coolant. Note that there is no coolant region in the BISON mesh.

C Solution Methods in Individual Programs

C.1 MPACT

The MOC is widely used to solve the neutron transport equation (Eq. (2.1)) because it is a deterministic method that can handle arbitrary geometry (e.g. curved surfaces, like the surface of a fuel rod). The MOC is used to solve the neutron transport equation by reducing it to many ordinary differential equations (ODEs) along characteristic lines, or rays, traced through the domain. The MOC is a type of transport method, specifically a discrete ordinates method [30]; unlike diffusion methods, transport methods treat the angular dependence of the neutron flux solution, yielding the angular flux as a solution. Transport methods provide a more accurate neutron flux solution at material interfaces, which is important to this work because the rim effect occurs near the interface of fuel and the fuel/cladding plenum.

The MOC is used to solve the neutron transport equation for a given nuclide concentration field. The nuclide concentration field is the solution to the nuclide depletion equations, Eq. (2.6), which in turn are dependent on the neutron flux, the solution to the neutron transport equation. In order to couple these equations in the MPACT simulation, the predictor-corrector method is employed. In a nutshell, the method alternatingly solves the nuclide depletion problem and the neutron transport problem, twice each; after a predictor-corrector

step, the neutron flux and nuclide concentration fields are updated. Each time step solved with the predictor-corrector method is referred to as a depletion step. The details of the predictor-corrector method are shown in Fig. 3.2. A sub-step refers to a single solution of

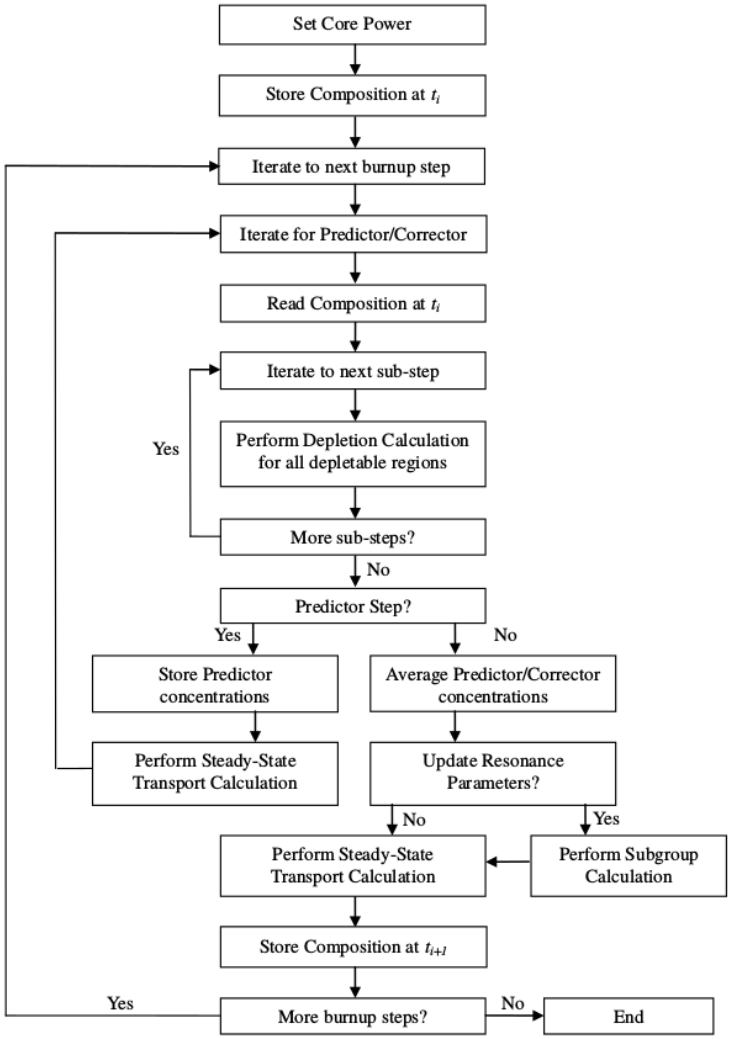

Figure 3.2: MPACT algorithm for solving a depletion step, which advances the neutron transport and nuclide depletion solutions from time t_i to time t_{i+1}.

the nuclide depletion problem, which MPACT may perform multiple times per predictor or corrector step. The predictor-corrector method employs an implicit corrector step, but overall the method is explicit.

C.2 BISON

BISON and all MOOSE applications may employ the Jacobian-Free Newton-Krylov method to obtain a solution. A multivariate, nonlinear problem may be expressed as:

$$\mathbf{L}(\mathbf{T}) = \mathbf{0} \tag{3.1}$$

Eqs. (3.2) and (3.3) describe the Newton method iteration for a multivariate (although not necessarily nonlinear) problem [31]. Given an initial guess $\mathbf{T}^0$, $\mathbf{T}^k$ should converge to the solution of the problem as the iteration index k increases. For each iteration k, Eq. (3.2) is solved for $\Delta\mathbf{T}^k$, and then $\Delta\mathbf{T}^k$ increments $\mathbf{T}^k$.

$$J(\mathbf{T}^k)\Delta\,\mathbf{T}^k = -\mathbf{L}(\mathbf{T}^k) \tag{3.2}$$

$$\mathbf{T}^{k+1} = \mathbf{T}^k + \Delta\mathbf{T}^k \tag{3.3a}$$

where

$\mathbf{T}^k \equiv$ the solution vector at iteration k, i.e. the finite element representation of the solution field

$\Delta\mathbf{T}^k \equiv$ the update to $\mathbf{T}^k$ determined by a Newton iteration

$\mathbf{L}(\mathbf{T}^k) \equiv$ the residual vector, which describes the problem to be solved

$J(\mathbf{T}^k) \equiv$ the Jacobian of $\mathbf{L}(\mathbf{T}^k)$, i.e. $\dfrac{\partial L_j^k}{\partial T_i^k}$; this is a matrix.

Each entry in $\mathbf{L}(\mathbf{T})$ has multiple terms and requires the computation of integrals. Forming the Jacobian is difficult because it requires the differentiation of each entry of $\mathbf{L}(\mathbf{T})$ with respect to each entry of $\mathbf{T}$; inverting the Jacobian to solve Eq. (3.2) would pose additional difficulty. Fortunately, it is not necessary to form the Jacobian explicitly, only to approximate the inverse of $J(\mathbf{T})$ applied to $\mathbf{L}(\mathbf{T})$. By employing the GMRES method to solve Eq. (3.2), it is possible to approximate $J^{-1}(\mathbf{T}^k)\mathbf{L}(\mathbf{T}^k)$ by repeatedly applying $J(\mathbf{T}^k)$ itself to a vector $\mathbf{v}$ throughout the GMRES iterations. To avoid forming $J(\mathbf{T}^k)$, $J(\mathbf{T}^k)\mathbf{v}$ may be replaced by a finite-difference approximation, given by Eq. (3.4). As a result of all this, the solution method is Jacobian-free.

$$J(\mathbf{T}^k)\mathbf{v} \simeq \frac{\mathbf{L}(\mathbf{T}^k + \epsilon\mathbf{v}) - \mathbf{L}(\mathbf{T}^k)}{\epsilon} \tag{3.4}$$

where

$\mathbf{v} \equiv$ is part of a Krylov subspace basis, determined by GMRES (we are skipping details here)

$\epsilon \equiv$ is a small number, usually 10^{-6} for double-precision calculations that may be adjusted in order to optimize the approximation of the Jacobian.

As stated above, GMRES is employed to solve Eq. (3.2). Studies have shown that GMRES should be used as the Krylov method for most applications of JFNK [31]. Considering that GMRES is a linear solver and that it must be run inside each Newton iteration, the GMRES iterations are referred to as linear iterations. The Newton iterations are referred to as nonlinear iterations.

D Data Transfer and Spatial Mapping Methods for Coupling

One issue that complicates the coupling of MPACT and BISON is the changing BISON mesh. With the current setup of Redwing, the MPACT mesh is static throughout the simulation, but the BISON mesh deforms according to the solid mechanics solution; so, all mapping between meshes is done based on the original BISON nodal coordinates. The deformations in the fuel are small relative to the mean free path of a neutron in the fuel, so they also have a small effect on the neutron transport solution.

D.1 MPACT to BISON: Volume-to-Point Mapping

All fields transferred from MPACT to BISON use are mapped via this method; these fields include power density, fission rate density, fast flux, and fuel fission gas concentration. As mentioned in the last section, these data are stored as piecewise constant fields on the MPACT flat source region or cross section (XS) mesh. The method of mapping data from the MPACT mesh to the BISON mesh is as follows: first, a `Function` object in Redwing determines which flat source region a BISON node lies in; then, the appropriate data are transferred from the MPACT flat source region to the BISON node. Note that all BISON quadrature points that reside in a given MPACT flat source region receive the same value for a given quantity (e.g. power density). Fig. 3.3 provides an illustration of this simple data transfer method. All mapping is done using the undeformed BISON node coordinates.

This simple data transfer method introduces error into the transferred data fields. After the unnormalized power density field is transferred to BISON, it is integrated over the undeformed mesh to obtain the BISON unnormalized pin power, $P_{\text{BISON,undef}}$. MPACT also sends the correct value of pin power for each pin, P_{MPACT}. These two pin power values are used to calculate the power normalization factor f_{norm} for each pin; see Eq. (3.5). The power density and fission rate density fields transferred from MPACT are multiplied by f_{norm}, which preserves the power in each pin and keeps the fission rate density consistent with the power density field. The same process is used to calculate separate normalization

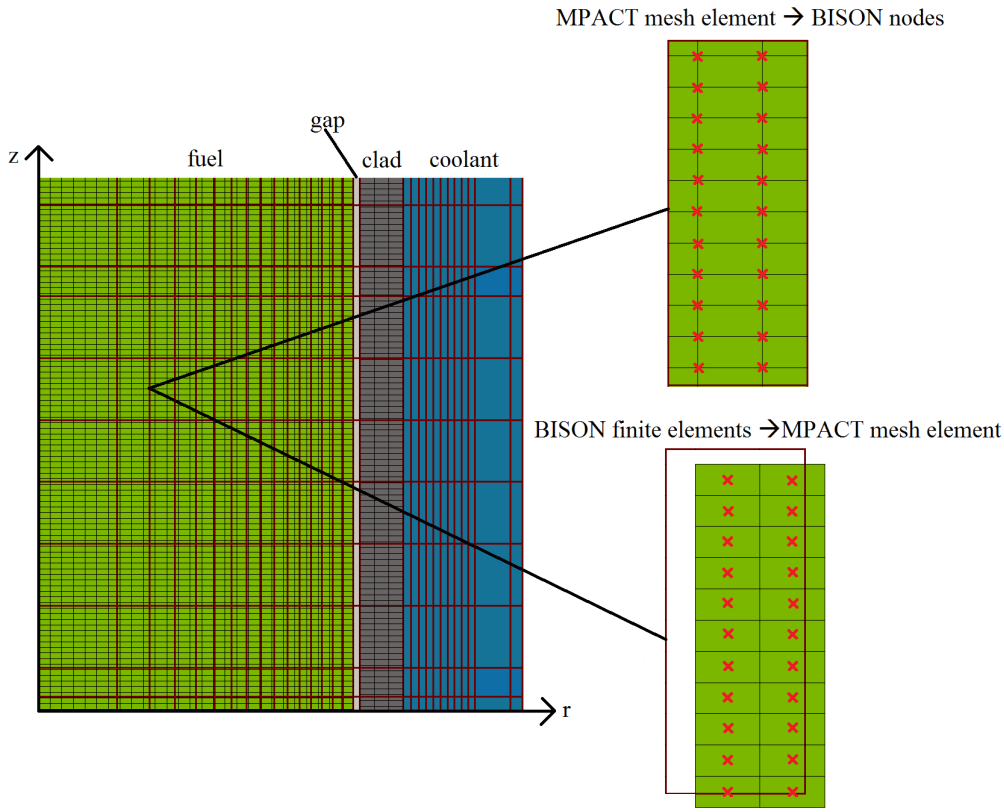

Figure 3.3: This is an illustration of mapping data fields between MPACT and BISON in both directions. It is a 2D-RZ BISON fuel pin mesh slicing through a 3D MPACT pin mesh. On the left, the BISON mesh is the thin black lines and the MPACT mesh is the heavy red lines. At the top right, a BISON node is denoted by a red X, and the large rectangle is an MPACT mesh region. At the bottom right, the MPACT mesh element is an empty rectangle and each BISON centroid is denoted by a red X.

factors for the fast flux and fission gas fields mapped from MPACT to BISON. Note that it is not necessary to use the deformed BISON mesh coordinates for data mapping or calculating integrals because the BISON solver integrates the heat source term of Eq. (2.10) over the undeformed mesh.

$$f_{\text{norm}} = \frac{P_{\text{MPACT}}}{P_{\text{BISON,undef}}} \tag{3.5}$$

D.2 BISON to MPACT: Volume-to-Volume Mapping

Data mapped from the BISON to the MPACT mesh include the temperature in the fuel, cladding, or coolant; the coolant density; and the fuel fission gas concentration. Mapping of the temperature in the fuel and cladding may be done with either the `Postprocessor`-based method or the `LayeredAverage`-based method. Mapping of the fuel fission gas concentration field uses the `Postprocessor`-based method. In both cases, separate averages are performed for the fuel, cladding, and coolant. As with data transfer from MPACT to BISON, data fields transferred in this direction are accompanied by a corresponding integral quantity (e.g. the fuel fission gas concentration field is accompanied by the fuel fission gas inventory). This integral quantity is divided by the integral quantity of the data field on the MPACT mesh (i.e. after mapping and transfer) to obtain a normalization factor, which is then applied to the field on the MPACT mesh. For data transferred in this direction, the quantity is simply Eq. (3.6).

$$\hat{f}_{\text{norm}} = \frac{P_{\text{BISON,undef}}}{P_{\text{MPACT}}} \tag{3.6}$$

D.2.1 LayeredAverage

With the `LayeredAverage`-based data transfer method, Redwing creates a `LayeredAverage` data object which has the same axial divisions as the MPACT XS mesh. Before data transfer from BISON to MPACT, Redwing determines the average temperature in a given layer; this temperature is written to all the MPACT XS mesh elements in that layer for either the fuel or cladding. BISON's finite elements are included in a given temperature average if their centroids lie inside the corresponding layer. More information can be found at the MOOSE Doxygen page for `LayeredAverage` [32]. The `LayeredAverage`-based data transfer method cannot account for the radial dependence of the temperature field. If the coolant temperature and density are mapped from BISON to MPACT, then the a `LayeredAverage` object calculates averages over the outer cladding surface rather than the coolant volume, because BISON stores the coolant data on the mesh nodes on the surface of the cladding

(see Subsection B.2).

D.2.2 Postprocessor

With the `Postprocessor`-based transfer method, Redwing obtains the geometric bounds of each MPACT XS mesh element during the intialization phase of the simulation. Redwing then creates a `Postprocessor` object corresponding to each MPACT cross section mesh element. Each `Postprocessor` object determines all of the BISON mesh elements whose centroids lie in an MPACT mesh element. Before data transfer from BISON to MPACT, each `Postprocessor` object averages the data field over this collection of BISON mesh elements, and then this average value is written to the corresponding MPACT XS mesh element; this data mapping method works for nonalingned MPACT and BISON. Note that this data transfer method requires that each MPACT XS mesh element contains at least one BISON element centroid from the undisplaced mesh. This `Postprocessor`-based data transfer method can transfer temperature fields which have radial and axial discretization. Fig. 3.3 illustrates this data transfer method.

E Overview of Multiphysics Coupling Methods

In this work, the goal is to solve multiple partial differential equations (PDEs) that form a nonlinear system on a single domain (i.e. one or more fuel pins). Certain dependent variables are considered to be the solution variables of specific equations (e.g. the multigroup neutron flux is considered to be a solution of the neutron transport equation); however, in the context of a coupled problem, these variables may also be considered to be part of the solution of the entire coupled system. The coupled neutron transport and fuel performance system is nonlinear because the coefficients of the governing equations depend on the solution variables of other equations. There are several approaches one may take to solve a coupled, nonlinear system.

One approach is full coupling; with this coupling method, PDEs are solved simultaneously as a single system. This allows one to obtain a converged solution to the entire coupled system. JFNK, the method discussed in section C.2, and other Newton method variations can be used to solve coupled problems with full coupling (subject to the tolerance on the residual of the Newton iteration).

Full coupling can be difficult to implement with simulation codes that were originally developed separately. With some coupled systems, it is possible to solve each part of the coupled system (i.e. PDE) separately and still obtain a converged solution to the coupled

problem. This is known as the operator split method. With this method, it is necessary to transfer solution data from one part of the system to the others.

In order to demonstrate the operator split method, an example problem split into two parts will be considered: a coupled neutronics (Eqs. (2.1) and (2.3)) and thermomechanics (Eqs. (2.10) and (2.11)) problem with solution vectors of $\boldsymbol{\phi}$ and $\mathbf{T}$, respectively. For the sake of simplicity, it is assumed that time-dependent nuclide depletion and steady-state neutron transport are combined into neutronics part of the system. Also, the same time step is used to solve each part of the system. In the context of this work, loose coupling means that each part of the system is solved once per time step, with solution data exchanged after each part of the system is solved. Algorithm 1 shows the loose coupling method applied to this simplified example problem. Loose coupling with operator split yields a sufficiently converged solution to the entire coupled system if the time step is sufficiently small.

Algorithm 1 Loose coupling solution method for an example problem

Input: $\boldsymbol{\phi}^{(0)}, \mathbf{T}^{(0)}$

for time step $i = 1, N$ **do**
    Solve the neutronics equations for $\boldsymbol{\phi}^{(i)}$,
    Calculate the coefficients of the thermomechanics equations using $\boldsymbol{\phi}^{(i)}$
    Solve the thermomechanics equations for $\mathbf{T}^{(i)}$
    Calculate the coefficients of the neutronics equations using $\mathbf{T}^{(i)}$

Output: $\boldsymbol{\phi}^{(N)}, \mathbf{T}^{(N)}$

Tight coupling is similar to loose coupling, except that there is an iteration over each time step, called a Picard iteration. The Picard iteration proceeds until residuals for each part of the coupled problem fall below a certain tolerance; or, in the case of the neutron transport problem, the change in the neutronic eigenvalue between iterates falls below a specified tolerance. Tight coupling may be more expensive than loose coupling, but it is better at resolving errors introduced by the operator split method.

F Description of Coupled Depletion Algorithm in Redwing

As mentioned previously, Redwing executes depletion runs with two-way data transfer. Redwing calculates the solution to the coupled fuel depletion problem with a loose operator split method. This coupling method is expected to be $O(\Delta t)$, where Δt is MPACT's depletion time step size. With loose coupling, each Redwing time step proceeds as follows: MPACT takes a depletion step and calculates a few fields derived from the neutron flux solution, including power density, at the end of that time step; Redwing transfers these

data to BISON; and then BISON uses these fields and solves the thermomechanics part of the problem for the same time step. It is possible to run the MPACT depletion step and the BISON time step at the same time, but this would mean that BISON would have to use the MPACT data from the beginning of the depletion step. Because BISON usually takes implicit time steps, using transferred fields from the end of the MPACT depletion step is more consistent with this formulation.

Other than the power density field, MPACT also transfers the fission rate density and fast neutron flux fields to BISON. The fission rate density field is used by BISON to calculate burnup, fuel creep, and fission gas release. The fast flux field is used by BISON to calculate the creep rate in the cladding. As mentioned earlier, there is two-way data transfer; at the end of a time step, BISON transfers the temperature field to MPACT. MPACT uses these data to update the macroscopic neutron cross sections, which appear as coefficients in the neutron transport equation. Also, MPACT performs resonance shielding calculations throughout Redwing simulations at an interval of about 200 days; this is done to take into account the effect of absorption resonances on the multigroup cross sections, so that self-shielding in fuel pins is modeled accurately.

Redwing originally used a coupled thermal hydraulics (i.e. TH) method in which the coolant temperature and density were computed by BISON's 1D enthalpy rise model, and then sent to MPACT at the end of a depletion time step. Models with coupled TH have stability issues due to the strong mutual influence between the fuel power density and coolant density fields; coupled TH also results in lagged coolant updates for the depletion solver. Although this mutual influence is physically realistic and can be observed in reactor operation (especially boiling water reactors), it also causes unphysical fluctuations in the axial power density profile in simulations with loose coupling between TH and neutron transport. In coupled TH mode, Redwing first solves for the conditions at hot zero power, then performs a startup ramp to hot full power with tight coupling. During the startup ramp, the composition of the fuel is fixed. Then, Redwing makes MPACT take a depletion step that matches the burnup of the startup ramp. After this point in the simulation, Redwing runs with loose couping, whether the model has coupled or prescribed TH.

Nearly all Redwing simulations in this dissertation were performed with its prescribed TH capability; in prescibed TH mode, Redwing looks up cladding outer wall temperatures to use as boundary conditions for the BISON thermomechanics problem, and looks up coolant temperature and density for the MPACT neutron transport problem. Using a prescribed coolant density improves the stability the simulations.

Due to a variety of physical models included in the BISON simulation, BISON may need to take smaller time steps than MPACT (especially during large power level changes).

Hence, BISON is allowed to take multiple time steps per MPACT depletion step. If a BISON time step fails, Redwing will half the time step size and make BISON retake the time step; after that, Redwing will make BISON attempt to take a time step to catch up to MPACT.

G Overview of Fission Gas Integral Quantities

Simple set theory is used to describe various integral fission gas results. With the implementation of fission gas coupling, distinctions arise between formerly identical quantities, such as the fission gas released and the plenum fission gas inventory. The sets of fission gas atoms described below correspond to specific integral quantites that appear in the coupling algorithms and in plots in following chapters.

1. $H \equiv$ Fission gas atoms generated up to time t
2. $G \equiv$ Net fission gas atoms generated (i.e. fission gas atoms generated, not including atoms lost due to transmutation in fuel) up to time t
3. $I_{\text{fuel}} \equiv$ Fission gas atoms contained in the fuel (i.e. fission gas inventory) at time t
4. $R \equiv$ Fission gas atoms released up to time t
5. $I_{\text{plenum}} \equiv$ Fission gas atoms contained in the fuel/cladding plenum at time t

The following relationships should be enforced:

1. $G \subseteq H$
2. $I_{\text{fuel}} \subseteq G$
3. $G = I_{\text{fuel}} \cup R$
4. $I_{\text{plenum}} \subseteq R$

The integral corresponding to set G, the net fission gas generated in the fuel, is usually reported. It is difficult to obtain the integral corresponding to H, the total fission gas generated, because the Bateman solver in MPACT does not integrate the production rate of any nuclide over time; rather, the solver integrates the gain and loss rates of each nuclide to yield the number density at a given time.

H Successive Fission Gas Coupling Algorithms

The fission product tracking capability of MPACT holds potential benefits for the multi-physics simulation of fission gas release. With BISON, there are several drawbacks with the Sifgrs model; as mentioned in Section B.1, the fission gas is treated in a lumped fashion and transmutation and decay of fission gas is neglected, which is not the case in MPACT. Another advantage to using MPACT is it is able to capture the change in the fission gas yield as a function of burnup. This change occurs because ^{239}Pu slowly replaces ^{235}U over the lifetime of LWR fuel. Fig. 2.2 shows the difference in fission yields between ^{235}U and ^{239}Pu. Due to the advantages of MPACT's fission gas tracking, each algorithm presented here replaces BISON's fission gas source with a new source based on MPACT's prediction of fission gas concentration, which improves the overall fission gas concentration prediction.

In this chapter, fission gas coupling algorithms are presented in order of increasing complexity. These algorithms hide the complexity of the MPACT and BISON solvers, instead focusing on the details of fission gas data exchange and handling. These are designed with the separate programs, MPACT and BISON, in mind. The first algorithm, Algorithm 2, was written to advance the solution of the coupled problem over a time step $\Delta t^{(i+1)}$ from time i to $i+1$. Values indexed as $i+1/2$ indicate intermediate values calculated during the time step between time i and $i+1$. This algorithm assumes a spatially continuous solution and has treatment for the collapse and extension of the fission gas vector, with BISON's Sifgrs solver in mind. Algorithm 3 adds one level of complexity; here, the special treatment for the undeformed fuel/cladding plenum is considered, so there are extra steps to distribute the fission gas released to the plenum. Algorithm 4 is written with solution vectors, which represent discrete data on the MPACT and BISON meshes; this algorithm is the best representation of the source code in MPACT, BISON, and Redwing.

Algorithm 2 Fission gas (FG) coupling algorithm: continuous in space (no meshes)

Input: $\phi^{(i)}(\mathbf{r},E), \mathbf{N}^{(i)}(\mathbf{r}), \mathbf{T}^{(i)}(\mathbf{r}), I^{(i)}_{\text{plenum}}, ...$

Solve the coupled neutron transport and nuclide transmutation equations:
$\phi^{(i+1/2)}(\mathbf{r},E), \mathbf{N}^{(i+1/2)}(\mathbf{r}) = \text{PC}(\phi^{(i)}(\mathbf{r},E), \mathbf{N}^{(i)}(\mathbf{r}), \Delta t^{(i+1)})$

Compute intra-pin quantites for the coefficients of the thermomechanics problem:
$\dot{F}(\mathbf{r}) = \int_0^\infty dE \Sigma_f(\mathbf{r},E)\phi^{(i+1/2)}(\mathbf{r},E)$
$q'''(\mathbf{r}) = \int_0^\infty dE \kappa\Sigma_f(\mathbf{r},E)\phi^{(i+1/2)}(\mathbf{r},E)$
$\phi_{\text{fast}}(\mathbf{r}) = \int_{1\text{MeV}}^\infty dE \phi^{(i+1/2)}(\mathbf{r},E)$

Sum up FG nuclide number densities:
$N^{(i+1/2)}(\mathbf{r}) = \sum_{n=1}^{19} N_n^{(i+1/2)}(\mathbf{r})$ for $\mathbf{r} \in$ fuel

Compute incremental change in FG number density due to production and transmutation in fuel:
$\Delta N^{(i+1)}_{\text{gen,tran}}(\mathbf{r}) = N^{(i+1/2)}(\mathbf{r}) - N^{(i)}(\mathbf{r})$ for $\mathbf{r} \in$ fuel

Compute incremental change in FG number density due to transmutation in plenum:
$\Delta N^{(i+1)}_{\text{tran}}(\mathbf{r}) = N^{(i+1/2)}(\mathbf{r}) - N^{(i)}(\mathbf{r})$ for $\mathbf{r} \in$ plenum

Compute FG production rate:
$\beta^{(i+1)}(\mathbf{r}) = \Delta N^{(i+1)}_{\text{gen,tran}} / \Delta t^{(i+1)}$ for $\mathbf{r} \in$ fuel

Simultaneously solve thermomechanics problem, including FG release

$\mathbf{T}^{(i+1)}(\mathbf{r}), V^{(i+1)}_{\text{gap}}, V^{(i+1)}_{\text{UL}} =$
$\text{B}(\mathbf{T}^{(i+1)}(\mathbf{r}), \dot{F}(\mathbf{r}), q'''(\mathbf{r}), \phi_{\text{fast}}(\mathbf{r}), N^{(i+1)}(\mathbf{r}), I^{(i+1)}_{\text{plenum}}, \Delta t^{(i+1)})$

Compute fuel FG number density field with Sifgrs:
$N^{(i+1)}(\mathbf{r}) = \text{Sifgrs}(\mathbf{T}^{(i+1)}(\mathbf{r}), \dot{F}(\mathbf{r}), \beta^{(i+1)}(\mathbf{r}), \Delta t^{(i+1)})$ for $\mathbf{r} \in$ fuel

Compute incremental FG release with Sifgrs:
$\Delta R = \int_{fuel} d\mathbf{r}(N^{(i)}(\mathbf{r}) + \beta^{(i+1)}(\mathbf{r})\Delta t^{(i+1)} - N^{(i+1)}(\mathbf{r}))$

Compute plenum FG inventory without transmutation:
$I^{(i+1/2)}_{\text{plenum}} = I^{(i)}_{\text{plenum}} + \Delta R$

Compute incremental change in FG number density due to release in plenum:
$\Delta N^{(i+1)}_{rel}(\mathbf{r}) = I^{(i+1/2)}_{\text{plenum}} / V^{(i+1)}_{\text{plenum}} - N^{(i)}(\mathbf{r})$ for $\mathbf{r} \in$ plenum

Sum incremental changes in FG number density to get FG number density field in plenum:
$N^{(i+1)}(\mathbf{r}) = N^{(i)}(\mathbf{r}) + \Delta N^{(i+1)}_{\text{tran}}(\mathbf{r}) + \Delta N^{(i+1)}_{\text{rel}}(\mathbf{r})$ for $\mathbf{r} \in$ plenum

Integrate FG number density field in plenum to get plenum FG inventory:
$I^{(i+1)}_{\text{plenum}} = \int_{\text{plenum}} d\mathbf{r} N^{(i+1)}(\mathbf{r})$

for $n = 1, 19$ **do**

$f_n = \int_{fuel} d\mathbf{r} N_n^{(i+1/2)}(\mathbf{r}) / \int_{fuel} d\mathbf{r} N^{(i+1/2)}(\mathbf{r})$

Extend FG number density to nuclides in plenum based on fuel nuclide fractions:
$N_n^{(i+1)}(\mathbf{r}) = N_n^{(i+1/2)}(\mathbf{r}) + \Delta N^{(i+1)}_{\text{rel}}(\mathbf{r}) f_n$ for $\mathbf{r} \in$ plenum

for $n = 1, 19$ **do**

Extend FG number density to nuclides in fuel based on local nuclide fractions:
$N_n^{(i+1)}(\mathbf{r}) = N^{(i+1)}(\mathbf{r}) N_n^{(i+1/2)}(\mathbf{r}) / N^{(i+1/2)}(\mathbf{r})$ for $\mathbf{r} \in$ fuel

Solve neutron transport problem again to account for feedback:
$\phi^{(i+1)}(\mathbf{r},E) = \text{Eigen}(\phi^{(i+1/2)}(\mathbf{r},E), \mathbf{N}^{(i+1)}(\mathbf{r}))$

Output: $\phi^{(i+1)}(\mathbf{r},E), \mathbf{N}^{(i+1)}(\mathbf{r}), \mathbf{T}^{(i+1)}(\mathbf{r}), I^{(i+1)}_{\text{plenum}}, ...$

where:

- $\mathbf{r}$ is the position vector
- E is the neutron energy
- ϕ is the scalar flux.
- $\mathbf{N}^{(i)}$ is the fission gas atom number density field, indexed by nuclide n, at time step i.
- PC is the MPACT depletion operator (P.C. stands for predictor-corrector)
- $\dot{F}$ is the fission rate density.
- q''' is the power density.
- κ is the energy released per fission.
- Σ_f is the macroscopic fission cross section.
- ϕ_{fast} is the fast neutron flux.
- N is the fission gas number density field summed over all nuclides.
- $\Delta N_{\text{gen,tran}}$ is the change in fission gas number density due to generation and transmutation.
- ΔN_{tran} is the change in fission gas number density due to transmutation.
- β is the Sifgrs fission gas source.
- $\mathbf{T}$ is the thermomechanics solution, which includes temperature and displacement.
- V_{gap} is the volume of the fuel/cladding gap.
- V_{UL} is the volume of the fuel/cladding upper and lower plena.
- B is the BISON solver operator, which updates $\hat{\mathbf{T}}$ using JFNK.
- Sifgrs is the Sifgrs operator, which updates the fission gas field; it is separated from B for clarity.
- ΔR is the fission gas release contribution to the fuel/cladding plenum.
- ΔN_{rel} is the change in fission gas number density due to release.

- I_{plenum} is the fission gas inventory in the plenum (i.e. gap + upper and lower plena).
- Eigen is the operator which yields the solution to the neutron transport eigenvalue problem.

Algorithm 3 replaces step 12 from Algorithm 2 with steps 12-15. These steps constitute the undeformed plenum treatment. Although this algorithm does not explicitly refer to two separate meshes, the extra steps would not be necessary unless some quantities corresponded to an undeformed fuel pin geometry and some corresponded to a deformed fuel pin geometry. The undeformed plenum treatment specifically means that the quantity $N^{(i+1)}(\mathbf{r})$ is calculated for the undeformed plenum, but the integral of $N^{(i+1)}(\mathbf{r})$ over the undeformed gap will yield the same amount of fission gas that is contained in the deformed gap; similarly, the integral of $N^{(i+1)}(\mathbf{r})$ over the undeformed upper and lower plena will yield the same amount of fission gas that is contained in those parts of the deformed plenum. This special treatment was motivated by the desire to reduce errors in the MPACT neutron transport solution without enabling mesh deformation in MPACT; the treatment essentially redistributes fission gas from the undeformed MPACT gap region according to how much gap closure has occured.

Algorithm 3 Fission gas coupling algorithm: continuous in space (no meshes), undeformed plenum treatment

Input: $\phi^{(i)}(\mathbf{r},E), \mathbf{N}^{(i)}(\mathbf{r}), \mathbf{T}^{(i)}(\mathbf{r}), I^{(i)}_{\text{plenum}}, ...$

1: Solve the coupled neutron transport and nuclide transmutation equations:
$\phi^{(i+1/2)}(\mathbf{r},E), \mathbf{N}^{(i+1/2)}(\mathbf{r}) = \text{PC}(\phi^{(i)}(\mathbf{r},E), \mathbf{N}^{(i)}(\mathbf{r}), \Delta t^{(i+1)})$

2: Compute intra-pin quantites for the coefficients of the thermomechanics problem:
$\dot{F}(\mathbf{r}) = \int_0^\infty dE \Sigma_f(\mathbf{r},E)\phi^{(i+1/2)}(\mathbf{r},E)$
$q'''(\mathbf{r}) = \int_0^\infty dE \kappa\Sigma_f(\mathbf{r},E)\phi^{(i+1/2)}(\mathbf{r},E)$
$\phi_{\text{fast}}(\mathbf{r}) = \int_{1\text{MeV}}^\infty dE \phi^{(i+1/2)}(\mathbf{r},E)$

3: Sum up FG nuclide number densities:
$N^{(i+1/2)}(\mathbf{r}) = \sum_{n=1}^{19} N_n^{(i+1/2)}(\mathbf{r})$ for $\mathbf{r} \in$ fuel

4: Compute incremental change in FG number density due to production and transmutation in fuel:
$\Delta N^{(i+1)}_{\text{gen,tran}}(\mathbf{r}) = N^{(i+1/2)}(\mathbf{r}) - N^{(i)}(\mathbf{r})$ for $\mathbf{r} \in$ fuel

5: Compute incremental change in FG number density due to transmutation in plenum:
$\Delta N^{(i+1)}_{\text{tran}}(\mathbf{r}) = N^{(i+1/2)}(\mathbf{r}) - N^{(i)}(\mathbf{r})$ for $\mathbf{r} \in$ plenum

6: Compute FG production rate:
$\beta^{(i+1)}(\mathbf{r}) = \Delta N^{(i+1)}_{\text{gen,tran}} / \Delta t^{(i+1)}$ for $\mathbf{r} \in$ fuel

7: **Simultaneously solve** thermomechanics problem, including FG release:

8: $\mathbf{T}^{(i+1)}(\mathbf{r}), V^{(i+1)}_{\text{gap}}, V^{(i+1)}_{\text{UL}} =$
$\text{B}(\mathbf{T}^{(i+1)}(\mathbf{r}), \dot{F}(\mathbf{r}), q'''(\mathbf{r}), \phi_{\text{fast}}(\mathbf{r}), N^{(i+1)}(\mathbf{r}), I^{(i+1)}_{\text{plenum}}, \Delta t^{(i+1)})$

9: Compute fuel FG number density field with Sifgrs:
$N^{(i+1)}(\mathbf{r}) = \text{Sifgrs}(\mathbf{T}^{(i+1)}(\mathbf{r}), \dot{F}(\mathbf{r}), \beta^{(i+1)}(\mathbf{r}), \Delta t^{(i+1)})$ for $\mathbf{r} \in$ fuel

10: Compute incremental FG release with Sifgrs:
$\Delta R = \int_{\text{fuel}} d\mathbf{r}(N^{(i)}(\mathbf{r}) + \beta^{(i+1)}(\mathbf{r})\Delta t^{(i+1)} - N^{(i+1)}(\mathbf{r}))$

11: Compute plenum FG inventory without transmutation:
$I^{(i+1/2)}_{\text{plenum}} = I^{(i)}_{\text{plenum}} + \Delta R$

12: Compute gap FG inventory with deformed mesh volumes:
$I^{(i+1)}_{\text{gap}} = I^{(i+1/2)}_{\text{plenum}} V^{(i+1)}_{\text{gap}} / (V^{(i+1)}_{\text{gap}} + V^{(i+1)}_{\text{UL}})$

13: Compute upper and lower plena FG inventory with deformed mesh volumes:
$I^{(i+1)}_{\text{UL}} = I^{(i+1/2)}_{\text{plenum}} V^{(i+1)}_{\text{UL}} / (V^{(i+1)}_{\text{gap}} + V^{(i+1)}_{\text{UL}})$

14: Compute incremental change in FG number density due to release in gap:
$\Delta N^{(i+1)}_{\text{rel}}(\mathbf{r}) = I^{(i+1)}_{\text{gap}} / V^{(0)}_{\text{gap}} - N^{(i)}(\mathbf{r})$ for $\mathbf{r} \in$ gap

15: Compute incremental change in FG number density due to release in upper and lower plena:
$\Delta N^{(i+1)}_{\text{rel}}(\mathbf{r}) = I^{(i+1)}_{\text{UL}} / V^{(0)}_{\text{UL}} - N^{(i)}(\mathbf{r})$ for $\mathbf{r} \in$ upper and lower plena

16: Sum incremental changes in FG number density to get FG number density field in plenum:
$N^{(i+1)}(\mathbf{r}) = N^{(i)}(\mathbf{r}) + \Delta N^{(i+1)}_{\text{tran}}(\mathbf{r}) + \Delta N^{(i+1)}_{\text{rel}}(\mathbf{r})$ for $\mathbf{r} \in$ plenum

17: Integrate FG number density field in plenum to get plenum FG inventory:
$I^{(i+1)}_{\text{plenum}} = \int_{\text{plenum}} d\mathbf{r} N^{(i+1)}(\mathbf{r})$

Algorithm 3 Fission gas coupling algorithm, continuous in space (no meshes), undeformed plenum treatment (continued)

for $n = 1, 19$ **do**

  $f_n = \int_{\text{fuel}} d\mathbf{r} N_n^{(i+1/2)}(\mathbf{r}) / \int_{\text{fuel}} d\mathbf{r} N^{(i+1/2)}(\mathbf{r})$

  Extend FG number density to nuclides in plenum based on fuel nuclide fractions:

    $N_n^{(i+1)}(\mathbf{r}) = N_n^{(i+1/2)}(\mathbf{r}) + \Delta N_{\text{rel}}^{(i+1)}(\mathbf{r}) f_n$ for $\mathbf{r} \in$ plenum

for $n = 1, 19$ **do**

  Extend FG number density to nuclides in fuel based on local nuclide fractions:

    $N_n^{(i+1)}(\mathbf{r}) = N^{(i+1)}(\mathbf{r}) N_n^{(i+1/2)}(\mathbf{r}) / N^{(i+1/2)}(\mathbf{r})$ for $\mathbf{r} \in$ fuel

Solve neutron transport problem again to account for feedback:

  $\phi^{(i+1)}(\mathbf{r}, E) = \text{Eigen}(\phi^{(i+1/2)}(\mathbf{r}, E), \mathbf{N}^{(i+1)}(\mathbf{r}))$

Output: $\phi^{(i+1)}(\mathbf{r}, E), \mathbf{N}^{(i+1)}(\mathbf{r}), \mathbf{T}^{(i+1)}(\mathbf{r}), I_{\text{plenum}}^{(i+1)}, \ldots$

where:

- I_{gap} is the gap fission gas inventory.
- I_{UL} is the upper and lower plena fission gas inventory.

Algorithm 4 describes fission gas coupling in Redwing for a single time step of size $\Delta t^{(i+1)}$, stepping from time i to time $i+1$. This time step occurs after the startup ramp; fission gas data are not exchanged during the startup ramp because it is run with the initial nuclide densities. Note that loose coupling is employed here (i.e. there is no Picard iteration). On the BISON fuel mesh, the fission gas density at each point actually consists of 3 separate values, one for each state of the fission gas at a given spatial location (i.e. intragranular, in grain face bubbles, or in high bunrup structures). Fission gas does not appear in high burnup structures until the local burnup reaches 70 MWD/kgHM. This is not reflected in the algorithms: before data are transferred between the MPACT and BISON fuel meshes, the fission gas number densities at a point are summed so there is only one value at that point. In the Algorithm 4, quantities with hats are stored on the BISON mesh; quantities without hats are stored on the MPACT mesh.

Algorithm 4 Fission gas coupling discretized algorithm: undeformed plenum treatment

Input: $\boldsymbol{\phi}^{(i)}, \mathbf{M}^{(i)}, \mathbf{N}^{(i)}, \hat{\mathbf{T}}^{(i)}, I^{(i)}_{\text{plenum}}, \ldots$

$\boldsymbol{\phi}^{(i+1/2)}, \mathbf{M}^{(i+1/2)} = \text{PC}(\boldsymbol{\phi}^{(i)}, \mathbf{M}^{(i)}, \Delta t^{(i+1)})$

for $k = 1, K$ **do**

  $\dot{F}_k = \sum_{e=1}^{E} \Sigma_{\text{f},k,e} \phi^{(i+1/2)}_{k,e}$

  $q'''_k = \sum_{e=1}^{E} \kappa \Sigma_{\text{f},k,e} \phi^{(i+1/2)}_{k,e}$

  $\phi_{\text{fast},k} = \sum_{\forall e > 1\text{MeV}} \phi^{(i+1/2)}_{k,e}$

for $k \in$ fuel and plenum **do**

  $N^{(i+1/2)}_k = \sum_{n=1}^{19} M^{(i+1/2)}_{n,k}$

for $k \in$ fuel **do**

  $\Delta N^{(i+1)}_{\text{gen,tran},k} = N^{(i+1/2)}_k - N^{(i)}_k$

  $G^{(i+1)}_k = \Delta N^{(i+1)}_{\text{gen,tran},k} + G^{(i)}_k$

for $k \in$ plenum **do**

  $\Delta N^{(i+1)}_{\text{tran},k} = N^{(i+1/2)}_k - N^{(i)}_k$

Integrate $\mathbf{G}^{(i+1)}$ over MPACT fuel mesh to obtain G

Map and transfer $\mathbf{G}^{(i+1)} \rightarrow \hat{\mathbf{G}}^{(i+1)}$ on BISON fuel mesh

Normalize $\hat{\mathbf{G}}^{(i+1)}$ so that G is preserved

Map and transfer $\dot{\mathbf{F}}$ and $\mathbf{q}'''$ to BISON fuel mesh and preserve integral over fuel

Map and transfer $\boldsymbol{\phi}_{\text{fast}}$ to BISON cladding mesh and preserve integral over cladding

for $l \in$ fuel **do**

  $\hat{\beta}_l = (\hat{G}^{(i+1)}_l - \hat{G}^{(i)}_l)/\Delta t^{(i+1)}$

Simultaneously solve thermo-mechanics problem, including FG release:

  $\hat{\mathbf{T}}^{(i+1)}, V^{(i+1)}_{\text{gap}}, V^{(i+1)}_{\text{UL}} = \text{B}(\hat{\mathbf{T}}^{(i+1)}, \hat{\dot{\mathbf{F}}}, \hat{\mathbf{q}}''', \hat{\boldsymbol{\phi}}_{\text{fast}}, \hat{\mathbf{N}}^{(i+1)}, I^{(i+1)}_{\text{plenum}}, \Delta t^{(i+1)})$

  $\hat{\mathbf{N}}^{(i+1)} = \text{Sifgrs}(\hat{\mathbf{N}}^{(i)}, \hat{\mathbf{T}}^{(i+1)}, \hat{\dot{\mathbf{F}}}, \hat{\boldsymbol{\beta}}, \Delta t^{(i+1)})$ on BISON fuel mesh

  $\Delta R \leftarrow$ integral of $(\hat{N}^{(i)} + \hat{\boldsymbol{\beta}} \Delta t^{(i+1)} - \hat{\mathbf{N}}^{(i+1)})$ over BISON fuel mesh

  $I^{(i+1/2)}_{\text{plenum}} = I^{(i)}_{\text{plenum}} + \Delta R$

  $I^{(i+1)}_{\text{gap}} = I^{(i+1/2)}_{\text{plenum}} V^{(i+1)}_{\text{gap}} / (V^{(i+1)}_{\text{gap}} + V^{(i+1)}_{\text{UL}})$

  $I^{(i+1)}_{\text{UL}} = I^{(i+1/2)}_{\text{plenum}} V^{(i+1)}_{\text{UL}} / (V^{(i+1)}_{\text{gap}} + V^{(i+1)}_{\text{UL}})$

  $\Delta \mathbf{N}^{(i+1)}_{\text{rel}} = I^{(i+1)}_{\text{gap}} / V^{(0)}_{\text{gap}} - \mathbf{N}^{(i)}$ for $k \in$ gap

  $\Delta \mathbf{N}^{(i+1)}_{\text{rel}} = I^{(i+1)}_{\text{UL}} / V^{(0)}_{\text{UL}} - \mathbf{N}^{(i)}$ for $k \in$ upper and lower plena

  $I^{(i+1)}_{\text{plenum}} = \sum_{k \in \text{plenum}} N^{(i+1)}_k \Delta V_k$

for $k \in$ plenum **do**

  if $k \in$ gap and $I^{(i+1)}_{\text{gap}} = 0$ **then**

    $N^{(i+1)}_k = 0.0$

  else

    $N^{(i+1)}_k = N^{(i)}_k + \Delta N^{(i+1)}_{\text{tran},k} + \Delta N^{(i+1)}_{\text{rel},k}$ for $k \in$ plenum

Algorithm 4 Fission gas coupling improved, discretized algorithm: undeformed plenum treatment (continued)

for $n = 1, 19$ **do**
    $f_n = \sum_{k \in \text{fuel}} M_{k,n}^{(i+1/2)} \Delta V_k / \sum_{k \in \text{fuel}} N_k^{(i+1/2)} \Delta V_k$
    for $k \in$ plenum **do**
        $M_{n,k}^{(i+1)} = M_{n,k}^{(i+1/2)} + \Delta N_{\text{rel},k}^{(i+1)} f_n$
Integrate $\hat{\mathbf{N}}^{(i+1)}$ over undeformed BISON fuel mesh to obtain $\hat{I}_{\text{fuel}}$
Map and transfer $\hat{\mathbf{N}}^{(i+1)} \rightarrow \mathbf{N}^{(i+1)}$ on MPACT fuel mesh
Normalize $\mathbf{N}^{(i+1)}$ so that $\hat{I}_{\text{fuel}}$ is preserved
for $n = 1, 19$ **do**
    for $k \in$ fuel **do**
        $M_{n,k}^{(i+1)} = N_k^{(i+1)} M_{n,k}^{(i+1/2)} / N_k^{(i+1/2)}$
Integrate temperature in $\hat{\mathbf{T}}^{(i+1)}$ over undeformed BISON fuel mesh to obtain $\hat{U}$
Map and transfer $\hat{\mathbf{T}}^{(i+1)} \rightarrow \mathbf{T}^{(i+1)}$ on MPACT fuel and cladding mesh
Normalize $\mathbf{T}^{(i+1)}$ so integrated temperature $\hat{U}$ is preserved
$\boldsymbol{\phi}^{(i+1)} = \text{Eigen}(\boldsymbol{\phi}^{(i+1/2)}, \mathbf{N}^{(i+1)}, \mathbf{T}^{(i+1)})$

Output: $\boldsymbol{\phi}^{(i+1)}, \mathbf{M}^{(i+1)}, \mathbf{N}^{(i+1)}, \hat{\mathbf{T}}^{(i+1)}, I_{\text{plenum}}^{(i+1)}, \ldots$

where:

- $\boldsymbol{\phi}$ is the scalar flux, which indexed by mesh element k and energy group e.
- $\mathbf{M}$ is the extended fission gas nuclide field, indexed by nuclide n and mesh element k.
- $\mathbf{N}$ is the fission gas nuclide field, indexed by mesh element k.
- $\mathbf{G}$ is the time-integral of fission gas generation and transmutation in fuel, indexed by mesh element k. Sifgrs needs this quantity to accurately compute the fission gas source.
- G is the integral of $\mathbf{G}$ over the fuel pin.
- $\hat{\mathbf{T}}$ is the BISON solution, indexed mesh element l, which includes temperature and displacement.
- $\dot{\mathbf{F}}$ is the fission rate density, indexed by mesh element k.
- $\mathbf{q}'''$ is the power density, indexed by mesh element k.
- $\boldsymbol{\phi}_{\text{fast}}$ is the scalar fast neutron flux, indexed by mesh element k.
- I_{fuel} is the fuel fission gas inventory.

Algorithm 4 is designed for a problem discretized on two separate meshes. The differences in the MPACT and BISON meshes were covered in Section B. All quantities mapped between meshes should be normalized to reduce mapping error. In order to do this, a normalization factor is computed according to equations (3.5) and (3.6). When these normalization factors are applied to the proper mapped data, the full-pin integral of the data is preserved.

Two separate fission gas inventories are written to the gap and upper/lower plena regions in MPACT; this is special treatment which attempts to account for gap closure, which is not modeled with the MPACT mesh. For example, when the gap has completely closed in the BISON mesh, no fission gas will be written to the gap region in MPACT, even though this region has a nonzero volume on the MPACT mesh. This special treatment was included in the algorithm because the location of fission gas can have a significant effect on the neutron transport problem.

Step 32 of Algorithm 4 is a special treatment to avoid writing negative values to $\mathbf{N}^{(i+1)}$. Due to time discretization error, the calculation in Step 34 might yield negative values for

$\mathbf{N}^{(i+1)}$ in a given gap mesh element if $I_{\text{gap}}^{(i+1)}$ is zero or very small. This leads to writing non-physical values to $\mathbf{N}^{(i+1)}$ in the gap, which alternate between positive and negative with each time step (i.e. as a result of having nonzero values stored in $\mathbf{N}^{(i)}$). Although this issue would be solved in the limit of $\Delta t^{(i+1)}$ approaching zero, this special treatment is implemented for simulations with reasonably-sized time steps.

I Design of Redwing for Simulating Fuel Pin Arrays

Before describing the design of Redwing, it is necessary to describe MOOSE's `MultiApps` system [33]. When simulating multiple fuel pins, Redwing takes advantage of this MOOSE system. With a `MultiApps` run, there is usually a master app and multiple sub apps. Each sub app has its own mesh and `Executioner`; it is a nearly independent instantiation of a MOOSE application, except that the master app is able to control each sub app's time stepping. With `MultiApps` runs, data may be exchanged between the master and sub apps using MOOSE's `Transfer` class. The data transferred range from nothing, to a single scalar value, to the entire solution field of the master or sub app. So, with `MultiApps`, MOOSE can solve systems of PDEs which are loosely coupled via `Transfer` objects.

When Redwing performs simulations of multiple pins, it spawns a Redwing sub app, each of which contains a single BISON fuel pin mesh. There is one Redwing master app (another MOOSE object) which runs the Redwing executioner and controls the Redwing sub apps. The physical coupling between fuel pins in an actual nuclear reactor is mainly the result of neutron streaming, and to a lesser extent due to coolant cross flow between individual pin cells. In Redwing, the solutions stored on the separate BISON meshes are coupled via data transfer with the MPACT, in which all the pins in the model are contained within a single mesh. More specifically, the BISON mesh solutions are coupled via the neutron transport solution provided by MPACT. Accordingly, most data transfer should occur between the parts of the program holding the BISON mesh data and the parts holding the MPACT mesh data. Therefore, rather than exchanging field data with the master app, each sub app exchanges data directly with MPACT (i.e. the part of the Redwing instantiation which holds the MPACT data). In the code, this part of the program is called `MPACT_libs`, specifically `Coupler_Redwing`. Very few data are exchanged between the Redwing master and sub apps: mainly the fuel pin array indices and the time step size. See Fig. 3.4 for an illustration of the design of Redwing for multiple-pin runs.

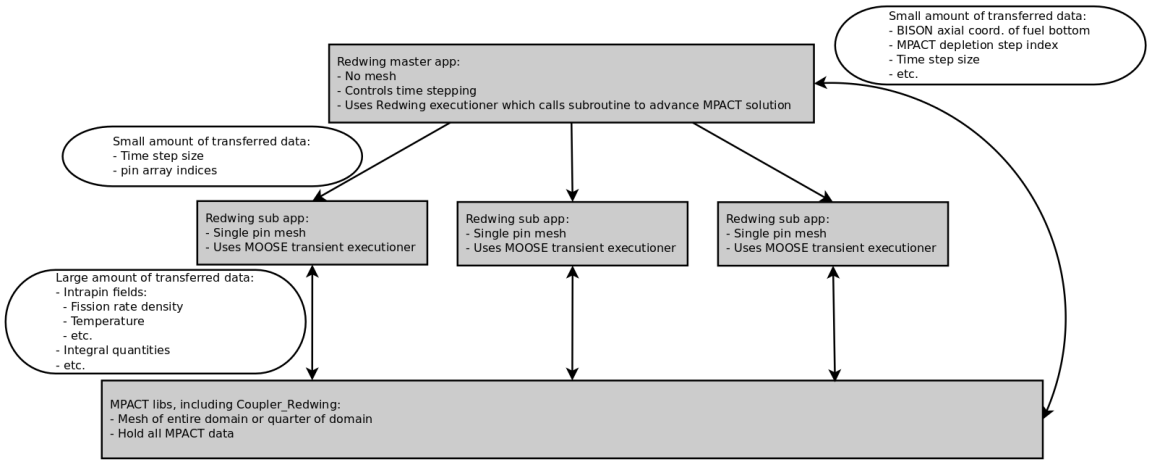

Figure 3.4: Design of Redwing for runs with multiple pins; the gray boxes are parts of the program and the arrows indicate data transfer.

J Validation of Redwing

An obvious first step in validating Redwing is to compare its results to the experimental data in BISON's assessment cases, assembled over time by the BISON team. Work has begun on validating Redwing; the first case considered is the Risø AN3 experiment [4]. The Risø AN3 experiment consisted of a series of non-destructive and then destructive tests carried out on a section of a PWR fuel rod. The fuel rod was originally irradiated in the Biblis A PWR and then re-fabricated to a shorter length with instrumentation. The experiment was carried out in the Risø DR3 water-cooled HP1 rig; it was a power bump test which lasted about 72 hours. The bump test refers to a ramp up to a high power (about 200% of the base irradiation average power), and then a sustained burn at this high power, as shown in Fig. 3.5.

The purpose of the experiment was to measure the effect of the power bump on the fuel temperature and fission gas release, and to obtain these data as a function of time. Experiments which provide time-dependent data are a powerful tool for testing computational models and validating codes compared to experiments which only provide data for the end of the experiment. The fuel temperature measurment was obtained with a thermocouple inserted into a small hole bored into the center of the top of the shortened rod. The thermocouple is not included in the model, although the thermocouple hole is; the simulation data corresponding to the thermocouple temperature are simply temperatures sampled at a fuel mesh node at the bottom of the thermocouple hole. The experimental fission gas released data were calculated based on pressure transducer measurements.

Figs. 3.6 and 3.7 show the experimental results plotted along with simulation results.

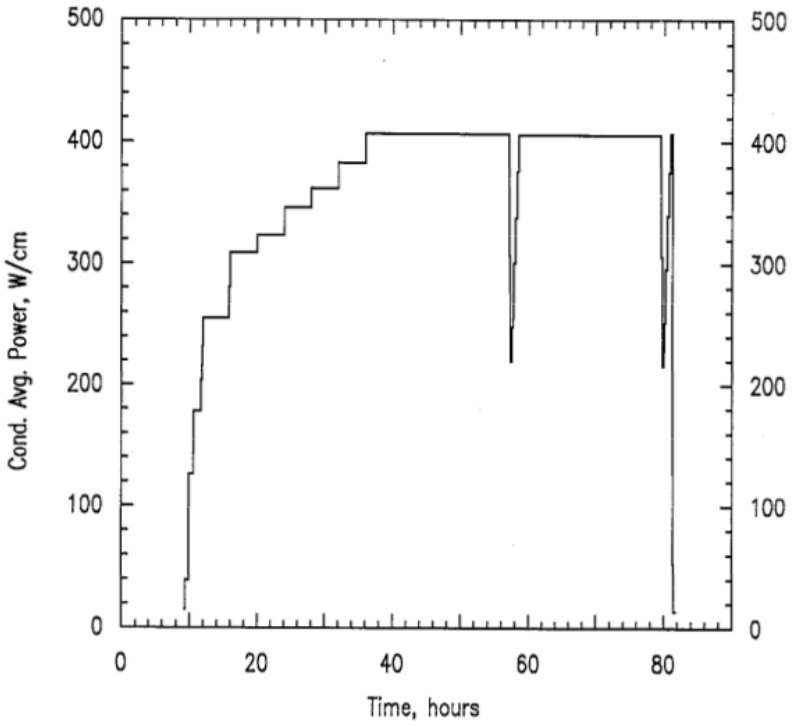

Figure 3.5: This is the rod-averaged linear power during the bump test [4].

Thus far, Redwing has yielded results which are generally in agreement with BISON, but with explainable differences; these will be discussed in the following chapters. Also, given the uncertainties in modeling fission gas release, the predictions of BISON and Redwing are fairly good. For this case, fission gas coupling results in an improvement in the prediction of fission gas release. Although all the computational models underpredict transient fission gas release at shudown, which occurs at about $t = 45$ hrs.

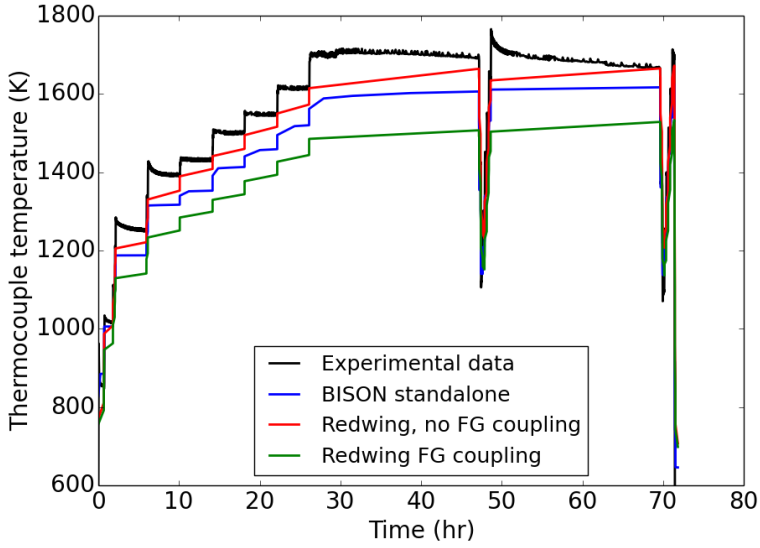

Figure 3.6: Experimental and simulated thermocouple temperature for the Risø AN3 experiment during the bump test. "FG" coupling refers to fission gas coupling. The data have been shifted so that the beginning of the ramp occurs at $t = 0$.

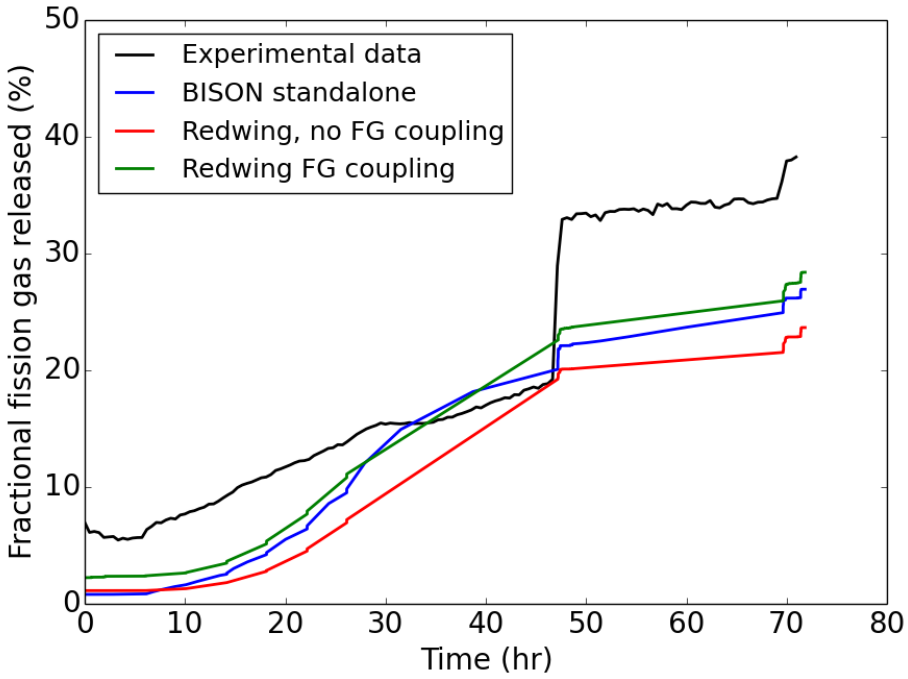

Figure 3.7: Experimental and simulated fractional fission gas released for the Risø AN3 experiment during the bump test. The data have been shifted so that the beginning of the ramp occurs at $t = 0$.

CHAPTER 4

General Coupled Fuel Depletion Simulation Results

In other applications in which neutron transport, nuclide depletion, and fuel performance have been coupled, there are generally agreed-upon data transfers. Usually neutron transport and nuclide depletion are coupled into a single program, like in the case of MPACT. Generally, the fission rate density or power density is transferred from the neutron transport and nuclide depletion program to the fuel performance program, and fuel and cladding temperature is transferred in the other direction [9, 10]. Many other data transfers are possible as well. Before fission gas data transfer is considered, Redwing results with decoupled fission gas will be examined.

In order to make the Redwing results more easily digestible, Table 4.1 gives an overview of the various coupling cases examined in this document and gives each a simple alphanumeric ID. These IDs are used throughout the results sections. The cases which contain an "X" are not considered in this work. This chapter contains results only for the decoupled fission gas cases: DFG0, DFG1, and DFG2.

Table 4.1: Labels for Redwing Coupling Cases

	Decoupled fission gas	Coupled fission gas
BISON	DFG0	X
One-way: Fission rate density, power density and fast flux transferred MPACT to BISON	DFG1	X
Two-way: fission rate density, power density and fast flux transferred MPACT to BISON; temperature transferred BISON to MPACT	DFG2	CFG2

In the interest of reproducibility, the version numbers or Git commit hashes are given in

Table 4.2 to show the exact versions of the codes used to obtain results in this and following chapters, or at least versions which may be used to duplicate the results presented. Redwing and all codes it depends on are under development. These results were obtained with a version of MPACT that was branched off of master on 2016 Oct. 30 in order to simplify the development process.

Table 4.2: Code versions used for this chapter

Code	Git SHA-1 hash or version number	Commit date
Redwing	`37fb39255b`	2017 Jun. 28
MPACT (branch)	`889de95e02`	2017 Jun. 28
MPACT (master)	`10bc0f11ce`	2016 Oct. 30
BISON	`34ebe05f3d`	2017 Jan. 11
MOOSE	`fe73a4caad`	2017 Jan. 17
libMesh	`5129e936af`	2016 Dec. 7
PETSc	`3.6.3`	2015 Jun. 9

A Watts Bar Nuclear 1 Single Pin Model Specifications

Redwing has been applied to several LWR simulations; here, the focus is on a Watts Bar Nuclear 1 (WBN1) fuel pin. The model consisted of a single PWR fuel pin based on the VERA Core Physics Benchmark Progression Problems from CASL [5], which in turn are based on the WBN1 reactor specifications. WBN1 is a Westinghouse-designed 17x17 assembly PWR, a typical design, built in Tennessee in the 1980s and 1990s [5]. The fuel pin geometry is shown in Fig. 4.1. Table 4.3 contains some specifications for the problem, and Fig. 4.1 shows more details about the problem geometry. Fig. 3.1 shows an example of the fuel pin mesh, which is slightly coarser than what was used in this chapter.

Originally, the BISON materials and contact models used to model the WBN1 fuel pin were based on the `US_PWR_16_x_16` assessment case in the BISON repository. After correspondence with ORNL in December 2016, the materials and contact models were updated to be similar to CASL's VERA model of WBN1. These models are more physically accurate. One of these changes was to use the kinematic formulation for the contact model, with a high penalty parameter of 10^{14}. Also, all Redwing cases were updated from the infinitesimal strain formulation to the finite strain formulation of the thermomechanics problem, which is necessary due to the amount of deformation that the WBN1 fuel rod experiences during several years of burnup. This made the Redwing simulations somewhat more expensive.

Table 4.3: Watts Bar Nuclear 1 single pin model specifications

Property	Value
Fuel pellet radius	0.4096 cm
Gap thickness	0.0084 cm
Cladding thickness	0.057 cm
Fuel rod pitch	1.26 cm
Fuel stack height	365.76 cm
Fuel rod height	385.1 cm
Fuel material	UO_2
Cladding and plugs material	Zircaloy-4
Fill gas material	helium
Initial ^{235}U enrichment	2.619 wt%
Linear power	21964 W/m
Simulated time	1825 days
Inlet temperature	565 K
Coolant pressure	15.5 MPa
Coolant inlet mass flux	3705.4 kg/(m^2-s)
Initial fuel density	94.5%

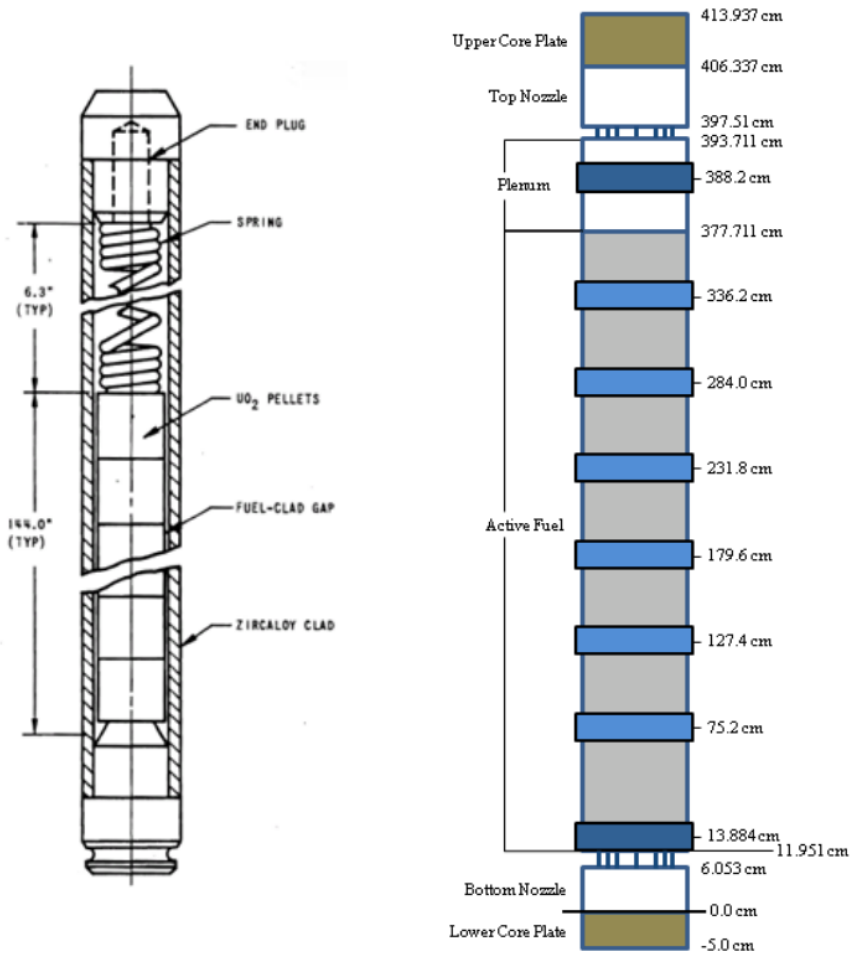

Figure 4.1: Left: the pin geometry, right: the axial details of the WBN1 single-pin model (note that this is a full assembly, but the model was a single pin) [5].

The MPACT part of the model is basically a scaled-down version of Benchmark Progression Problem 9, with a few modifications, including:

1. Only a quarter of a single fuel pin was modeled, rather than a quarter core.
2. The power history was simplified to have a 3-hour startup ramp and then a constant power (see Fig. 4.2)
3. The constant power was set to 120% of the average pin power in WBN1.
4. The ray spacing was decreased from 0.1 cm to 0.0064 cm.
5. 16 rather than 8 azimuthal directions were used for the angular quadrature set.
6. A 1 cm thick lower plenum was added to make the solid mechanics contact problem easier to converge.
7. Upper and lower axial water reflectors were added, each 20 cm thick
8. The 47-group MPACT transport cross section library, v4.1 was used
9. The MPACT internal depletion solver was used with the MPACT depletion library (`MPACT.dpl`).

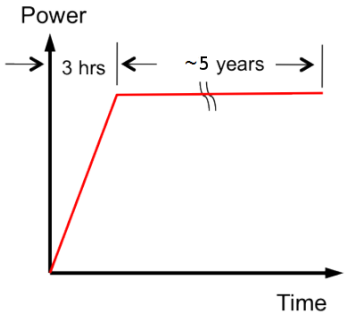

Figure 4.2: Watts Bar Nuclear 1 single pin model power history

The mesh density was increased in order to obtain a more accurate solution. Table 4.4 shows the mesh specifications for the single-pin WBN1 problem. The justification for the radial mesh used in the fuel is given in Ch. 5.

As shown in Fig. 4.1, the single-pin model includes an upper plenum; this is the part of the fuel rod above the fuel stack, which is simply a Zircaloy tube containing helium (initially). The small lower plenum is not shown. The union of the upper plenum, lower plenum and the fuel-cladding gap is the fuel-cladding plenum. The plenum volume, 17.3

Table 4.4: Mesh and time discretization for the single-pin Watts Bar model

Property	Value
Radial mesh elements in fuel (MPACT mesh)	16
Radial mesh elements in fuel (BISON mesh)	27
Radial mesh elements in coolant (MPACT)	10
Axial mesh elements in fuel (MPACT)	62
Axial mesh elements in fuel (BISON)	500
Polar rays per octant for MOC	3
Azimuthal angles per octant for MOC	16
Maximum Redwing time step size	20 days

cm^3, is almost evenly split between the upper and lower plena (54%) and the fuel-cladding gap (46%). The larger the combined volume fraction of upper and lower plena, the more ^{135}Xe is removed from shielding thermal neutrons streaming from the coolant into the fuel.

The Redwing simulations were performed with its prescribed thermal-hydraulics (TH) capability. Prior to all of the simulations described in this chapter, MPACT standalone was run with its internal TH solver and 16 radial fuel mesh elements in order to generate the prescribed TH HDF5 files.

B Watts Bar Nuclear 1 Single Pin Results

B.1 Cladding Lift-off

The switch to the CASL BISON materials models led to an important issue with high-burnup simulations; the early prediction of cladding lift-off. Clad lift-off is a phenomena observed in fuel rods where excessive fission gas release causes the fuel-cladding plenum pressure to rise far enough above the coolant pressure that the fuel-cladding gap reopens by a substantial amount [34]. This is a dangerous phenomenon; helium mixed with a substantial amount of fission gas has a much lower thermal conductivity than pure helium, so the gap thermal resistance for a given gap size is much higher than it would be in a fresh fuel rod.

With Redwing simulations, cladding lift-off begins when the plenum's pressure is about 14 MPa above the coolant pressure. Using the original materials models, this did not occur until about 1825 days of burnup, which was the end of the simulations detailed in the following section. With the materials and contact models update, cladding lift-off started at about 1360 days of burnup. The time at which cladding lift-off began was quite consistent for all cases with coupled fission gas that reached this point in the simulation. Fig. 4.3

shows the extreme deformation in the cladding after 1825 days that results from cladding lift-off. This is not a realistic scenario, because deformation to this degree would cause the cladding to burst, but models for failure mechanisms such as bursting were not included in the simulation. Also, the pressure applied by the spacer grids was not included in the boundary conditions for the the solid mechanics problem; that would have reduced the amount of cladding deformation.

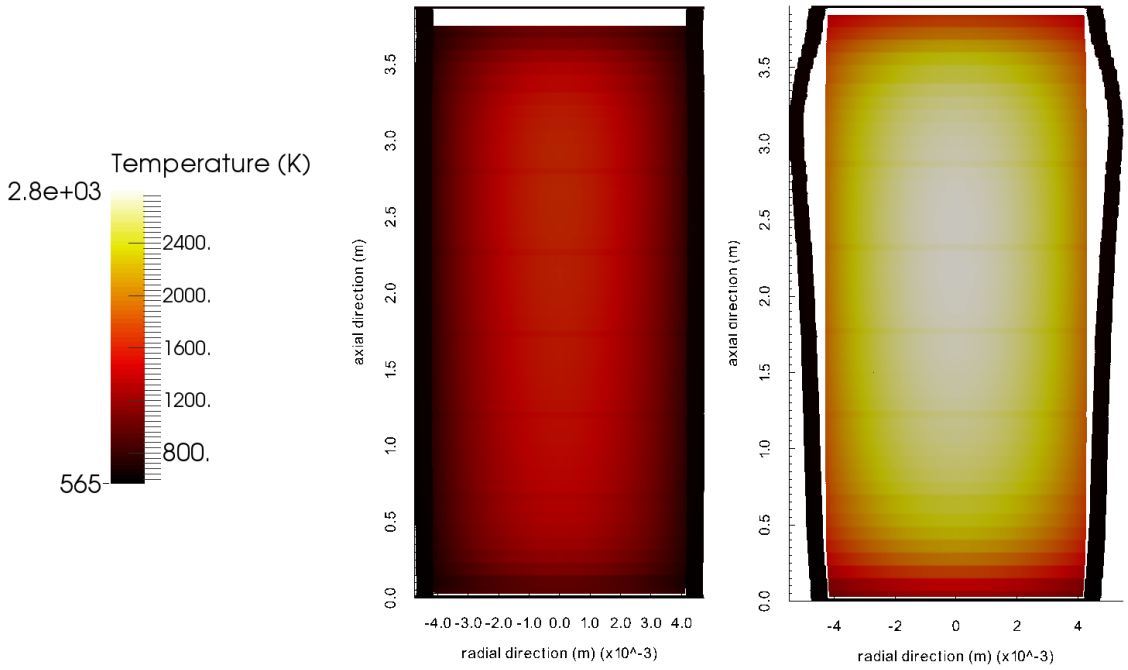

Figure 4.3: These are two cross sections along the centerline of the BISON mesh for a single-pin WBN1 Redwing simulation at constant power. The pin on the left is at t = 1280 days, and the pin on the right is at 1825 days. This particular model had 16 mesh elements between the centerline and fuel surface in the MPACT mesh and the maximum Redwing time step was 20 days.

B.2 Cases Simulated

Six cases were run:

1. DFG0, fast flux proportional to linear power density
2. DFG0, fast flux from DFG2 fixed-κ case
3. DFG1
4. DFG1, fixed-κ case
5. DFG2
6. DFG2, fixed-κ case

By default, Redwing uses a variable value of κ, the recoverable energy released per fission, because MPACT reads a different value of $\kappa\sigma_f$ (where σ_f is the microscopic fission cross section) for each fissionable nuclide in its transport library. This results in the pin-averaged value of κ to slowly change as the actinide inventory evolves with burnup. The standard BISON practice, however, is to use a fixed value of κ, $3.2 \cdot 10^{-11} \frac{\text{J}}{\text{fission}}$ for all simulations. In order to do Redwing simulations with a fixed value of κ, the fixed value must be applied in two parts of the code: where the power density field is computed in MPACT before transfer to BISON, and where the flux is normalized to pin power in MPACT's depletion module.

The DFG1 and DFG2 cases were run with prescribed TH, while DFG0 was run with BISON's internal enthalpy rise solver. In order to make a better comparison, the DFG0 runs used the same linear power density (i.e. magnitude and shape) as the DFG1 run with a fixed κ value. One DFG0 simulation also used the same fast flux magnitude as the DFG1 fixed-κ run; in this DFG0 simulation, the fast flux and linear power density had the same axial distribution, which is usual practice with BISON when the fast flux profile is not available from experimental data.

B.3 Results

BISON predicts a higher fission rate density (FRD) at the fuel surface; this is due to a more radially refined mesh used to calculate the FRD, which is independent of the finite element mesh used to discretize the rest of the problem. The radial FRD profile is calculated by the BISON class `BurnupFunction`, which uses the Lassmann model [3], a single-group neutron diffusion model, to obtain the radial profile. Hence, the BISON model of FRD is less

physically accurate than the MPACT prediction, but it allows the user to cheaply utilize a much higher radial discretization than with the MPACT model. In the results shown in this chapter, there are 100 points in the radial mesh used to calculate the FRD profile. Due to the highly surface-peaked FRD profile caused by the rim effect, BISON's simple model is likely predicting a more accurate surface FRD than MPACT simply due to its higher discretization, even if the model is less accurate for the interior of the pin. Still, the surface FRD is not an important quantity; Chapter 5 contains the justification for using only 16 elements to discretize the MPACT mesh between the centerline and the fuel surface.

There is an issue with the recoverable energy released per fission, or κ. As mentioned in Chapter 3, Redwing normalizes fields transferred from MPACT to BISON so that the integrated fuel rod power is the same on both meshes. The ratio of fuel rod power to fission rate is the average value of κ; this value is generally assumed to be constant, it actually changes slowly over the lifetime of the fuel. Fig. 4.5 shows that Redwing predicts that κ starts slightly higher than the fixed value used in BISON, $3.2 \cdot 10^{-11} \frac{\text{J}}{\text{fission}}$, and then rises slowly over time. Redwing's κ varies with burnup, due to the changing actinide inventory of the fuel. Tracking the changing actinide inventory allows Redwing to make a more physically accurate prediction of the FRD; because the FRD has a strong effect on most QOIs, variable-κ Redwing results are difficult to compare to BISON results. For this reason, some Redwing simulations were performed with κ fixed at $3.2 \cdot 10^{-11} \frac{\text{J}}{\text{fission}}$.

Fig. 4.4 shows that Redwing predicts a lower average FRD; this occurs because it uses a higher value of κ to calculate the FRD field, and therefore the fuel pin-averaged FRD is lower. The effect of the higher κ value can also be seen in Fig. 4.6, where the DFG1 variable-κ case has a lower value of net fission gas produced due to the lower average FRD.

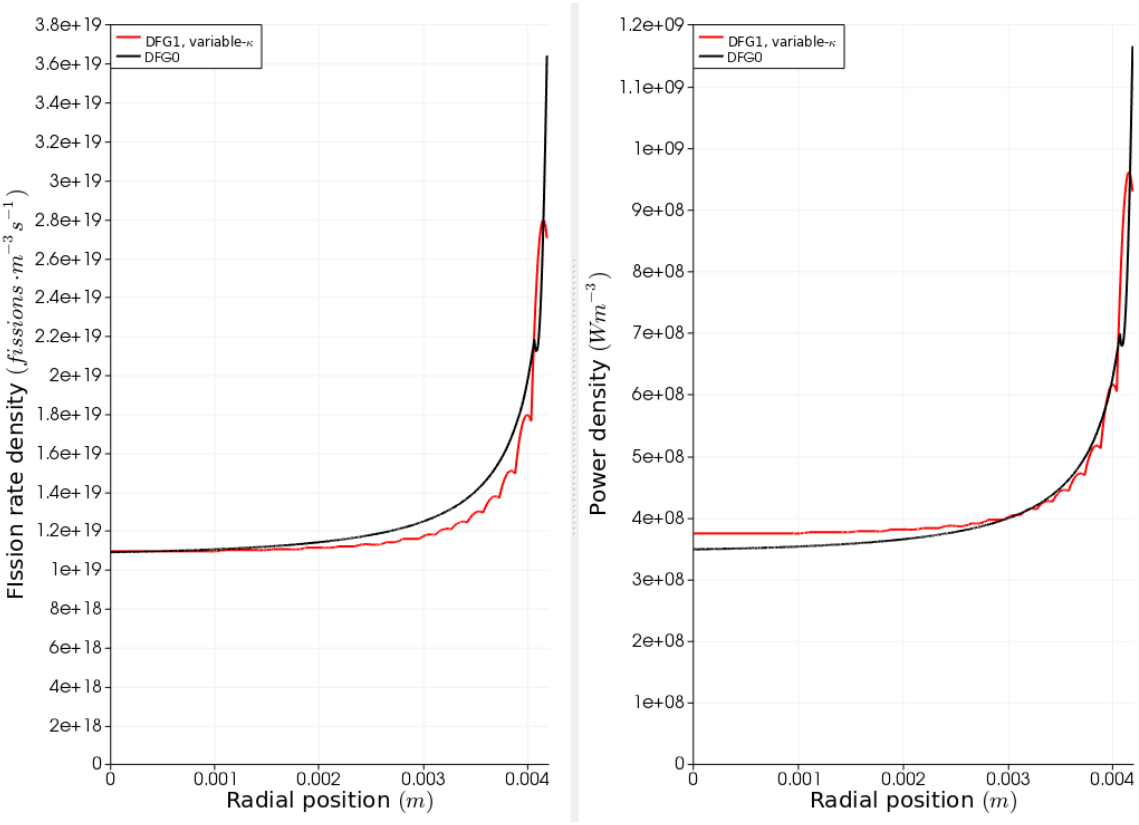

Figure 4.4: These are the radial profiles of fission rate density and power density at the rod midplane in the fuel. This figure compares BISON (DFG0) to Redwing with one-way coupling (DFG1) and variable-κ. DFG0 uses the fast flux from the DFG1 fixed-κ case.

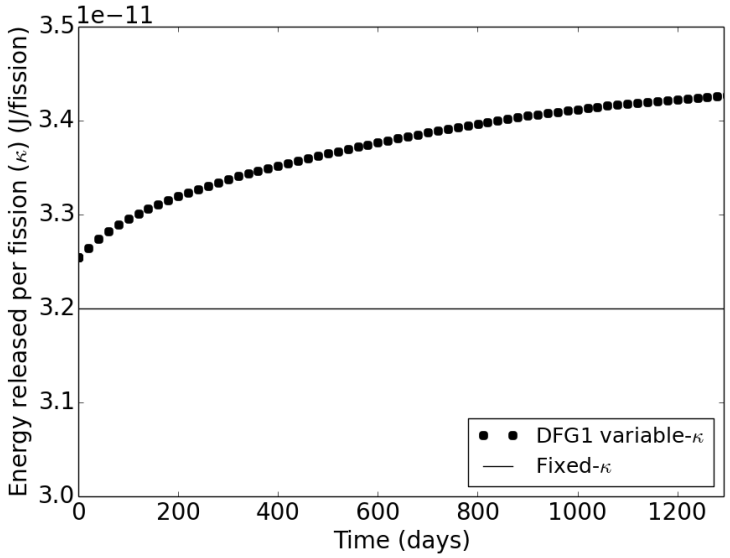

Figure 4.5: The pin-averaged κ vs. time for the case with variable κ (which is based on data from the MPACT depletion library). Also displayed is the κ value used for BISON and Redwing fixed-κ cases.

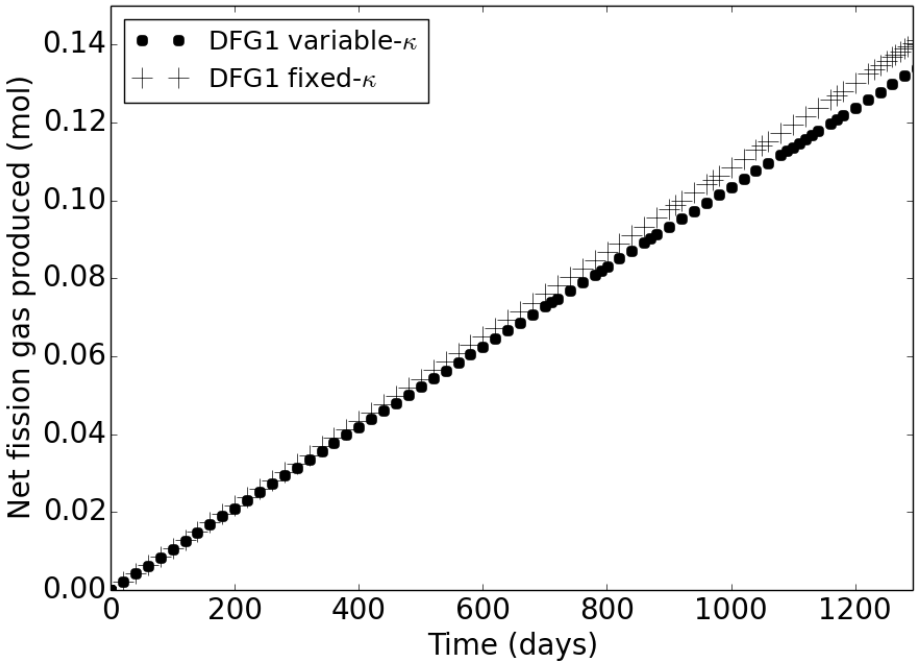

Figure 4.6: The net fission gas produced in two single-pin WBN1 DFG1 coupling cases. This shows the significant effect of using fixed-κ or variable-κ on the fission gas production.

The usual approach to calculating the fast flux field in BISON (i.e. DFG0) simulations is to assume that it is proportional to the linear heat rate (i.e. with a conversion factor) at a given axial location, which is workable but physically unrealistic; it is also possible for BISON to use a user-provided fast flux distribution, but this must be known a priori. The DFG0 conversion factors used in BISON assessment models and CASL's VERA WBN1 model yield an average fast flux value which is higher than that predicted by Redwing at the beginning of the simulation, but is lower by the end; see Fig. 4.7. The fast flux magnitude in Redwing is largely determined by the choice of which energy groups are considered to contain fast neutorns. In the Redwing WBN1 model, the minimum energy cutoff for fast flux is set at 1.35 MeV, which is the lower bound of the fourth energy group for the neutron transport library [35]. Fig. 4.7 also shows that the fast flux rises slowly in the DFG1 cases, which is expected to occur as the neutron flux spectrum hardens with burnup. A third important feature of Fig. 4.7 is the difference caused by the κ treatment in the DFG1 cases. The magnitude of the fast flux starts slightly higher in the case with fixed-κ, and the difference slowly increases with burnup as κ rises in the variable-κ case, and concurrently the overall flux magnitude decreases.

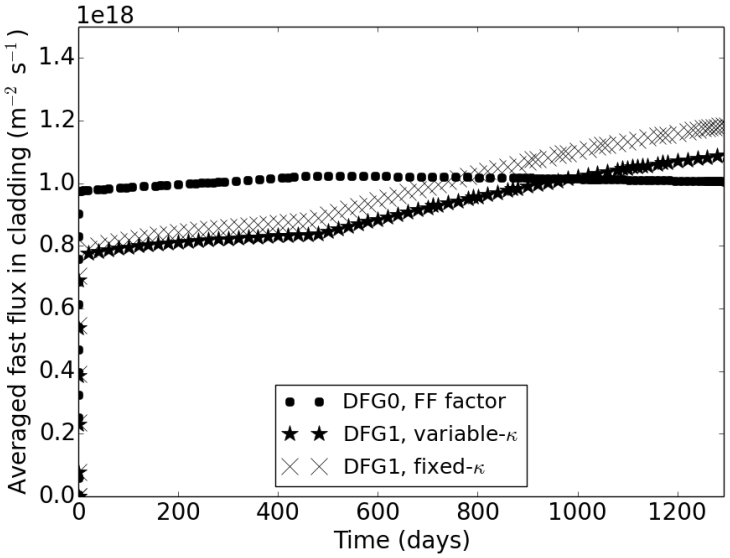

Figure 4.7: The fast neutron flux averaged over the pin's cladding for three single-pin WBN1 cases.

As shown in Fig. 4.8, the fuel-cladding gap closed faster in BISON than in Redwing; this is mostly due to the fact that the BISON case underwent almost twice as much radial thermal expansion as Redwing at the beginning of the simulation, even though both simulations are using the same thermal expansion model. This likely occurs because the overall thermomechanics model (including thermal contact and fuel thermal expansion) at the beginning of the simulation is sensitive to small differences in power density shape; this issue requires further investigation. As the gap closed, the gap conductance increased and the fuel temperature reached a minimum; by comparing Figs. 4.8 and 4.9, one can see that the fuel temperature reached a minimum when the average gap width falls below 0.01 mm.

As expected, Fig. 4.10 shows that a greater average fuel temperature correlates with a greater percent fission gas released. This occurs because higher fuel temperatures promote faster diffusion of fission gas from fuel grain interiors to grain boundaries. Fig. 4.10 also shows that, for each treatment of κ, one-way and two-way coupling have nearly the same fission gas released, with two-way coupling resulting in slightly higher fission gas released. For nearly all QOIs, the results from one-way and two-way coupling are nearly the same, with the exception of cladding-averaged fast flux.

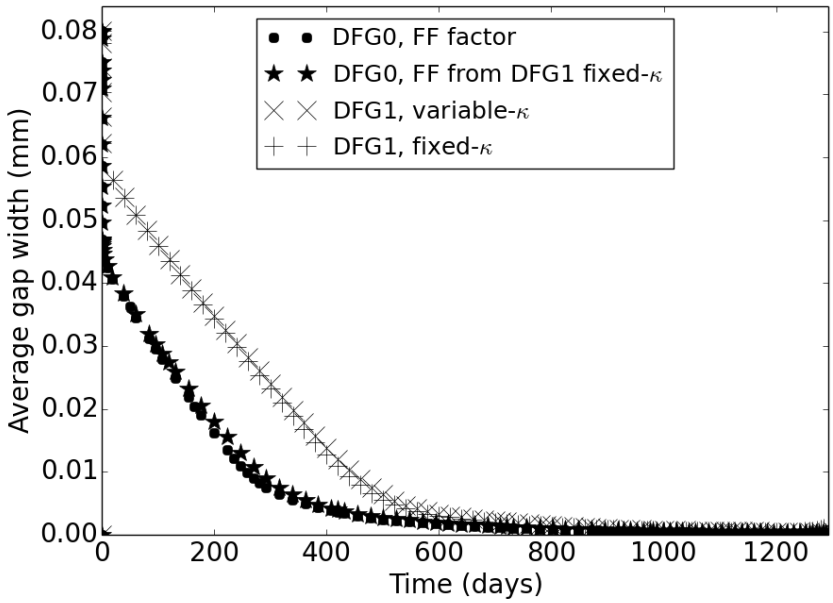

Figure 4.8: The axially-averaged gap width for four single-pin WBN1 cases.

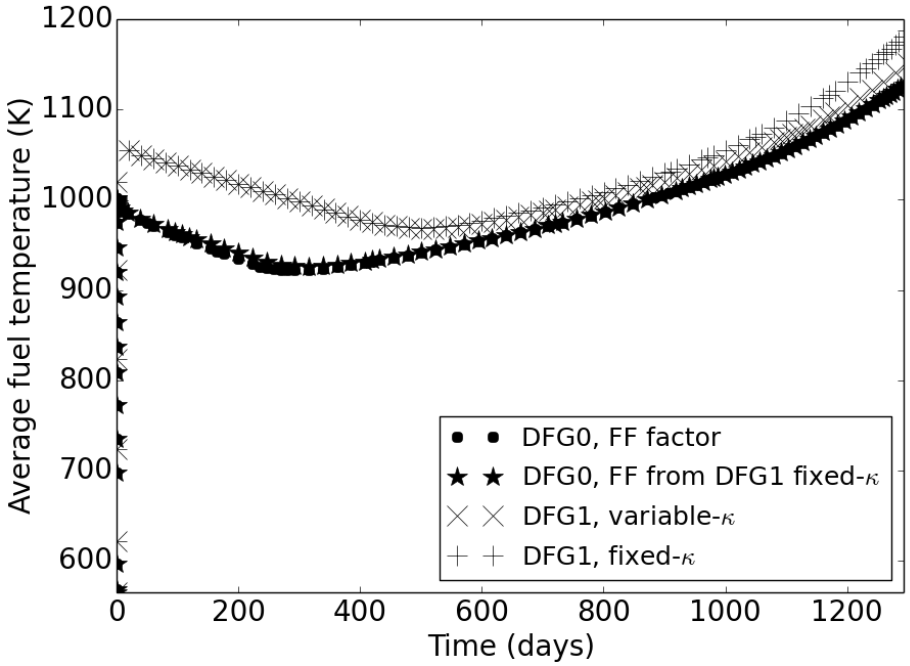

Figure 4.9: The average fuel temperature for four single-pin WBN1 cases.

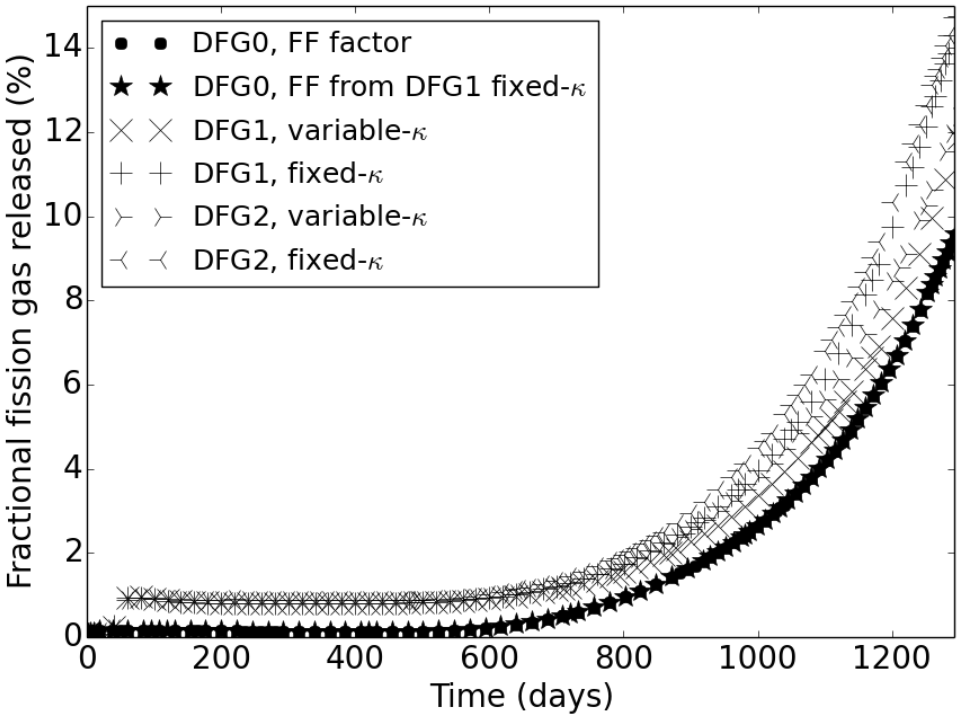

Figure 4.10: The fission gas released as a percentage of the fission gas generated for all six single-pin WBN1 cases.

Redwing has higher fidelity models than BISON of certain physical phenomena, such as fast flux and the energy relased per fission; although these phenomena are generally regarded as minor issues, this chapter has illustrated that they can have significant effects on QOIs over the lifetime of a fuel rod. Unfortunately, using more realistic models does not guarantee that the predictions of QOIs are more physically accurate; Redwing must be validated against experimental data before its predictions can be trusted. Redwing has the potential to match experimental data better than BISON, as seen with the simulations of the Risø AN3 experiment (Fig. 3.7), but it has yet to be demonstrated to make reliably better predictions. Now that two-way coupling has been demonstrated, the next chapter will focus on fission gas coupling.

CHAPTER 5

Fission Gas Coupling Results: Single Watts Bar Fuel Pin

Algorithm 4 was implemented in MPACT and Redwing. A few small changes were also made to the Sifgrs module in BISON in order to calculate the fission gas source based on data transferred from MPACT's Bateman solver. The focus of this chapter is Redwing cases with coupled fission gas fields. The cases DFG1, DFG2, and CFG2 will be considered in this chapter (see Table 5.1).

Table 5.1: Labels for Redwing Coupling Cases

	Decoupled fission gas	Coupled fission gas
BISON	DFG0	X
One-way: Fission rate density, power density and fast flux transferred MPACT to BISON	DFG1	X
Two-way: fission rate density, power density and fast flux transferred MPACT to BISON; temperature transferred BISON to MPACT	DFG2	CFG2

While examining the output of the cases presented in this chapter, small fluctuations in the power density shape in the fuel were observed; this is due to an instability in the solution. Fortunately, oscillations caused by this instability do not grow with time. The power density shape is supposed to evolve slowly with depletion, without its axial peak oscillating back and forth. In order to quantify this fluctuation, the L^2-norm of the rate of change of the power density was added as a `Postprocessor` in Redwing. The rate of change was measured, rather than the change in power density, in order to make a consistent comparison between cases with different Redwing time steps. Eq. (5.1) is an expression

for L^2, the L^2-norm of the rate-of-change of the power density, for a time step from time i to $i+1$.

$$L^2 = \sqrt{\int_{\text{fuel}} d\mathbf{r} \left(\frac{q'''^{(i+1)} - q'''^{(i)}}{\Delta t^{(i+1)}} \right)^2} \tag{5.1}$$

A Watts Bar Fuel Pin Model Specifications

The Watts Bar fuel pin model is based on the same specifications from Chapter 4. Table 4.3 contains pertinent geometrical specifications and operational parameters for the fuel pin. Table 5.2 contains information on the spatial and temporal discretization of the model. Like with the last chapter, Redwing was run with its prescribed TH treatment. Unlike the last chapter, most simulations in this chapter were performed with the fast neutron flux consisting of the six highest-energy flux groups, so that the lower fast flux energy cutoff was 0.5 MeV.

Table 5.2: Mesh and time discretization for the single-pin Watts Bar base case

Property	Value
Radial mesh elements in fuel (MPACT mesh)	4
Radial mesh elements in fuel (BISON mesh)	11
Radial mesh elements in coolant (MPACT)	10
Axial mesh elements in fuel (MPACT)	62
Axial mesh elements in fuel (BISON)	500
Ray spacing for MOC	0.0064 cm
Polar rays per octant for MOC	3
Azimuthal angles per octant for MOC	16
Maximum Redwing time step size	20 days

B Constant Power Analysis

B.1 Sensitivity Study of the Radial Fuel Mesh

It is very important to have a sufficiently refined radial fuel mesh due to the rim effect and the large thermal gradient in the radial direction. Therefore, the radial fuel mesh density was the primary parameter considered in this sensitivity study. Four cases of the Watts Bar fuel rod were run with fission gas coupling. In each successive case, the radial density of the MPACT fuel mesh was increased by a factor of 2. The radial mesh density in BISON

was increased as well, but not in a regular manner. The BISON mesh consists of quadratic finite elements, so it is able to represent solution fields in more detail than the MPACT mesh. Also, with the current data transfer methods, there must be a single BISON mesh element centroid in each MPACT flat source region. Hence, the minimum BISON radial mesh density which satisfied this requirement was used in each case. See Table 5.3 for the BISON radial mesh used in each case.

Table 5.3: Number of radial mesh elements in fuel for the Watts Bar fuel pin model

MPACT	BISON
4	11
8	12
16	27
32	57

Increasing the radial fuel mesh incurs a computational cost in memory required and wall time. All simulations mentioned in this chapter were run on a single node of INL's Fission supercomputer, with 25 processors. Table 5.4 shows the wall time required for each simulation. The Redwing time steps which occured during were very time consuming, with some single time steps taking six or more hours for the 16/27 radial meshing case.

Table 5.4: Wall times for radial mesh sensitivity study run on one Fission node

Case	Wall time (hr)
4/11	8.8
8/12	8.3
16/27	18.5
32/57	30.8*

*This is the wall time taken to reach a simulation time of 1400 days. This case failed on the time step to 1420 days.

Figures 5.1-5.7 show the evolution of quantities of interest for the normal gap case. According to Fig. 5.7, the fission gas released shows a large decrease when the radial mesh is refined from 4/11 to 8/12 mesh elements. A decrease is expected because with refinement of the MPACT mesh, the fission rate density becomes more peaked at the fuel surface, where the temperature is lower, and therefore fission gas released is lower; however, increasing the radial mesh density further causes the fission gas released to increase.

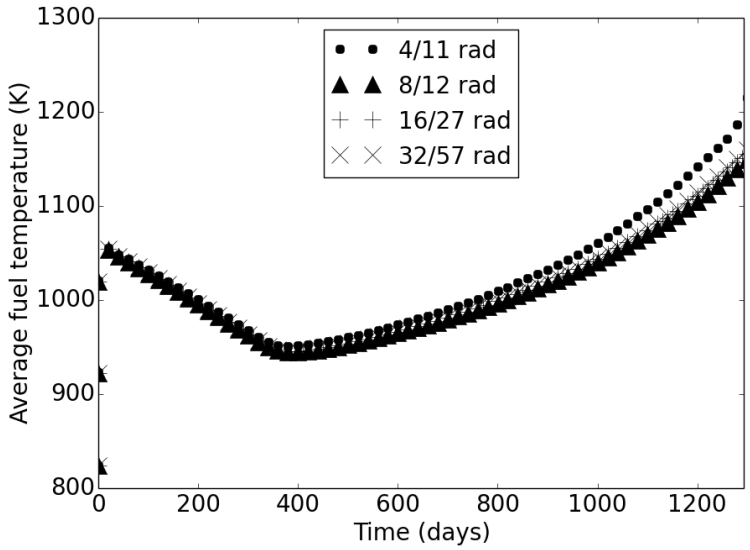

Figure 5.1: This is the average fuel temperature for four radial meshing cases of the WBN1 constant power simulations. The cases are reported as the number of MPACT radial mesh elements / the number of BISON radial mesh elements.

Fig. 5.2 shows that the gap closes at about $t = 600$ days, regardless of the radial meshing. An important note here is that, by comparing Fig. 5.2 and Fig. 5.6, that fission gas release does not occur until after the gap has closed, which simplifies the coupled problem, as all the fission gas released is transported to the upper plenum with the current algorithm.

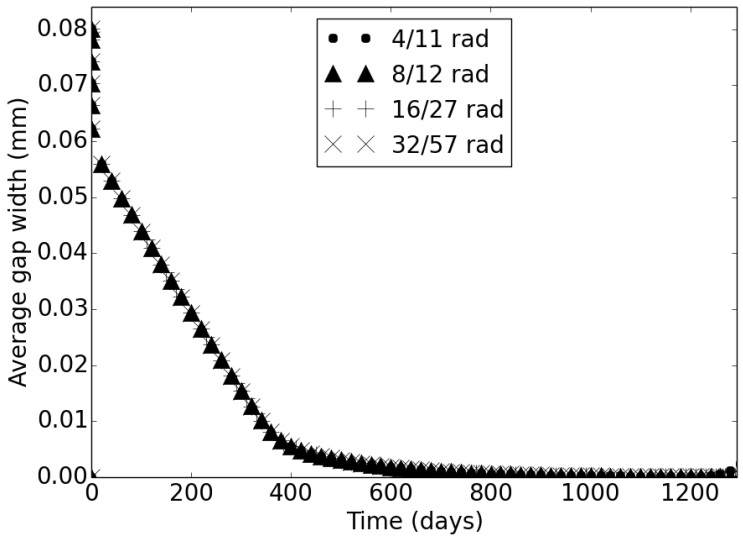

Figure 5.2: The axially-averaged gap width for four radial meshing cases of the WBN1 constant power simulations.

The maximum cladding hoop strain, shown in Fig. 5.3, shows agreement between cases except for the 4 radial mesh element case. By $t = 1280$, the maximum cladding strain is just below 1% for the 3 cases with the highest mesh density; this is the NRC's limit for uniform strain, although the limit applies to overall strain of the cladding, not the maximum strain at a point. The radial mesh density has a fairly small effect on QOIs such as k_{eff} and net fission gas produced (Figs. 5.4 and 5.5, repsectively). As stated above, radial mesh density had a large effect on fission gas released, as shown in Figs. 5.6 and 5.7; this resulted in a significant effect on the fuel fission gas inventory, as shown in Fig. 5.8.

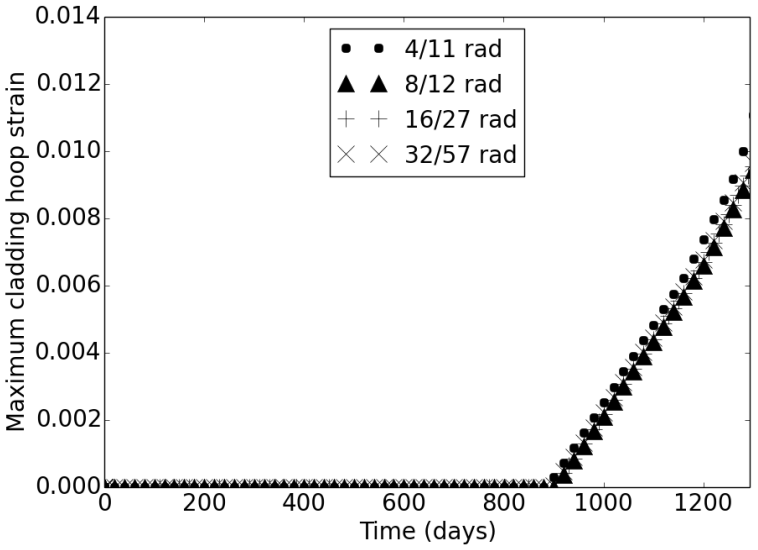

Figure 5.3: The maximum cladding hoop strain for four radial meshing cases of the WBN1 constant power simulations.

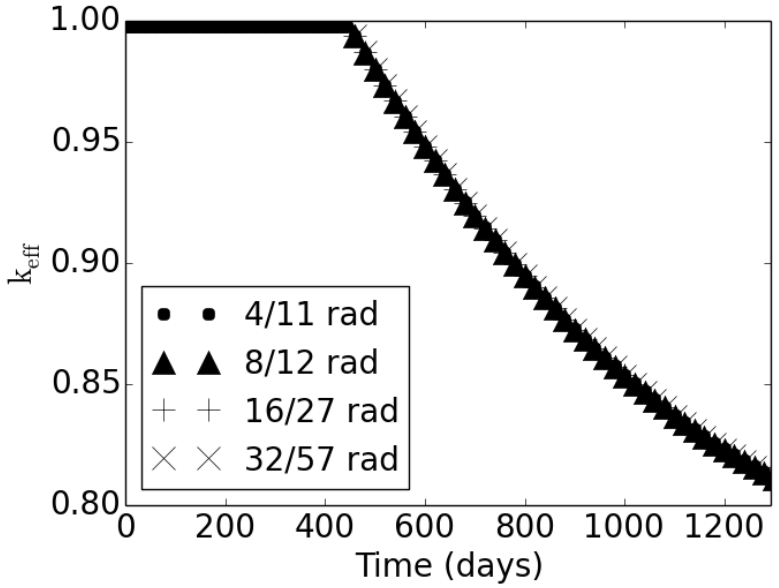

Figure 5.4: The neutron transport eigenvalue (for an infinite pin array) for four radial meshing cases of the WBN1 constant power simulations.

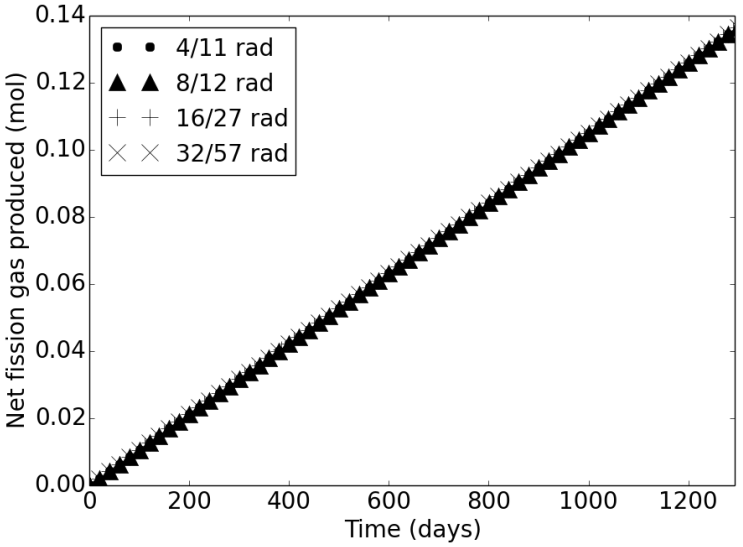

Figure 5.5: The net fission gas produced for four radial meshing cases of the WBN1 constant power simulations.

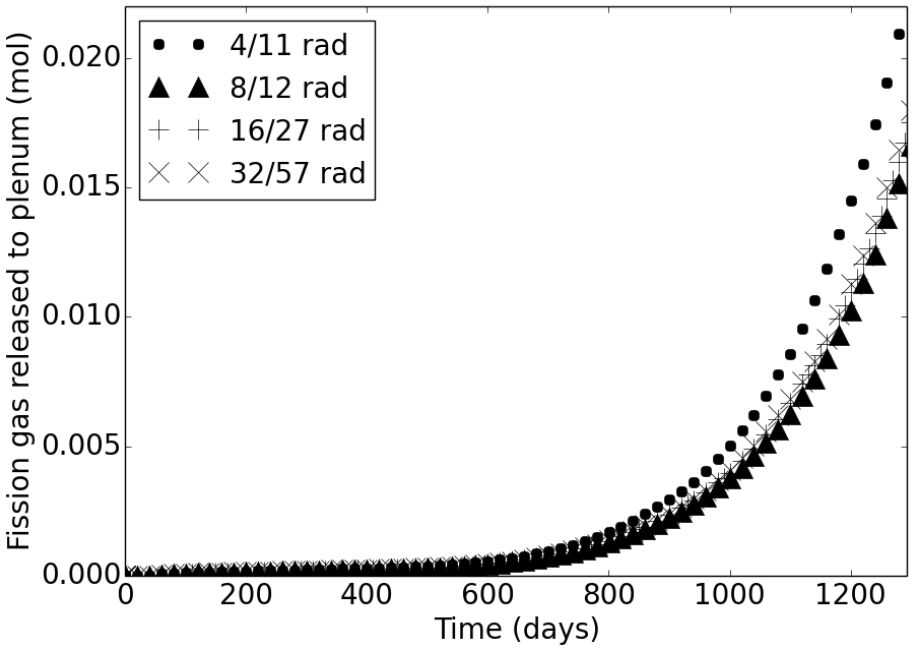

Figure 5.6: The fission gas released for four radial meshing cases of the WBN1 constant power simulations.

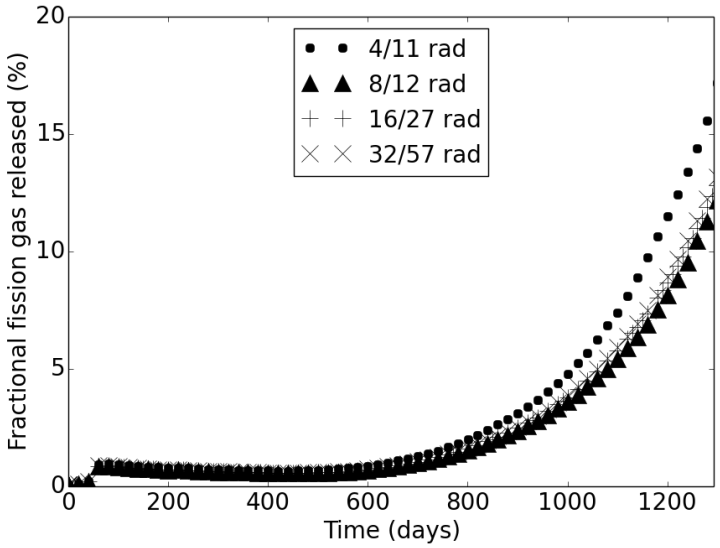

Figure 5.7: This is the percent fission gas relased for four radial meshing cases of the WBN1 constant power simulations. The quantity displayed is relative to the net fission gas produced.

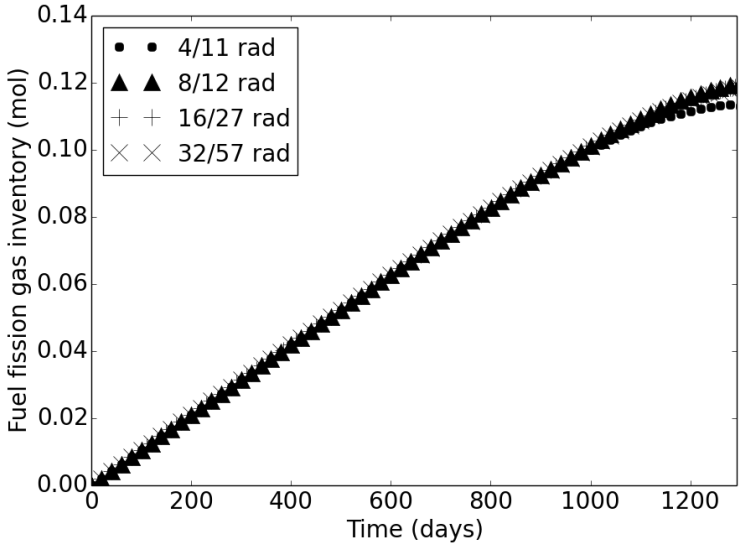

Figure 5.8: The fuel fission gas inventory for four radial meshing cases of the WBN1 constant power simulations.

Fig. 5.9 indicates that the solution is somewhat stable, due to the fact that the L^2-norm remains at a low value relative to the beginning of fuel life. The L^2-norm steadily falls and reaches a somewhat steady value at about 10^{-2}, other than upticks at 220 day intervals, when the subgroup calculation is performed by MPACT. The subgroup calculation causes an abrupt change in the neutron cross sections, which results in a slight change in the power density shape.

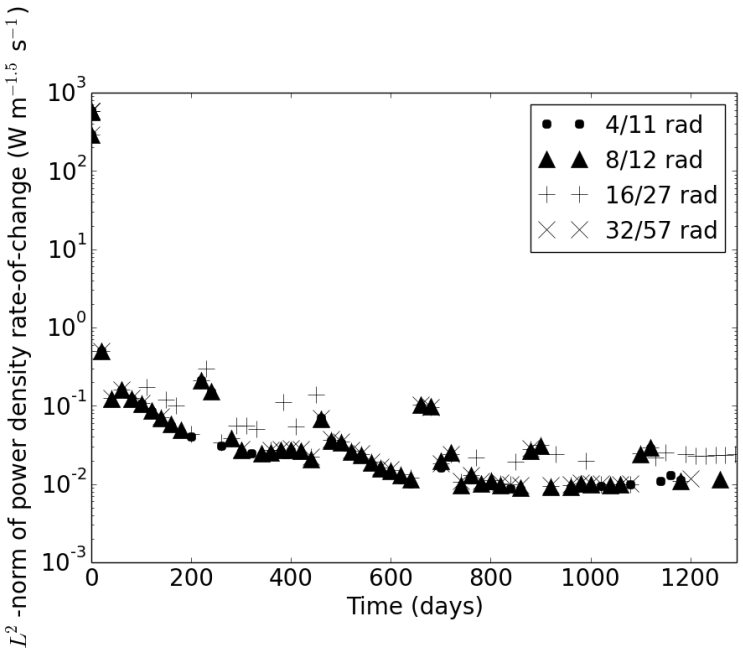

Figure 5.9: The L^2-norm (over the BISON mesh) of the power density rate-of-change for four radial meshing cases of the WBN1 constant power simulations

Table 5.5 shows differences in the QOIs. At the end of the simulation, t = 1280 days, the differences in the QOIs between the 16/27 and 32/57 MPACT/BISON radial mesh cases were only a few percent, suggesting that the 16/27 radial mesh case is sufficiently refined. The difference in both fission gas released and plenum fission gas inventory between the 16/27 and 32/57 cases is only -3%, which is encouraging; these are the two most important QOIs in this study. Figure 5.7 shows the evolution of the percent fission gas released; the small bump in this quantity at t = 60 days is likely transient fission gas release triggered by a change in temperature; it corresponds to a small amount of fission gas release.

Table 5.5: Relative differences in quantities of interest and absolute difference in k_{eff} compared to the most refined case at t = 1280 days for the MPACT/BISON radial mesh sensitivity study

Output quantity	Finest: 32/57 rad	4/11 rad	8/12 rad	16/27 rad
Avg. fuel temperature	1150 K	3.16%	-0.92%	-0.40%
Max. fuel temperature	1646 K	3.64%	-0.94%	-0.37%
Max. cladding hoop strain	0.00907	10.15%	-2.28%	-1.04%
Fractional FG released	12.25%	27.23%	-7.90%	-3.35%
Net FG produced	0.134 mol	-0.01%	-0.01%	-0.00%
Plenum FG inventory	0.0164 mol	27.23%	-7.87%	-3.37%
FG released to plenum	0.0165 mol	27.22%	-7.90%	-3.36%
k_{eff}	0.813315	43 pcm	2 pcm	6 pcm

B.2 Sensitivity Study of the Redwing Time Step

It is important to check the sensitivity of the coupled solution to the time step size, because the MPACT and BISON solvers are loosely coupled. To perform this check, all time steps after the startup ramp were reduced: the base case was dt = 20 days, the other cases were dt = 10, 5, and 2.5 days. The BISON solver attempted to match the time step of each Redwing step; however, If a BISON solve failed, the time step would be reduced to half the size of the Redwing time step. All cases had the 16/27 radial meshing. Table 5.6 shows the wall time taken by each simulation. As expected, there is a decrease in wall time as dt is increased from 2.5 to 10 days, but an increase as dt is increased to 20 days; this is due to a larger number of failed solves in the BISON solver, which necessitated more recovery time steps than the dt = 10 days case.

Table 5.6: Wall times for time step sensitivity study using one Fission node

Case (dt in days)	Wall time (hr)
2.5	32.5
5	22.5
10	15.8
20	18.5

Table 5.7 shows the differences in QOIs compared to the most refined case, dt =2.5 days. As expected, most QOIs show improvement in accuracy with the reduction in the time step size, such as the percent fission gas released. Two exceptions to the expected behavior are the maximum cladding hoop strain and net fission gas produced. The relative error in maximum cladding hoop strain hovers around 0.8%, which is acceptably small. The net fission gas produced is significantly higher for the dt = 5 days case than the less-

refined cases. This behavior is likely the result of time-integration error due to using loose fission gas coupling along with MPACT's internal fuel depletion solver, resulting in the overproduction of Xe and Kr gas. Although unexpected, this increase in error is small, with only a 1.5% difference between the dt = 5 days and the dt = 2.5 days cases. Plots for net fission gas production and fuel fission gas inventory are not included because these QOIs are nearly the same for all cases.

Table 5.7: Relative differences in quantities of interest and absolute difference in k_{eff} compared to the most refined case for the time step sensitivity study

Output quantity	Finest: dt =2.5 days	20 days	10 days	5 days
Avg. fuel temperature	1140 K	0.53%	0.46%	0.34%
Max. fuel temperature	1633 K	0.40%	0.42%	0.29%
Max. cladding hoop strain	0.00891	0.71%	0.83%	0.79%
Fractional FG released	11.11%	6.56%	5.54%	3.13%
Net FG produced	0.134 mol	0.60%	0.61%	1.47%
Plenum FG inventory	0.0147 mol	7.62%	6.73%	5.00%
FG released to plenum	0.0149 mol	7.20%	6.18%	4.65%
k_{eff}	0.813385	0 pcm	3 pcm	-2 pcm

Although the dt = 20 days case has significant relative error in the fission gas released and the plenum fission gas inventory at 7% to 8%, this time step size was chosen to run further simulations. The reduction in error with decreasing time step is only a few percent (i.e. first-order convergence is not observed for the chosen time step sizes), so using a time step size smaller than 10 days is not worth the increase in computing time. The time-integration error in net fission gas produced in the fuel (mentioned above) results in the slow error reduction in the QOIs: fission gas released and plenum fission gas inventory.

Figs. 5.10 and 5.11 show effects of changing the time step size. By default, Redwing makes the MPACT and BISON solvers take the same time step, but sometimes BISON is subcycled in order to achieve convergence. The time step sizes reported are those set by Redwing; for all cases BISON had to be subcycled on at least a few Redwing time steps. The periodic increases in the L^2-norm of the power density rate-of-change observed in Fig. 5.9 can also be seen in Fig. 5.11. Decreasing the time step did not reduce the L^2-norm for all time steps; in fact, the cases with smaller time steps show a greater increase in the L^2-norm when the subgroup calculation occurs; this suggests the L^2-norm changes by a fixed amount regardless of time step size. Between the periodic increases in the L^2-norm, the quantity generally stays at a value of 0.1 W $m^{-1.5}$ s^{-1} or below. During this period, the dt = 20 days case is elevated relative to the other cases at several points in time, likely due to an instability in the solution.

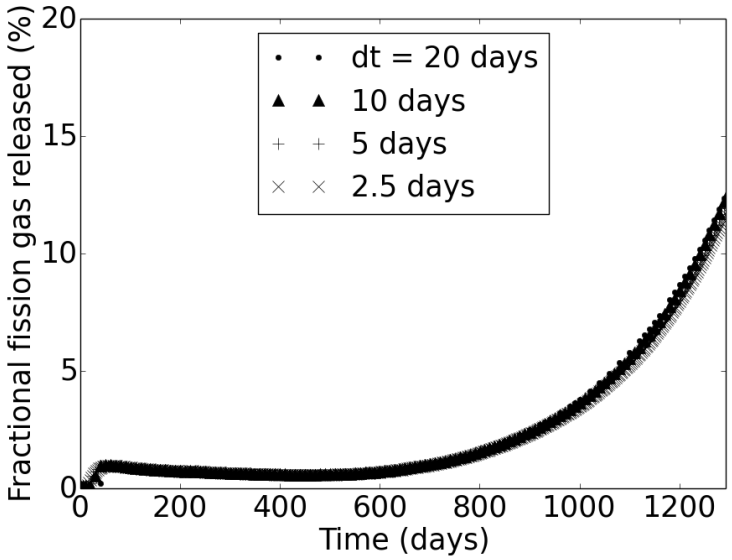

Figure 5.10: This is the percent fission gas relased for four time step cases of the WBN1 constant power simulations. The quantity displayed is relative to the net fission gas produced. 16/27 radial fuel meshing was used.

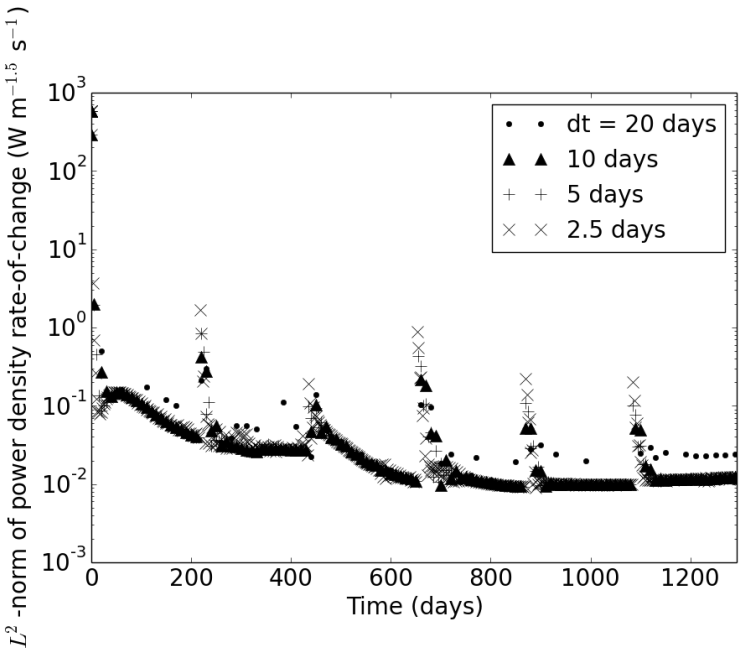

Figure 5.11: This is the L^2-norm of the power density rate-of-change for four time step cases of the WBN1 constant power simulations. 16/27 radial fuel meshing was used.

B.3 Effect of Fission Gas Coupling

The primary way to evaluate fission gas coupling is to compare two cases which are identical except for the activation of fission gas coupling. The Redwing case with 16/27 radial fuel meshing and dt = 20 days was simulated with coupled and decoupled fission gas. With decoupled fission gas, the plotted results are those calculated by Sifgrs, which assumes the fission gas (FG) yield is simply $0.3017 \frac{\text{FG atoms}}{\text{fission}}$. Table 5.8 shows the effects caused by enabling fission gas coupling; for decoupled fission gas, the fission gas quantities reported are those calculated by the BISON solver. Table 5.8 also includes the case of one-way MPACT to BISON coupling with decoupled fission gas.

Table 5.8: Relative differences in quantities of interest and absolute difference in k_{eff} caused by fission gas coupling at t = 1280 days.

Output quantity	Reference: DFG2	CFG2	DFG1
Average fuel temperature	1135 K	0.97%	-0.03%
Maximum fuel temperature	1618 K	1.38%	-0.27%
Maximum cladding hoop strain	0.00861	4.25%	1.70%
Fractional fission gas released	11.02%	7.90%	-1.16%
Net fission gas produced	0.132 mol	1.92%	-0.02%
Plenum fission gas inventory	0.0145 mol	9.62%	-1.17%
Fission gas released to plenum	0.0145 mol	9.97%	-1.17%
k_{eff}	0.812760	62 pcm	435 pcm

Fig. 5.12 shows a slight increase in the net fission gas production due to coupling fission gas; the higher fission gas production rate is the result of solving the Bateman equations for the fission gas concentrations, which accounts for many physical phenomena that BISON's simple Sifgrs source ignores. As burnup increases, more plutonium is fissioned; although the overall independent yield of fission gas from plutonium nuclides is slightly lower than that of ^{235}U, the yield of certain nuclides, like ^{135}Xe, is higher. Also, as the neutron spectrum hardens with burnup, fission gas atoms are less likely to capture neutrons, which tends to decrease their rate of transmutation into non-gaseous species. The higher fission gas production in the fuel and slightly higher fuel temperature results in a higher amount of fission gas released for the case with fission gas coupling, shown in Fig. 5.13 shows the increase in fission gas released caused by fission gas coupling. According to Table 5.8, there is a significant increase of about 9% in plenum fission gas inventory and fission gas released at the end of the simulation; as expected, fission gas coupling also affected the overall solution to the coupled problem, as evident in the change in maximum fuel temperature and maximum cladding hoop strain. The increased fission gas released for fission gas coupling is likely not due to an instability, as the coupled and decoupled fission gas profiles show

nearly the same L^2-norm of the power density rate-of-change throughout the simulation; see Fig. 5.14. It is likely that the higher fission gas released with coupled fission gas is mostly due to the small increase in net fission gas production. If this is so, it is likely that some of the discrepancies between CFG2 and DFG2 may be reduced simply by increasing the accuracy of the fission gas source in BISON's Sifgrs module.

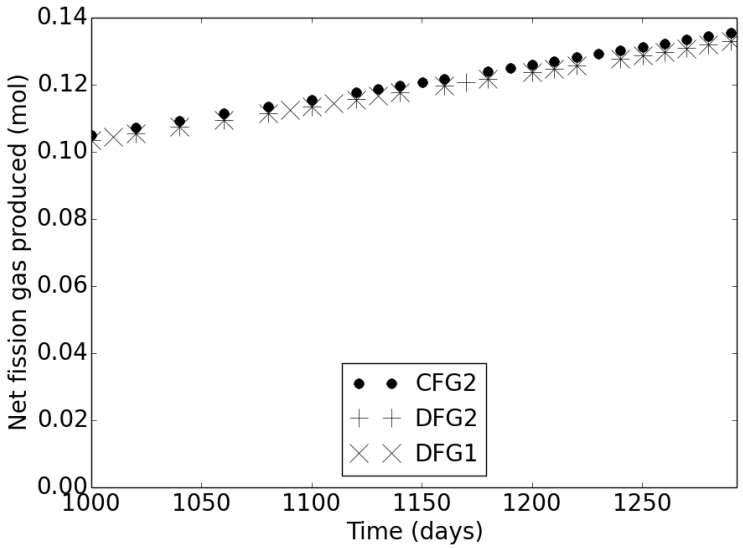

Figure 5.12: This is a comparison between coupled and decoupled fission gas cases of net fission gas generated near the end of life for the WBN1 fuel pin model.

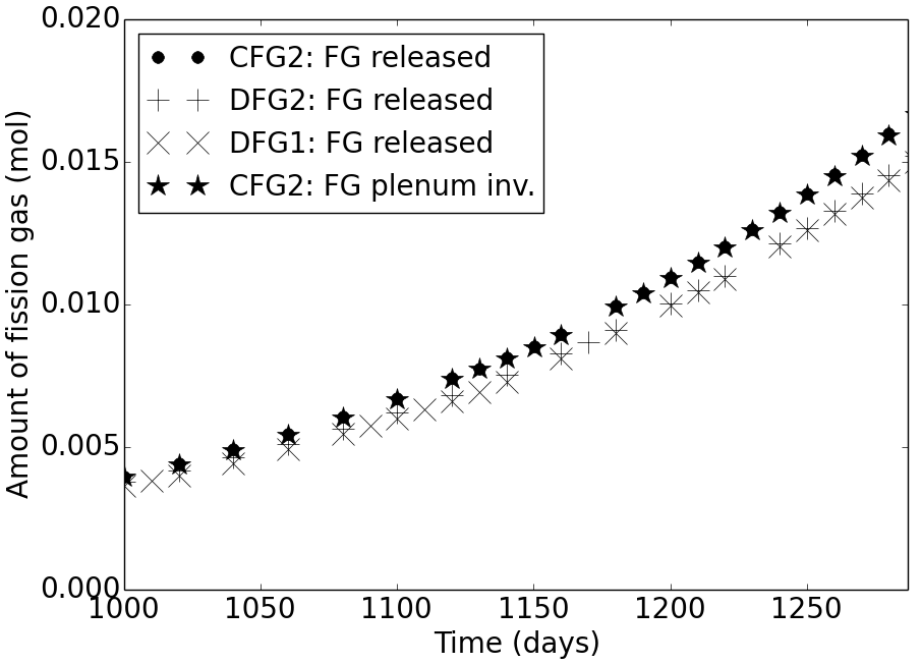

Figure 5.13: This is a comparison between several plenum fission gas (FG) quantities near the end of life for the WBN1 fuel pin model: the FG released and plenum inventory for the case with coupled FG and 2 way coupling, and the FG released for 2 way coupling with decoupled FG and 1 way coupling with decoupled FG.

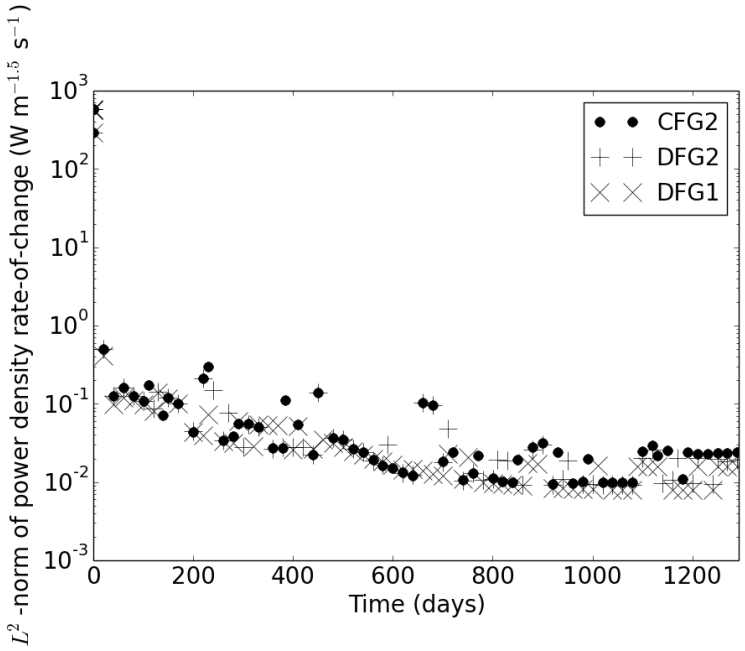

Figure 5.14: This is a comparison between coupled and decoupled fission gas cases of the L^2-norm of the power density rate-of-change for the WBN1 fuel pin model.

Table 5.8 shows the same value for plenum inventory and fission gas released for the decoupled cases because there is no distinction between these quantities with decoupled fission gas fields. Part of the fission gas coupling algorithm is to account for loss of fission gas in the plenum due to decay and transmutation. The loss of fission gas in the plenum is evident from the fact that the relative difference in the plenum inventory, 9.62%, is slightly smaller than the relative difference in gas released, 9.97%; as noted, these quantities are both percentages of the same value (i.e. the fission gas released to the plenum in DFG2). This shows that the effect of decay and transmutation in the plenum is small the WNB1 constant power case. Fig. 5.13 also shows that the difference between fission gas released and the plenum fission gas inventory is small. Temperature feedback (i.e. the difference between 2-way and 1-way coupled cases) causes a large decrease in the eigenvalue (435 pcm), as shown in Fig. 5.15.

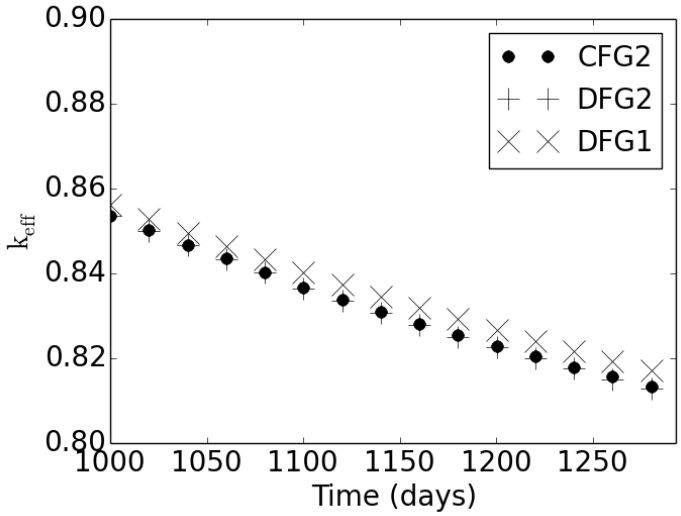

Figure 5.15: This is a comparison between coupled and decoupled fission gas cases of the neutron transport eigenvalue (for an infinite pin array) near the end of life for the WBN1 fuel pin model.

B.4 Fissionable Nuclide-Dependent Fission Gas Source in Sifgrs

As stated in the previous section, many of the discrepancies in QOIs between coupled and decoupled fission gas simulations might be decreased by increasing the fidelity of the Sifgrs fission gas source. This also has the potential to increase the accuracy of BISON. In this section, a prescription is made for a more accurate fission gas source in BISON's Sifgrs module. Improving the fission gas source in Sifgrs only requires a small patch to BISON.

As burnup increases in a fuel pin, a smaller fraction of fissions occur in ^{235}U, and a larger fraction occur in ^{238}U and the various fissionable plutonium nuclides. This is germane to fission gas release because each of these fissionable nuclides has a different yield of fission gas nuclides. In BISON, the `BurnupFunction` module calculates the spatial distributions of the concentrations of ^{235}U, ^{238}U, and ^{239}Pu-^{242}Pu using the Lassmann model [3]. Hence, by accessing these data in Sifgrs, a more accurate fission gas source can be calculated.

In order to create a new expression for the fission gas source in Sifgrs, the Bateman equations, Eqs. (2.3), must be considered for each fission gas nuclide. Several simplifications may be made to Eqs. (2.3) when they are used to describe the source of fission gas nuclide i. The migration of fission gas is not considered to be a part of the source, so it is ignored here. Beta decay is the only type of radioactive decay considered as the source of fission gas; in this section, the index of the parent of fission gas nuclide i is $i - p_i$. Six fissionable nuclides of uranium and plutonium are considered, so the index j runs from 1 to 6. These simplifications result in Eqs. (5.2).

$$\frac{\mathrm{d}N_i(t)}{\mathrm{d}t} = \lambda_{i-p_i} N_{i-p_i} + \bar{\phi}\sigma_{\mathrm{a},i-1} N_{i-1} + \bar{\phi} \sum_{j \in \mathrm{U,Pu}} y_{ij}\sigma_{\mathrm{f},j} N_j - (\lambda_i + \bar{\phi}\sigma_{\mathrm{a},i}) N_i \quad (i \in \text{FG nuclides}), \tag{5.2}$$

One deficiency of Eqs. (5.2) is that they do not account for resonance absorption in ^{238}U. The Lassmann model, which inspired the fissionable nuclide-dependent source, does account for the resonance absorption by including a prescribed radial shape function for the ^{238}U number density [3]. Neglecting the effect of resonance absorption will result in some error in the fissionable nuclide-dependent source for moderate to high burnup.

BISON's Sifgrs module does not differentiate between different fission gas nuclides, so Eqs. (5.2) are summed over i, which includes all N_{fg} fission gas nuclides. When this summation occurs, the terms $\bar{\phi}\sigma_{\mathrm{a},i-1}N_{i-1}$ and $\bar{\phi}\sigma_{\mathrm{a},i}N_i$ cancel out, leaving Eq. (5.3), which

is the net fission gas production rate.

$$\sum_{i\in \text{FG nuc}} \frac{\mathrm{d}N_i(t)}{\mathrm{d}t} = \frac{\mathrm{d}N(t)}{\mathrm{d}t} = \sum_{i\in \text{FG nuc}} \lambda_{i-p_i} N_{i-p_i} + \bar{\phi} \sum_{j\in \text{U \& Pu}} \sigma_{\mathrm{f},j} N_j \sum_{i\in \text{FG nuc}} y_{ij} - \sum_{i\in \text{FG nuc}} \lambda_i N_i \tag{5.3}$$

Another simplification is to assume that the fission gas precursors decay instantly to fission gas atoms, which is a reasonable assumption as long as the precursor half-life is small compared to the time step or the absorption cross section is reasonably large. With this assumption, fission gas precursor atoms born from fission are included in the fission source of their daughters; so, Eq. (5.3) becomes Eq. (5.4).

$$\frac{\mathrm{d}N(t)}{\mathrm{d}t} = \bar{\phi} \sum_{j\in \text{U,Pu}} \sigma_{\mathrm{f},j} N_j \sum_{i\in \text{FG nuc \& pre}} y_{ij} - \sum_{i\in \text{FG nuc}} \lambda_i N_i \tag{5.4}$$

y_{ij} may be summed over i to simplify Eq. (5.4).

$$y_j = \sum_{i\in \text{FG nuc \& pre}} y_{ij} \tag{5.5}$$

As stated earlier, BISON tracks six fissionable nuclides, so there are six y_j values. These data may be obtained from the MPACT depletion library [1]; the fision yields are summed for the following fission gas nuclides and their precursors: ^{79}Br,^{81}Br,^{80}Kr-^{88}Kr,^{128}I-^{135}I, and ^{128}Xe-^{137}Xe. The y_j values may be thought of as comprising a vector $\mathbf{y}$, as shown in Eq. (5.6); the fractional yield of fission gas from each fissionable nuclide is between 0.40 and 0.47.

$$\begin{aligned}\mathbf{y} &= [y_{235\text{U}} \quad y_{238\text{U}} \quad y_{239\text{Pu}} \quad y_{240\text{Pu}} \quad y_{241\text{Pu}} \quad y_{242\text{Pu}}] \\ &= [0.4643 \quad 0.4414 \quad 0.4455 \quad 0.4291 \quad 0.4212 \quad 0.4056]\end{aligned} \tag{5.6a}$$

Eq. (5.4) may be rewritten as Eq. (5.7), with y_j.

$$\frac{\mathrm{d}N(t)}{\mathrm{d}t} = \bar{\phi} \sum_{j\in \text{U,Pu}} y_j \sigma_{\mathrm{f},j} N_j - \sum_{i\in \text{FG nuc}} \lambda_i N_i \tag{5.7}$$

In the Sifgrs module, the neutron flux is not available, so the one-group neutron flux in Eq. (5.7) is replaced. This is done by expressing the one-group flux in terms of fission rate density $\dot{F}$, as shown in Eq. (5.8).

$$\bar{\phi} = \frac{\dot{F}}{\sum\limits_{j\in \text{U,Pu}} \sigma_{\text{f},j} N_j} \tag{5.8}$$

Inserting Eq. (5.8) into Eq. (5.7) yields Eq. (5.9).

$$\frac{\mathrm{d}N(t)}{\mathrm{d}t} = \dot{F} \frac{\sum\limits_{j\in \text{U,Pu}} y_j \sigma_{\text{f},j} N_j}{\sum\limits_{j\in \text{U,Pu}} \sigma_{\text{f},j} N_j} - \sum_{i\in \text{FG nuc}} \lambda_i N_i \tag{5.9}$$

The final alteration to the fission gas source equation is to simplify the radioactive decay term. To do so, an averaged decay coefficient is defined for all fission gas nuclides, as shown in Eq. (5.10).

$$\bar{\lambda} = \frac{\sum\limits_{i\in \text{FG nuc}} \lambda_i N_i}{\sum\limits_{i\in \text{FG nuc}} N_i} \tag{5.10}$$

Inserting Eq. (5.10) into Eq. (5.9) yields Eq. (5.11). This is the fissionable nuclide-dependent source that was implemented in BISON's Sifgrs with a code patch.

$$\frac{\mathrm{d}N(t)}{\mathrm{d}t} = \dot{F} \frac{\sum\limits_{j\in \text{U,Pu}} y_j \sigma_{\text{f},j} N_j}{\sum\limits_{j\in \text{U,Pu}} \sigma_{\text{f},j} N_j} - \bar{\lambda} \sum_{i\in \text{FG nuc}} N_i \tag{5.11}$$

Because of its dependence on the fission gas nuclide concentrations, $\bar{\lambda}$ is space- and time-dependent, but for the implementation in Sifgrs, it will be a constant for the sake of simplicity. Selecting a value is difficult, and in general it depends on the fuel model. For the WBN1 single-pin simulation, a spatially-averaged, time-dependent value of $\bar{\lambda}$ may be calculated from simulation output data. In order to do this, two simulations are performed:

1. BISON with a fissionable nuclide-dependent source, using the $\mathbf{f}$ vector from Eq. (5.6), and the one-group cross section data already contained in BISON's `BurnupFunction` module, with $\bar{\lambda}$ set to zero

2. A CFG2 Redwing simulation with a fixed κ value of $3.2 \cdot 10^{-11}$ J/fission, similar to the one described in Section B.3

For these simulations and the rest discussed in this section, the pin linear power density was reduced to 18303 W/m, which is the average value for a pin in WBN1. This was done to prevent cladding lift-off until higher burnups were achieved. The simulations were run for six years. Also, all simulations were run with the fast flux calculated by summing flux

in the four highest-energy groups, so that the minimum fast flux energy was 1.35 MeV. The time-dependent value of $\bar{\lambda}$ was calculated by plugging in the appropriate output data from these two simulations into Eq. (5.11), and then solving for $\bar{\lambda}$. The resulting value depends strongly on time, as shown in Fig. 5.16.

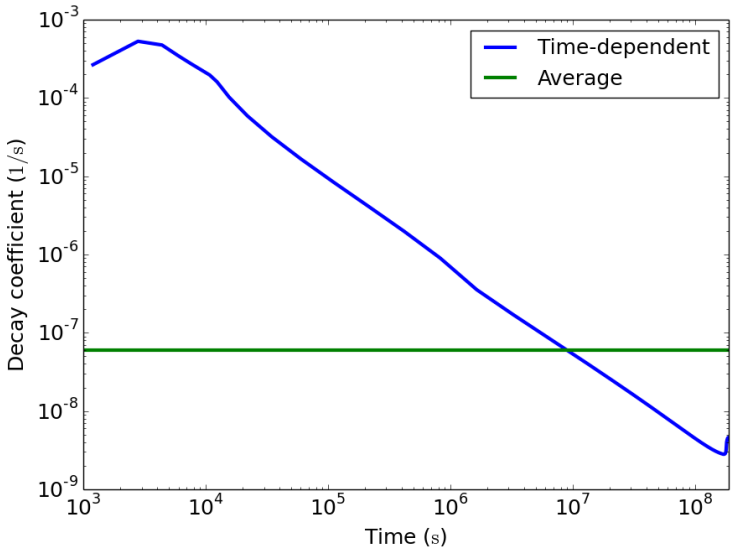

Figure 5.16: This is the decay coefficient ($\bar{\lambda}$) in Eq. (5.11) calculated from the output of Redwing and BISON simulations of a WBN1 single-pin model. The time-dependent value as well as its average are shown.

There is not a systematic method for determining a single value of the decay coefficient. The average value of the decay coefficient was used in a BISON simulation with a fissionable nuclide-dependent source, and the amount of fission gas reached a false equilibrium because the loss rate to decay and transmutation became too high. Therefore, several lower values of the decay coefficient were chosen to predict a more physically accurate fission gas source.

In order to make the BISON fission gas source match Redwing, simulations with several different constant values of the decay coefficient (i.e. decay constants) were run with the fissionable nuclide-dependent source; the output of simulations with decay constants of $1.5 \cdot 10^{-9}\text{s}^{-1}$ and $4.2 \cdot 10^{-9}\text{s}^{-1}$ are discussed here. Beside the fissionable nuclide-dependent source, a simpler change was made to the BISON fission gas source. Rather than using the standard Sifgrs source of $0.3017\dot{F}$, an adjusted source of $0.3070\dot{F}$ was used; with the adjusted source, the net fission gas generated is nearly the same as Redwing after six years

of burnup. The Redwing simulation with a fixed κ is included in the following table and figures in order to evaluate the BISON simulations.

Fig. 5.17 shows the net fission gas generated for these cases. The cases with a fissionable nuclide-dependent source have a curved profile, while the other cases have a nearly linear profile. The high rate of fission gas production in the beginning of the fissionable nuclide-dependent simulations suggests that the summed fission yields for fission gas, $\mathbf{y}$, are overestimated. The right-hand subplot in Fig. 5.17 shows more detail; from this it can be seen that the case which best matches Redwing fixed-κ at the end of the simulation is BISON with the adjusted source. Also, according to results from Redwing, when κ is fixed, the net fission gas production rate rises slowly over burnup, rather than decreasing, which suggests that the fission gas source modeled with Eq. (5.11) should actually have a negative value of $\bar{\lambda}$.

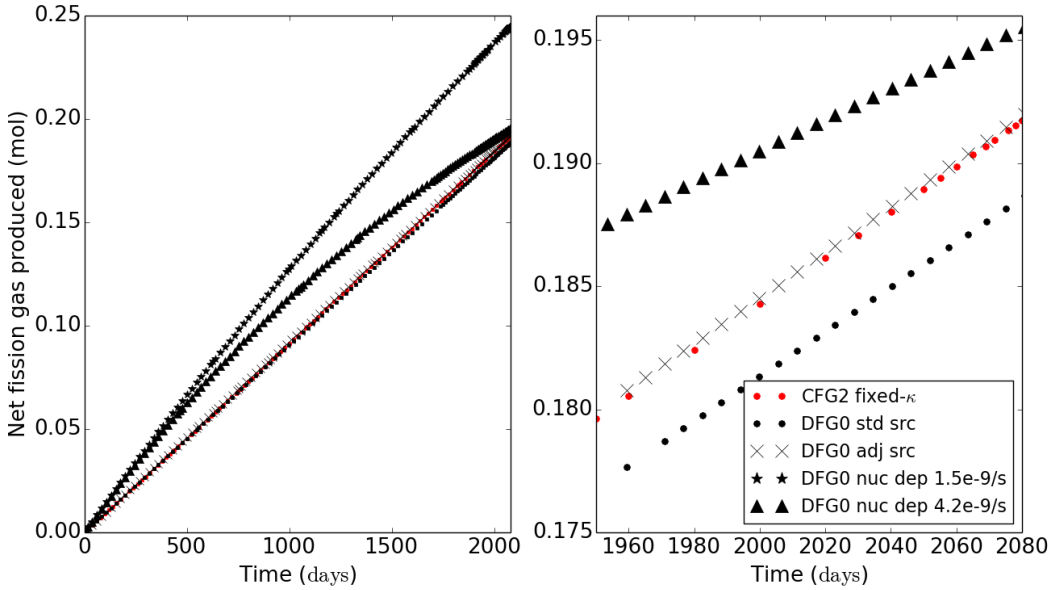

Figure 5.17: This is the net fission gas generated for several cases of the WBN1 simulation with constant power. "BISON nuc dep" refers to BISON simulations with a fissionable nuclide-dependent source, listed along with the decay constant. "BISON adj source" is a BISON simulation with a simple fission gas source of 0.3070 $\dot{F}$. "BISON std source" is a BISON simulation with the standard fission gas source of 0.3017 $\dot{F}$.

By the end of the simulations, the net fission gas source in the Redwing fixed-κ simulation is best matched by BISON with an adjusted soure or the fissionable nuclide-dependent source with a decay constant of $4.2 \cdot 10^{-9} \mathrm{s}^{-1}$. However, the fission gas released is best matched by BISON with a decay constant of $1.5 \cdot 10^{-9} \mathrm{s}^{-1}$, which can be seen in Fig. 5.18.

The reason for this is clear from Fig. 5.19: Redwing undergoes slower gap closure at the beginning of the simulation, leading to higher average fuel temperatures and more diffusion of fission gas, priming the fuel for higher rates of fission gas release near the end of the simulation. This behavior was also noted in results in Chapter 4. Because gap closure is the result of a sensitive thermomechanics problem, small differences between Redwing and BISON in initial radial power profile may lead to a fairly significant gap closure discrepancy.

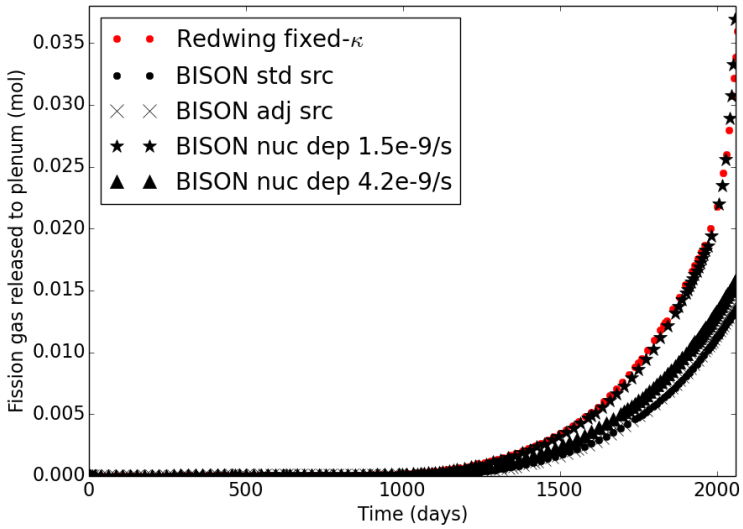

Figure 5.18: This is the fission gas released to the plenum for several cases of the WBN1 simulation with constant power.

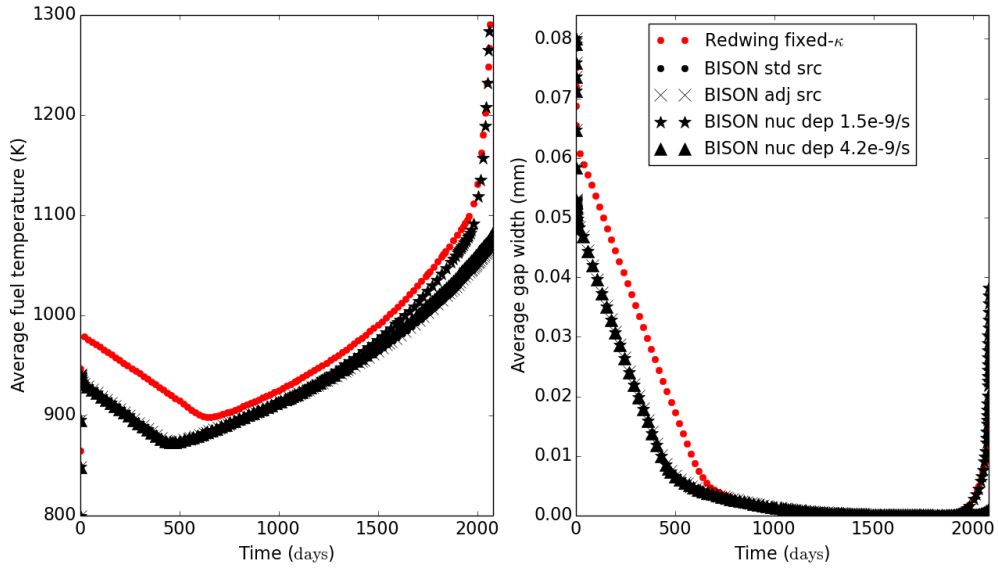

Figure 5.19: This is a comparison of the average fuel temperature and the average gap width for several cases of the WBN1 simulation with constant power. On the right-hand side of the plots, the Redwing and $1.5 \cdot 10^{-9}\text{s}^{-1}$ decay constant cses show the beginning of cladding lift-off.

Tables 5.9 and 5.10 show comparisons of the various BISON simulations to the Redwing fixed-κ simulation at 4.3 and 5.5 years of burnup. For the simulations discussed in this section, which are set at the average WBN1 pin power, 4.3 years of burnup corresponds to 59 MWD/kgHM, and 5.5 years of burnup corresponds to 77 MWD/kgHM, which is quite high. These tables show that the adjusted source has improved the accuracy of the BISON fission gas source (i.e. net fission gas produced) for both burnups shown; this is evident from the fact that the Redwing fixed-κ and adjusted source simulations have very similar percent differences. The BISON simulation with a fissionable nuclide-dependent source and decay constant of $4.2 \cdot 10^{-9}\text{s}^{-1}$ improved the fission gas source, but only near the end of the simulation. Table 5.10 shows that the BISON simulation with a fissionable nuclide-dependent source and decay constant of $1.5 \cdot 10^{-9}\text{s}^{-1}$ matches the Redwing fixed-κ of fission gas released and average fuel temperature fairly well. While these results show that implementing a fissionable nuclide-dependent source in BISON can improve its prediction of QOIs, the changes in the code may just be compensating for the gap closure discrepancy between Redwing and BISON (see Fig. 5.19), rather than improving the accuracy of the fission gas source. The discrepancy obfuscates the comparison of Redwing and BISON with novel fission gas source prescriptions. The cause of the discrepancy should be determined so that it may be reduced or eliminated. That way, direct comparisons between BISON and Redwing can be made to evaulate changes to BISON.

It was posited in Section B.3 that the discrepancies between decoupled and coupled fission gas cases were partly due to the change in the Sifgrs fission gas source. In this section, the Sifgrs fission gas source was also changed, and its effect on QOIs can be compared to the effect in the previous section using data in Table 5.9 and Table 5.8; these data were taken at the same burnup (59 MWD/kgHM). The adjusted Sifgrs fission gas source of 0.3070 $\dot{F}$ provides a change of 1.76% in the net fission gas produced, similar to the increase of 1.92% caused by coupling fission gas in Redwing (i.e. CFG2 vs. DFG2); however, the adjusted Sifgrs source resulted in only about a 3% increase in fission gas released, which coupling fission gas in Redwing resulted in an almost 10% increase in this QOI. The two BISON simulations with a fission nuclide-dependent source cause changes in average fuel temperature that are comparable to the change caused by coupling fission gas in Redwing: an approximate 1% increase. These results indicate that changing the fission gas source has a significant effect on QOIs, and it may be the most important part of fission gas coupling; however, the effects of implementing novel fission gas source prescriptions in Sifgrs on BISON were not the same as implementing fission gas coupling in Redwing. It would be better to make these comparisons of data from WBN1 simulations run at the same power.

Table 5.9: Relative differences in quantities of interest of WBN1 simulations at 4.3 years of burnup compared to BISON with a standard fission gas source of 0.3017 $\dot{F}$; the abbreviations for the other simulations are: "RW fix-κ" for the Redwing with fixed κ, "adj src" for BISON with an adjusted source of 0.3070 $\dot{F}$, and "FNDS" for BISON with a fissionable nuclide-dependent source with two decay constants.

Output quantity	std src	RW fix-κ	adj src	FNDS 1.5e-9/s	FNDS 4.2e-9/s
Average fuel temperature	975 K	2.92%	0.05%	1.34%	0.60%
Maximum fuel temperature	1347 K	4.53%	0.06%	1.00%	0.45%
Net fission gas produced	0.143 mol	1.33%	1.76%	34.78%	13.32%
Plenum fission gas inventory	0.00241 mol	97.45%	2.97%	86.96%	37.69%
Fission gas released to plenum	0.00241 mol	98.12%	2.97%	86.96%	37.69%
Fractional fission gas released	1.68%	95.57%	1.21%	38.73%	21.51%

Table 5.10: Relative differences in quantities of interest of WBN1 simulations at 5.5 years of burnup compared to BISON with a standard fission gas source of 0.3017 $\dot{F}$

Output quantity	std src	RW fix-κ	adj src	FNDS 1.5e-9/s	FNDS 4.2e-9/s
Average fuel temperature	1053 K	8.61%	0.20%	6.52%	1.00%
Maximum fuel temperature	1489 K	9.89%	0.16%	5.40%	0.78%
Net fission gas produced	0.182 mol	1.62%	1.76%	30.48%	4.92%
Plenum fission gas inventory	0.0116 mol	99.05%	3.86%	94.64%	19.34%
Fission gas released to plenum	0.0116 mol	99.46%	3.86%	94.64%	19.34%
Fractional fission gas released	6.34%	96.23%	2.07%	49.17%	13.75%

C Transient Fission Gas Release Triggered by a Reactor Shutdown

The single fuel pin model was run with a shutdown that occurs just after 900 days and lasts for 3.5 days. The shutdown period is based on plant data from a Watts Bar shutdown. The preceding 900 days may be thought of as two fuel cycles. Fig. 5.20 shows the power history for the shutdown cases.

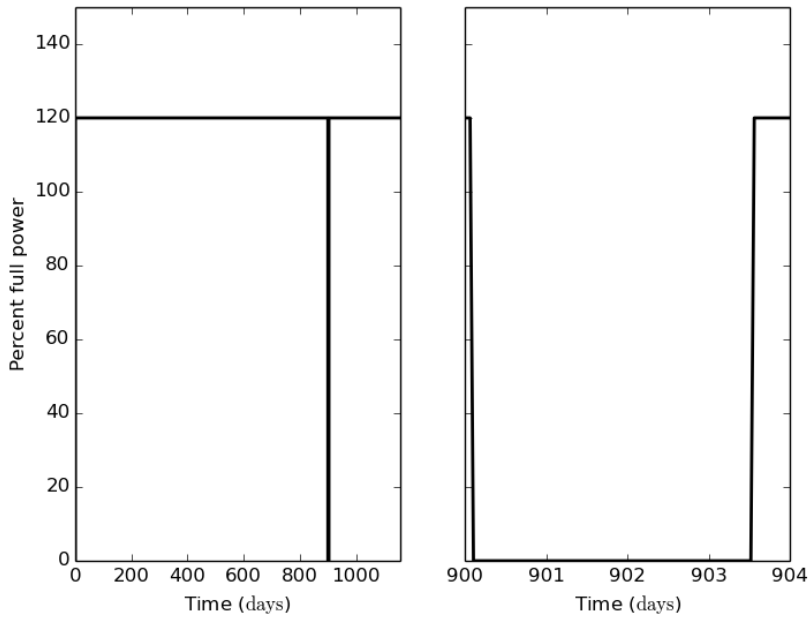

Figure 5.20: This is the power history for the shutdown cases. The power percentage is relative to the average pin power in WBN1.

Adding a shutdown to the WBN1 pin model makes the fuel/cladding contact problem more difficult to solve. This occurs because thermal contraction and expansion of the fuel and cladding cause quick changes in the relative position of these parts of the pin during shutdown and startup; therefore, two changes were made to the contact model in order to make it easier to solve: first, the formulation was changed from kinematic to penalty. Second, the penalty parameter was reduced from 10^{14} to 10^{9}; this makes the contact problem easier to solve at the expense of lower accuracy.

C.1 Sensitivity Study of the Redwing Time Step

First, a time step sensitivity study was performed for the shutdown period; Varying the time step during the shutdown had almost no effect on the QOIs. A separate time step sensitivity study was performed for the period immediately after the shutdown, with the time step during shutdown set to 0.25 days. Table 5.11 shows the wall time taken for each simulation in this sensitivity study. Increasing the post-shutdown time step size reduces the wall time somewhat.

Table 5.11: Wall times for post-shutdown time step sensitivity study using one Fission node

Case (dt in days)	Wall time (hr)
1.25	18.2
2.5	17.2
5	16.4
10	15.7
20	15.6

Table 5.12 shows the effects of varying the time step in the 60-day period after the shutdown. Varying the time step throughout this period had a significant effect on the QOIs. Most QOIs do not show a monotonic change in the relative error with respect to the most refined case (dt = 1.25 days), with the exception of k_{eff}, which shows a monotonic decrease with first-order convergence. Fig. 5.21 shows the effect of varying the post-shutdown time step on the percent fission gas released; all simulations agree fairly well, except for the period from about t = 900 to 1000 days, when transient fission gas release was occuring.

Table 5.12: Relative differences in quantities of interest and absolute difference in k_{eff} for post-shutdown time step sensitivity study at t = 1103.5 days.

Output quantity	Finest: dt = 1.25	dt = 20	dt = 10	dt = 5	dt = 2.5
Average fuel temperature	1087 K	0.03%	-0.13%	0.05%	0.10%
Maximum fuel temperature	1531 K	0.23%	0.02%	0.09%	0.09%
Minimum cladding hoop strain	-0.01415	-0.47%	0.65%	-0.68%	-0.86%
Fractional fission gas released	6.555%	0.51%	-2.47%	0.95%	1.93%
Net fission gas produced	0.1156 mol	0.01%	0.01%	0.07%	0.07%
Plenum fission gas inventory	0.00755 mol	0.50%	-2.49%	1.01%	2.00%
Fission gas released to plenum	0.00757 mol	0.52%	-2.46%	1.01%	2.00%
Fuel fission gas inventory	0.1080 mol	-0.03%	0.19%	0.00%	-0.07%
k_{eff}	0.836554	-25 pcm	-12 pcm	-6 pcm	-3 pcm

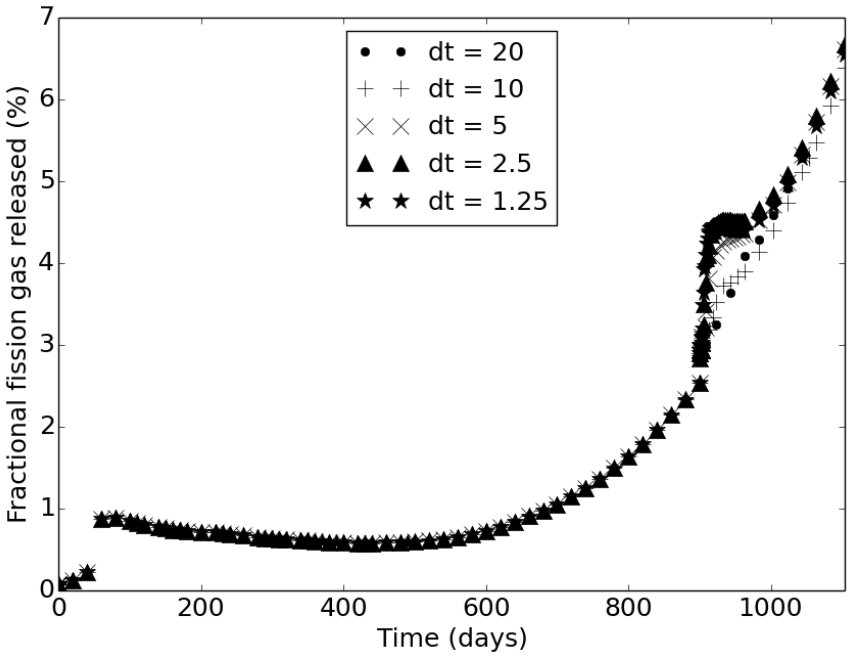

Figure 5.21: The fractional fission gas released as a percentage of net fission gas production for the single-pin shutdown case. The legend shows the Redwing time step, which was varied for the period from t = 903.5 days (i.e. immediately after the shutdown) to 960 days.

One reason for the lack of monotonic convergence with dt is the error in the net fission gas produced; when the time step is decreased from 10 to 5 days, the error in this QOI increases from 0.01% to 0.07%. While this error is insignificant, small changes in the net fission gas produced can lead to larger changes in the fission gas released. Another interesting result of this study is the change in error in percent fission gas released from 0.51% to -2.47% when dt is decreased from 20 to 10 days. It is not clear what causes this increase in the error magnitude. Due to the fact that the QOIs do not show a discernable error convergence behavior and that the QOI errors do not exceed 3%, the 20-day time step case was selected for further study.

C.2 Stability of Simulations with Shutdown

The addition of a shutdown into the WBN1 single-pin model caused stability issues due to the change in power. Even with prescribed TH, the axial power distribution shows unphysical fluctuations after the shutdown. Although the instabilities were dampened by the model (rather than growing unbounded), they still reduce confidence in the simulation results. The fluctuations can be quantified by taking the L^2-norm (over the BISON mesh) of the power density rate of change in the fuel. The expected behavior for this QOI is to

change slowly over time, reflecting the change in intra-pin power distribution as the fuel composition changes, with sharp changes only at the time of shutdown and restart; however, the L^2-norm remains elevated after the shutdown. The power density fluctuations are especially bad for cases that ^{135}Xe was treated like all other nuclides by MPACT's Bateman solver (i.e. transient Xe), rather than set to its equilibrium value (i.e. equilibrium Xe). Figs. 5.22 and 5.23 show the behavior of the L^2-norm of the rate of change of the power density; transient Xe treatment shows a much higher L^2-norm due to the power density distribution fluctuating. The greater instability in the transient Xe cases can also be seen by comparing the maximum temperature, which fluctuated much more in the transient Xe case; see Figs. 5.24 and 5.25.

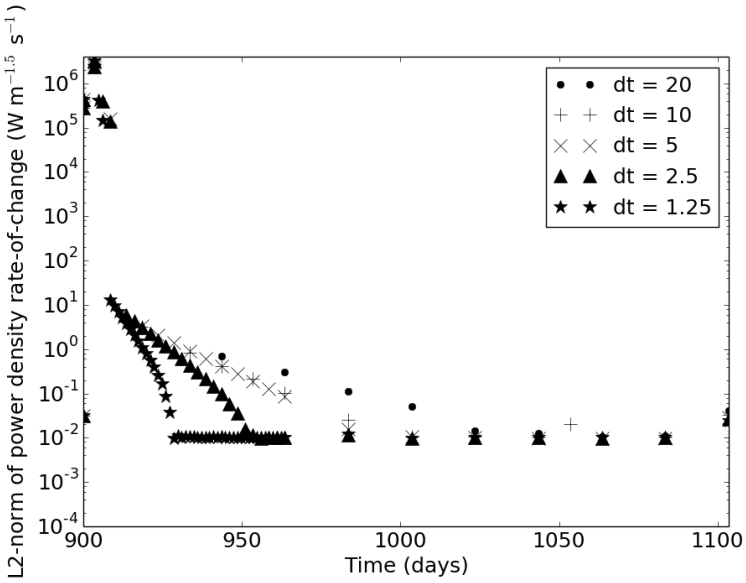

Figure 5.22: The L^2-norm (over the BISON mesh) of the rate of change of the power density for the single-pin shutdown case with equilibrium Xe treatment. The legend shows the Redwing time step immediately after the shutdown.

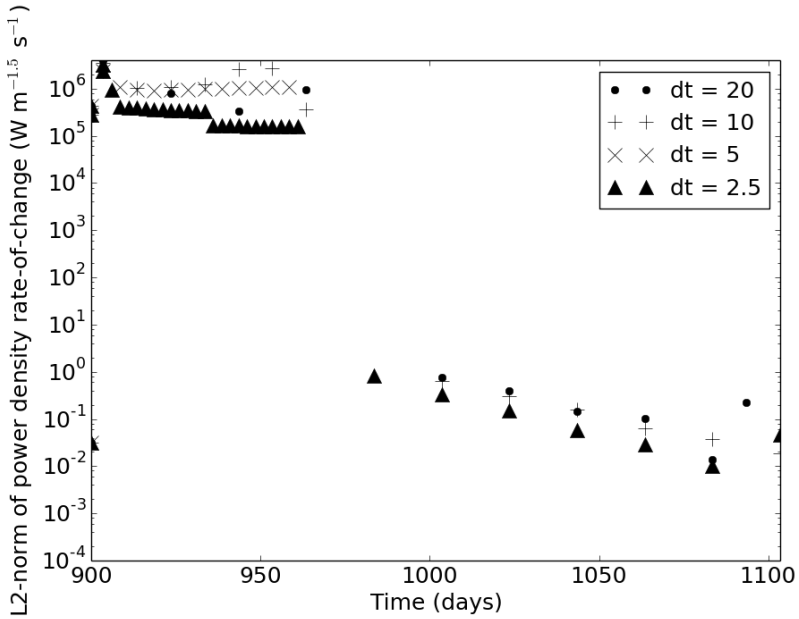

Figure 5.23: The L^2-norm (over the BISON mesh) of the power density rate of change for the single-pin shutdown case with transient Xe treatment. The legend shows the Redwing time step immediately after the shutdown.

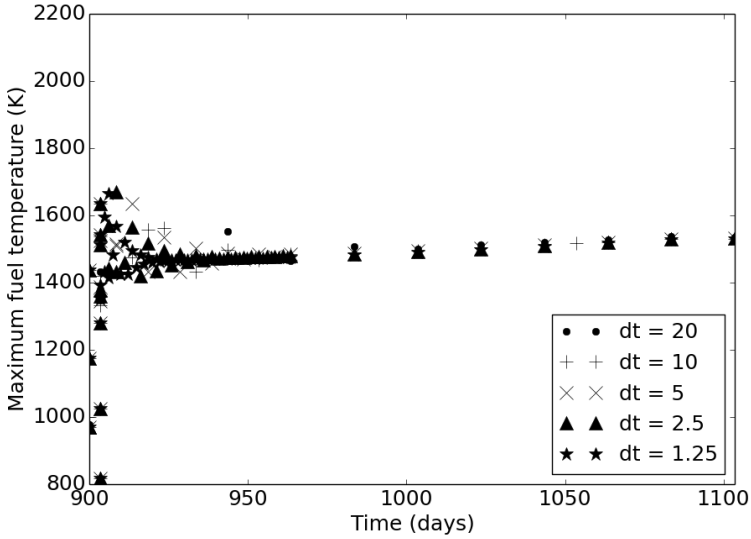

Figure 5.24: The maximum temperature evolution for the single-pin shutdown case with equilibrium Xe treatment. The legend shows the Redwing time step immediately after the shutdown.

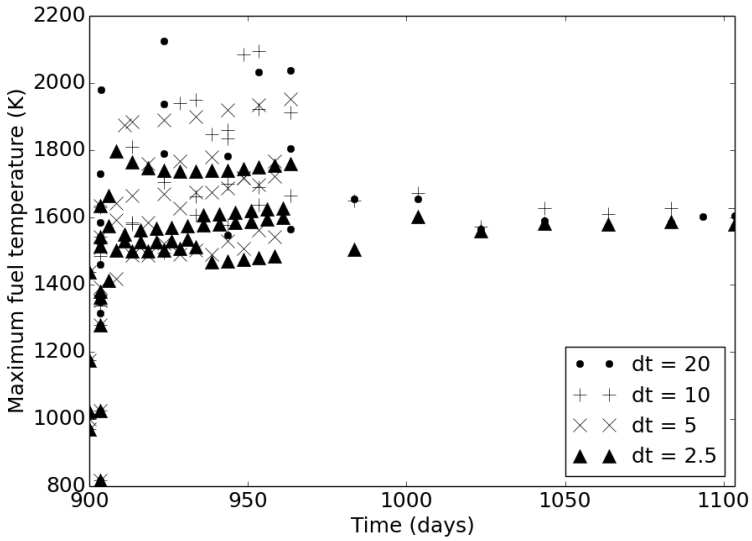

Figure 5.25: The maximum temperature evolution for the single-pin shutdown case with transient Xe treatment. The legend shows the Redwing time step immediately after the shutdown.

A comparison of the equilibrium Xe cases in Fig. 5.22 shows some intersting results. After the shutdown, the L^2-norm of the power density rate of change eventually reaches a steady level at about 10^{-2} W m$^{-1.5}$ s^{-1}, which represents the change in the power density distribution due to nuclide evolution. By comparing the dt = 1.25, 2.5, and 5 days cases, the L^2-norm takes about 15 time steps for the fluctuations to damp out, regardless of the time step size. Hence, decreasing the time step size does not decrease the severity of the fluctuations in power density, but it does decrease the amount of time needed to totally dampen them.

The fluctuations in power density result in higher local power density, which in turn results in higher fuel temperatures; see Figs. 5.24 and 5.25. This results in significantly higher, and unphysical, fission gas release rates; Fig. 5.26 demonstrates this. Further steps must be taken in order to increase the stability of the Redwing simulations with shutdown in order to obtain physically realistic results.

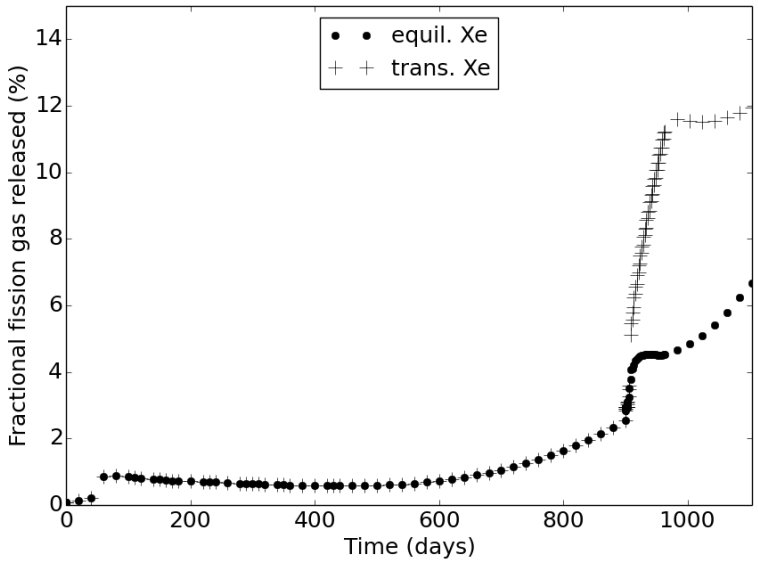

Figure 5.26: This is a comparison of the percent fission gas released between equilibrium and transient Xe treatments.

C.3 Effect of Fission Gas Coupling

Like Subsection B.3, a comparison of cases was performed to evaluate the effects of fission gas coupling. A single 3.5 day Redwing time step was prescribed for the shutdown period for the three cases, and 20 day time steps with equilibrium xenon treatment were used after the return to full power. Table 5.13 shows differences in QOIs at the end of the simulation. There are several significant differences in the QOIs; most notably the fissiong gas released, the fission gas plenum inventory, and k_{eff}. Unfortunately, the results suggest that the greater degree of instability in the two-way coupled simulations is the main cause of these differences, rather than an increase in physical accuracy of the simulations.

Table 5.13: Relative differences in quantities of interest and absolute difference in k_{eff} caused by fission gas coupling at t = 1103.5 days.

Output quantity	Reference: DFG1	CFG2	DFG2
Average fuel temperature	1074 K	1.19%	0.98%
Maximum fuel temperature	1514 K	1.33%	0.89%
Minimum cladding hoop strain	-0.01493	-5.70%	-4.24%
Fractional fission gas released	5.540%	18.91%	15.78%
Net fission gas produced	0.1136 mol	1.76%	0.02%
Plenum fission gas inventory	0.00629 mol	20.62%	15.80%
Fission gas released to plenum	0.00629 mol	21.00%	15.80%
Fuel fission gas inventory	0.1073 mol	0.63%	-0.91%
k_{eff}	0.840210	-391 pcm	-422 pcm

The L^2-norm of the power density rate-of-change in the fuel gives an indication of the severity of the instability in the simulation, as shown in Fig. 5.27. The instability is evident after the shutdown at 900 days, where the two-way cases show an L^2-norm that is dampened over the period of about five time steps. The greater instability leads to more peaked power density profiles, which lead to unphysically high amounts of fission gas release; this is shown by Fig. 5.28. The change in fission gas released caused fission gas coupling is about 20%; some of this is likely due to errors caused by the instability, rather than improvements in the physical models due to fission gas coupling. Based on these results, implementing tight coupling is more important for fuel pin simulations with a shutdown than simulations at constant power.

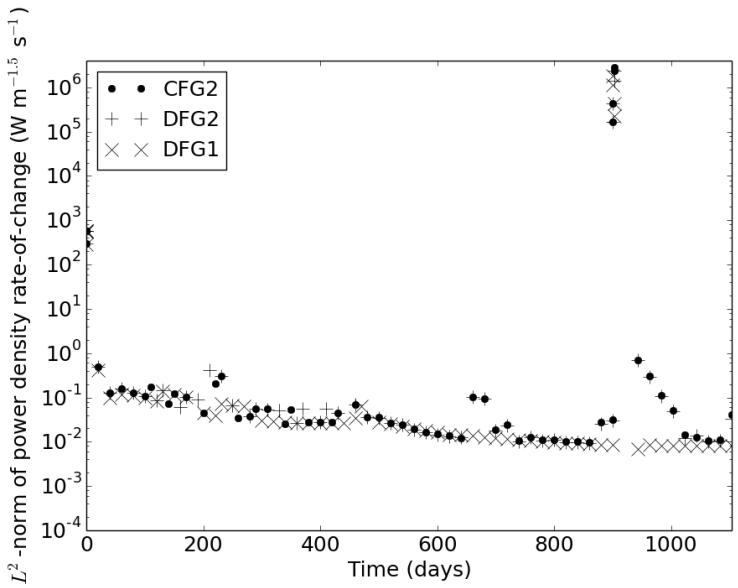

Figure 5.27: The L^2-norm (over the BISON mesh) of the power density rate of change for the single-pin shutdown case. The legend shows the coupling methods for each case: one-way (MPACT to BISON), two-way with decoupled fission gas, and two-way with coupled fission gas.

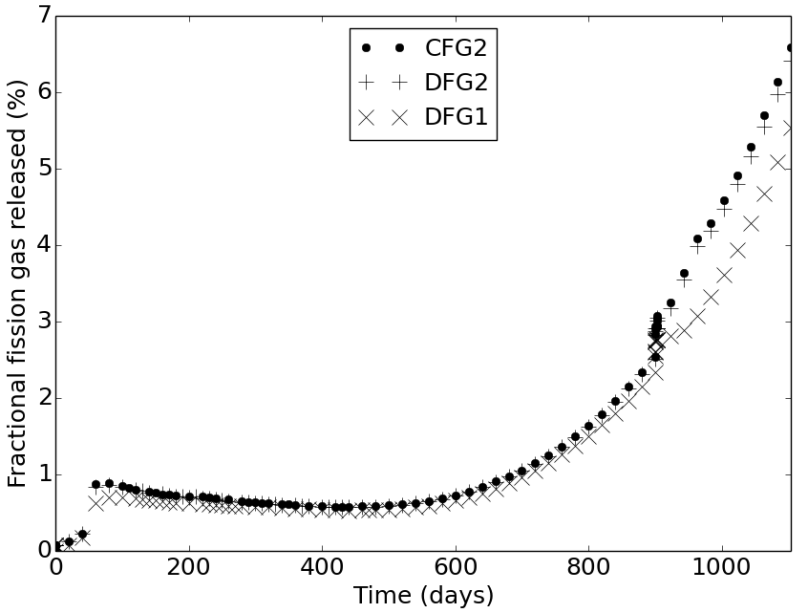

Figure 5.28: The fractional fission gas released as a percentage of net fission gas production for the single-pin shutdown case. The legend shows the coupling methods for each case: one-way (MPACT to BISON), two-way with decoupled fission gas, and two-way with coupled fission gas.

The difference in average fuel temperature among all coupling cases stays within 5K before the shutdown, so k_{eff} and the fission gas released results agree quite well over this time period. After shutdown, the CFG2 and DFG2 cases underwent greater fission gas release, which led to higher fuel temperatures; see Fig. 5.29. A positive feedback effect occurs between fuel temperature and fission gas release, exascerbating this effect; note that fission gas release can affect gap conductivity even after the gap is closed, because BISON's thermal contact model enforces a minimum gap distance. As a result, the discrepancy in average fuel temperature ends up being 11K-13K, which is a small but consequential value. With a higher-power case, the discrepancy caused by higher fission gas release would be even greater. This temperature discrepancy contributes to the large difference in k_{eff} at the end of the simulation: see Fig. 5.30.

The case with coupled fission gas has a slightly higher average temperature than the two way coupling case with decoupled fission gas as well as a k_{eff} value which is slightly higher. As mentioned above, the fission gas released is overestimated due to the instability in the cases with two-way coupling. Hence, k_{eff} is overestimated because increased fission gas released results in less absorption of neutrons by ^{135}Xe in the fuel. These results provide another reason to use a new coupling method to stabilize Redwing simulations with fission gas coupling.

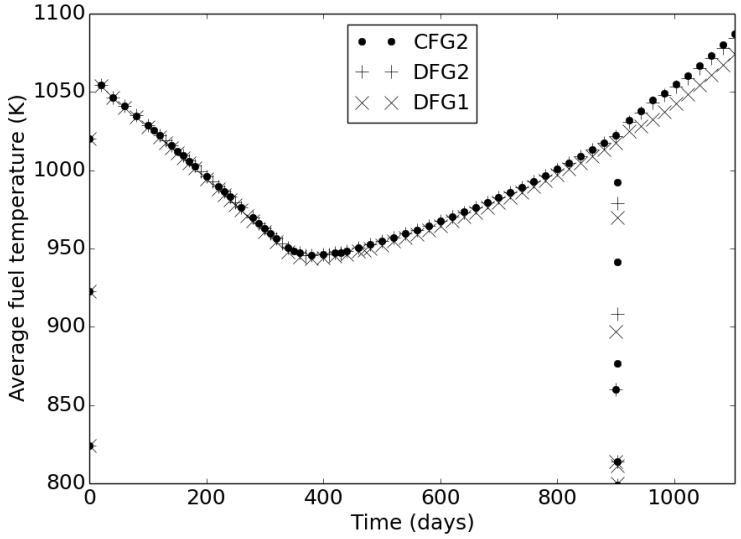

Figure 5.29: The average fuel temperature for the single-pin shutdown cases. The legend shows the coupling methods for each case: one-way (MPACT to BISON), two-way with decoupled fission gas, and two-way with coupled fission gas.

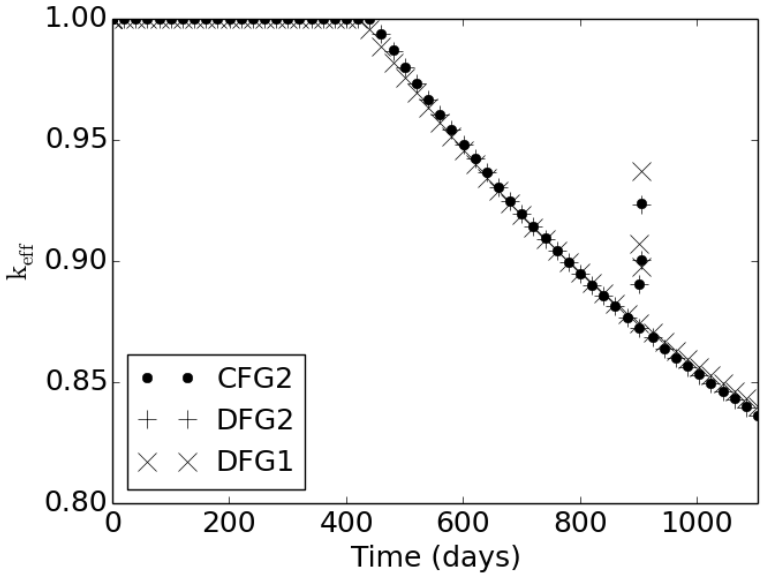

Figure 5.30: The neutron transport eigenvalue for the single-pin shutdown cases. The legend shows the coupling methods for each case: one-way (MPACT to BISON), two-way with decoupled fission gas, and two-way with coupled fission gas.

C.4 Effect of Thermal Hydraulics Coupling

The shutdown case results show that using Redwing's prescribed TH capability had a marginal effect on the stability of the simulations. Fig. 5.31 shows that the L^2-norm of the power density rate-of-change is consistently higher for coupled TH compared to prescribed TH; at many times in the simulation, it is twice as high, and even worse at some points. The only time at which the L^2-norm of prescribed TH is higher is at the very end of the simulation time. Although using Redwing's prescribed TH mode helped with the results of the simulation,

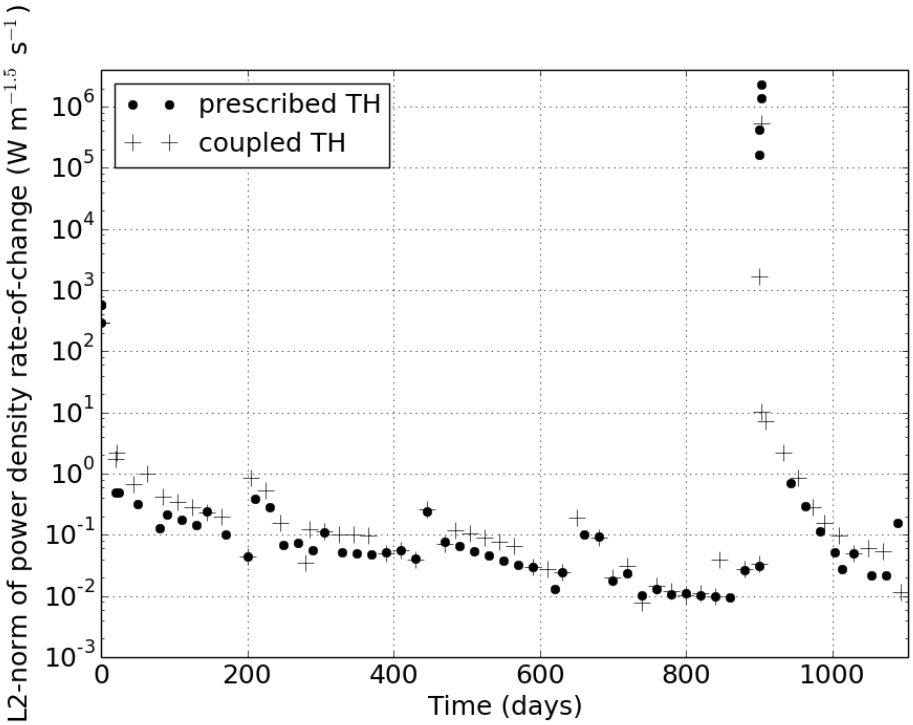

Figure 5.31: The L^2-norm (over the BISON mesh) of the power density rate of change for the single-pin shutdown case. Both cases had two-way coupling with fission gas coupled; one had prescribed TH and one had coupled TH.

CHAPTER 6

Fission Gas Coupling Results: Pin Array

In order to investigate the effects of fission gas coupling on the neutronic interaction between fuel pins, a small fuel pin array model with reflective side boundary conditions was created. Like the single pin model, the neutron transport boundary conditions on the top and bottom of the domain were vacuum. Figure 6.1 depicts the pin array model. A guide tube filled with water was placed in the upper left corner to create a tilt in the pin power distribution. All other pins contained fuel. The model could be thought of as a quarter of a 5x5 pin array with a central guide tube. A shutdown of 3.5 days occured at t = 900 days, which is roughly the length of two fuel cycles. The end of this simulation was at t = 1160 days.

Eight fuel pins were explicitly modeled with MPACT and BISON meshes; five fuel pins had unique solutions due to symmetry. Like with the single pin simulations, the MPACT mesh was 3D, while the BISON fuel pin meshes were 2D, extending in the axial and radial directions. Fields transferred from MPACT to BISON were first averaged over the azimuthal angle. Based on the single pin mesh sensitivity studies, the 16/27 radial meshing was used for each fuel pin and the maximum time step was set to dt = 20 days. In order to prevent problems with convergence of the thermomechanics problem, it was necessary to change the contact model; the penalty formulation was used instead of the kinematic formulation, and the penalty parameter was decreased from 10^{14} to 10^{9}.

Two simulations were run; one with coupled fission gas and one with decoupled fission gas. The fuel pin array simulation was run on Fission, using five nodes with ten processors per node. Table 6.1 shows the wall time required to run each simulation.

Table 6.1: Wall times for pin array simulations using five Fission nodes

Case	Wall time (hr)
Coupled fission gas	59.6
Decoupled fission gas	50.6

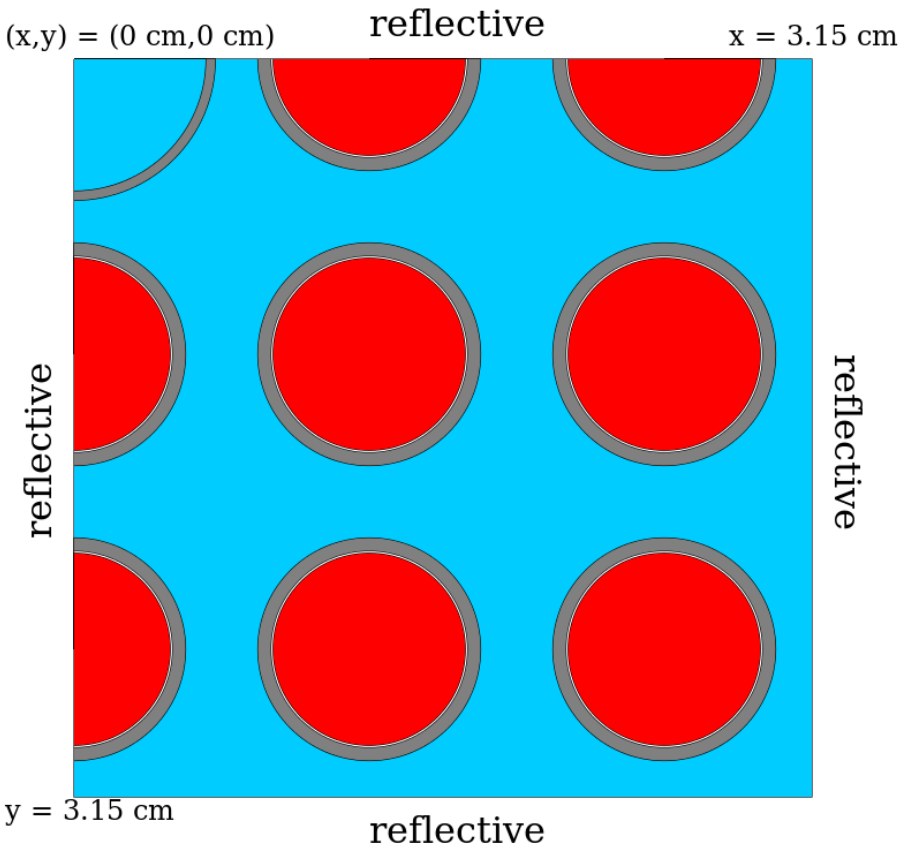

Figure 6.1: A cutaway view of the midplane of the pin array model. Red is fuel, blue is moderator, gray is Zircaloy, and white is helium in the fuel/cladding gap. Reflective boundary conditions for neutron transport were set on all four sides of the domain.

The power of the pin array was set such that the array's average pin power was 110% of the average pin power of WBN1 during normal operation; a 120% power simulation was attempted, but this resulted in convergence issues with the BISON solver. The hottest fuel pins were the two directly adjacent to the empty guide tube, and the coldest pin was the one farthest from the guide tube. At the end of the simulation, the hottest and coldest fuel pins were at 112% and 109% of the average pin power for WBN1, respectively. For WBN1 The difference in the hottest pin's power caused by coupling the fission gas fields was only 1 W, an insignificant amount.

Table 6.2 shows the differences in the hottest pin's QOIs caused by enabling fission gas coupling. Small yet significant differences can be seen in the fission gas QOIs; however, these differences are much smaller than those seen in the QOIs for the single pin problem (see Table 5.13). This suggests that the importance of fission gas coupling is mainly de-

pendent on the pin power, rather than other factors such as intrapin neutronic interactions or rapid power level changes.

Table 6.2: Relative differences in quantities of interest and absolute difference in k_{eff} for the hottest pin in the array caused by fission gas coupling

Output quantity	DFG2	CFG2
Avg. fuel temperature	1020 K	0.05%
Max. fuel temperature	1424 K	0.19%
Max. cladding hoop strain	0.00001	-0.48%
Fractional FG released	2.98%	0.86%
Net FG produced	0.113 mol	1.72%
Plenum FG inventory	0.00336 mol	1.93%
FG released to plenum	0.00336 mol	2.60%
Pin Power	75302 W	0.00%
k_{eff}	0.838002	11 pcm

Figure 6.2 shows k_{eff} over the simulation period. k_{eff} started at 1.00000 and remained fixed until the boron search yieled zero, and then the MPACT solver switched to solving the eigenvalue problem, so k_{eff} began to decrease. There was a brief spike in k_{eff} caused by the decrease in fuel and moderator temperature during the shutdown. This plot demonstrates that enabling fission gas coupling has a negligible effect on k_{eff} for this model.

Figure 6.3 shows the variation in pin power in the hottest and coldest fuel pins in the pin array. The shutdown is visible at t = 900 days, with two data points at about half the full power; these are the average power during one-hour ramps that bookend the 3.5 day shutdown. Figure 6.3 shows a very slight variation in the pin powers over the simulation time; the inter-pin power distribution was nearly fixed. The pin power difference was fairly steady and small at about 3000 W, but this was enough to cause a significant difference in the fission gas plenum inventory, as shown in Figure 6.4. At the end of the simulation, the hottest pin has 55% more fission gas in its plenum than the coldest pin; this shows that even small variations in pin power over a couple fuel cycles can have a significant effect on the plenum fission gas inventory. Also, Figure 6.4 shows a small burst in fission gas release during the shutdown, which is due to transient release. A higher power would result in more transient fission gas release during and immediately after the shutdown; in this case, fission gas coupling would become more significant.

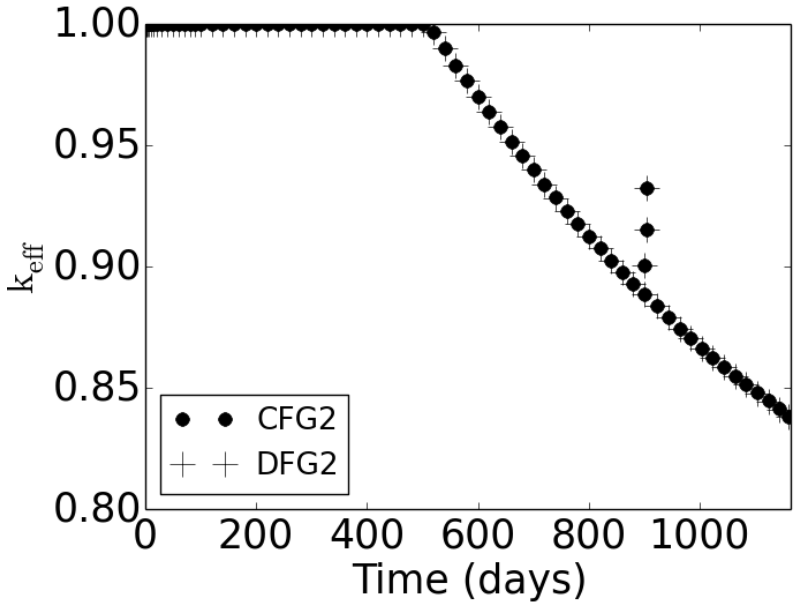

Figure 6.2: The neutron transport eigenvalue (k_{eff}) for the pin array problem, comparing coupled and decoupled fission gas results.

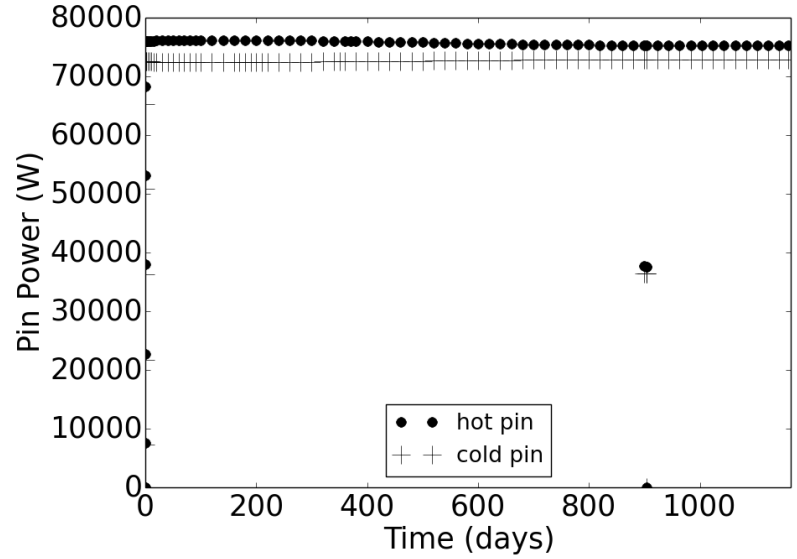

Figure 6.3: This is a comparison of the hottest and coldest pin powers for the pin array simulation; fission gas coupling had an insignificant effect on the pin power distribution.

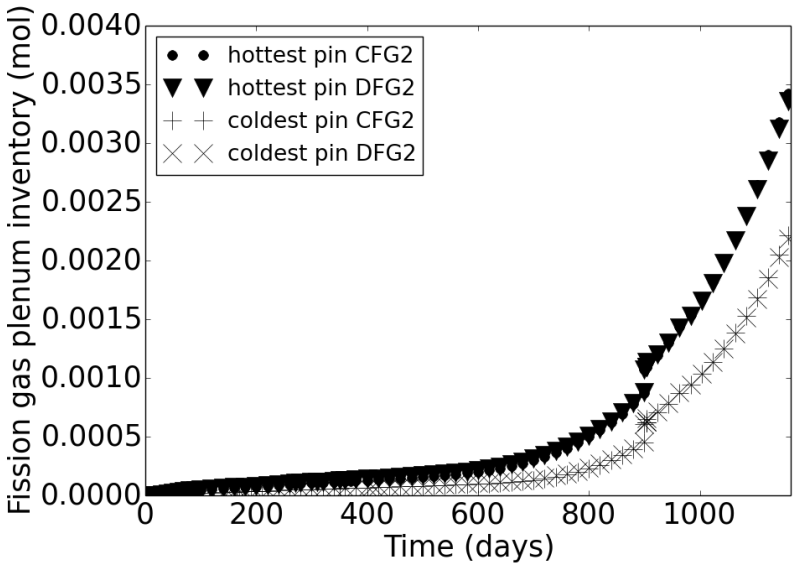

Figure 6.4: This is a comparison between coupled and decoupled fission gas cases of the plenum fission gas inventory for the pin array simulation; results for the hottest and coldest pins are shown.

CHAPTER 7

Conclusions and Future Work

A Conclusions

The objective of this work was to develop and investigate a full-physics, consistent fission gas coupling method using MPACT and BISON; to this end, the MOOSE application Redwing was developed. Redwing was used to perform a series of single- and multi-pin fuel depletion simulations. The results suggest that simulations with loose coupling, including fission gas coupling, can improve the prediction of fission gas behavior and other quantities of interest (i.e. QOIs). A comparison of coupled and decoupled fission gas cases showed that fission gas coupling caused significant differences in the prediction of fission gas released (i.e. FGR) for high-power and high-burnup cases; these differences were likely due to the more accurate fission gas source provided by fission gas coupling. A fissionable nuclide-dependent source was implemented in BISON in order to determine whether improving BISON's fission gas source prediction would result in similar changes in the FGR results. The BISON fissionable nuclide-dependent source was able to improve the agreement in FGR between Redwing and BISON; however, comparison of the codes based on other QOIs were obfuscated by a discrepancy in gap closure near the beginning of life of the fuel. This issue requires further investigation. The changes in BISON QOIs that resulted from implementing the fissionable nuclide-dependent source as well as the simple, adjusted source were similar to changes that resulted from coupling fission gas in Redwing. This shows that the improvement in the fission gas source is an important part of fission gas coupling, and that improvements can be made to the fission gas source prescription for BISON.

Although instabilities are evident in the loosely-coupled Redwing solutions for various scenarios, results suggest that this is a moderate issue, and reducing the Redwing time step results in small improvements. The instablities are not likely the driver for differences caused by fission gas coupling, because coupled and decoupled fission gas cases

have nearly the same L^2-norm of the power density rate-of-change over the course of the simulations. Beside fission gas-related quantities, fission gas coupling also causes significant differences in quantities of interest such as fuel temperature and maximum cladding hoop strain in high-power and high-burnup cases, suggesting that fission gas coupling can improve the accuracy of the overall fuel performance solution. However, validation of Redwing would be needed to determine whether these changes are truly improvements over BISON's predictive capabilities.

There are several more issues with the Redwing models which should be investigated. Cladding lift-off was likely predicted too early; more research is required to determine the specific causes of this. This may be a realistic prediction given the fact that spacer grids are not explicitly modeled in BISON, which would help hold the cladding in place. Also, the time step sensitivity suggests that there is a time-integration error, even at small Redwing time steps of a few days. This is likely due to using loose fission gas coupling along with MPACT's internal depletion solver.

Apart from fission gas coupling, this work highlighted several important aspects of coupled neutron transport and fuel performance simulations of LWR fuel. For one, the time-varying κ, which may be estimated with coupled neutron transport and fuel depletion, has a significant effect on several quantities of interest in high-burnup fuel. Another important physical quantity which may be predicted with neutron transport is the fast neutron flux in the cladding, which can have a large effect on cladding creep rate.

B Future Work

There are several avenues for future modeling and simulation with fission gas coupling. According to BISON's Sifgrs model, a rapid decrease from a high fuel temperature results in a large transient fission gas release; with rapid fission gas release, fission gas coupling would become more significant. Fission gas coupling was only mildly effectual in modeling shutdown in the pin array simulation in Chapter 6, but in that case the pre-shutdown power and temperature were too low to result in significant transient fission gas release. In order to perform higher-power simulations, it is necessary to resolve issues in the fuel pin array model so that the BISON solver is able to handle problems at above 110% power. Two other cases in which fission gas coupling would be more significant are a case with a large amount of fission gas release before gap closure and a case with realistic clad lift-off, so that thermal neutrons streaming from the coolant to the fuel would cause more transmutation of fission gas.

Regarding fission gas coupling at a higher level, a possible next step would be to repli-

cate the coupling scheme in Redwing with other coupled neutron transport and fuel performance software. One of the keys here is to use a separate neutron transport library, which has a large effect on the predicted fission gas behavior. Another near-term step would be to implement tight coupling of MPACT and BISON in Redwing, which should improve the solution stability and the accuracy of quantities of interest.

The fissionable nuclide-dependent fission gas source in BISON requires further investigation; the first step would be to determine the cause of the discrepancy in gap closure between Redwing and BISON; once that is eliminated, a better comparison may be made between Redwing and BISON. Besides a fissionable nuclide-dependent source, a possibility for improving the fission gas released prediction and other QOIs would be to introduce a time-dependent κ value into Sifgrs and the neutron heat source, so the proper relationship between fission rate density and power density are maintained. This would also have an important effect on the fission gas generation; Fig. 4.6 shows that a fixed-κ Redwing simulation predicts up to 5% less fission gas generated compared to a more accurate variable-κ simulation. The time-dependent κ could be entered as an analytic function of time in the BISON input file, or a fissionable nuclide-dependent value could be calculated internally in BISON.

Eventually, before coupled software can be used for predictive simulations for reactor design, it must be validated. The BISON assessment suite could be used for Redwing validation, but first MPACT must be updated so that it can provide the proper neutronics solution for experimental rigs, like the ones that were used in the Risø AN3 and GE7 experiments.

BIBLIOGRAPHY

[1] MPACT Team. MPACT depletion library, August 2008. In MPACT repository: `MPACT/MPACT_Extras/xslibs/MPACT.dpl`.

[2] Japan Atomic Energy Agency. Graph of Fission Product Yields, August 2015. http://wwwndc.jaea.go.jp/cgi-bin/FPYfig.

[3] K. Lassmann, C. O'Carroll, J. van de Laar, and C.T. Walker. The radial distribution of plutonium in high burnup UO_2 fuels. *Journal of Nuclear Materials*, 208:223–231, 1994.

[4] The third Risø fission gas project: Bump test AN3 (CB8-2R), Risø-FGP3-AN3. Technical report, Risø, September 1990.

[5] Andrew T. Godfrey. VERA core physics benchmark progression problem specifications, revision 4. Technical report, Oak Ridge National Laboratory, August 2014.

[6] Han Gyu Joo, Jin Young Cho, Kang Seog Kim, Chung Chan Lee, and Sung Quun Zee. Methods and performance of a three-dimensional whole-core transport code DeCART. In *PHYSOR 2004 - The Physics of Fuel Cycles and Advanced Nuclear Systems: Global Developments*, Chicago, Illinois, April 2004. American Nuclear Society.

[7] MPACT Team. *MPACT VERA User's Manual, Version 2.1.0*. University of Michigan, Ann Arbor, MI, December 2015.

[8] MPACT Team. *MPACT Theory Manual, Version 2.1.0*. University of Michigan, Ann Arbor, MI, December 2015.

[9] Derek R. Gaston, Cody J. Permann, John W. Peterson, Andrew E. Slaughter, David Andrs, Yaqi Wang, Michael P. Short, Danielle M. Perez, Michael R. Tonks, Javier Ortensi, Ling Zou, and Richard C. Martineau. Physics-based multiscale coupling for full core nuclear reactor simulation. *Annals of Nuclear Energy*, 84:45–54, 2015.

[10] John A. Turner, Kevin Clarno, Matt Sieger, Roscoe Bartlett, Benjamin Collins, Roger Pawlowski, Rodney Schmidt, and Randall Summers. The Virtual Environment for Reactor Applications (VERA): Design and architecture. *Journal of Computational Physics*, 326:544–568, 2016.

[11] Benjamin Collins, Shane Stimpson, Blake W. Kelley, Mitchell T.H. Young, Brendan Kochunas, Aaron Graham, Edward W. Larsen, Thomas Downar, and Andrew Godfrey. Stability and accuracy of 3D neutron transport simulations using the 2D/1D method in MPACT. *Journal of Computational Physics*, 326:612–628, 2016.

[12] R.L. Williamson, J.D. Hales, S.R. Novascone, M.R. Tonks, D.R Gaston, C.J. Oermann, and D. Andrs. Multidimensional multiphysics simulation of nuclear fuel behavior. *Journal of Nuclear Materials*, 423:149–163, 2012.

[13] D. Gaston, C. Newman, G. Hansen, and D. Lebrun-Grandi. MOOSE: A parallel computational framework for coupled systems of nonlinear equations. *Nuclear Engineering and Design*, 239(10):1768–1778, October 2009.

[14] J.D. Hales, S.R. Novascone, G. Pastore, D.M. Perez, B.W. Spencer, and R.L. Williamson. *BISON Users Manual, BISON Release 1.2*. Idaho National Laboratory, Idaho Falls, ID, September 2015. INL/MIS-13-30314 Rev. 2.

[15] J.D. Hales, S.R. Novascone, G. Pastore, D.M. Perez, B.W. Spencer, and R.L. Williamson. *BISON Theory Manual: The Equations behind Nuclear Fuel Analysis, BISON Release 1.2*. Idaho National Laboratory, Idaho Falls, ID, September 2015. INL/EXT-13-29930 Rev. 2.

[16] James J. Duderstadt and Louis J. Hamilton. *Nuclear Reactor Analysis*. John Wiley and Sons, 1976.

[17] M. Hursin, B. Kochunas, and T.J. Downar. *DeCART v2.05 Theory Manual*, November 2008.

[18] M.H.A. Piro, J. Banfield, K.T. Clarno, S. Simunovic, T.M Besmann, B.J. Lewis, and W.T. Thompson. Coupled thermochemical, isotopic evolution and heat transfer simulations in highly irradiated UO_2 nuclear fuel. *Journal of Nuclear Materials*, 441:240–251, June 2013.

[19] Giovanni Pastore. *Modeling of Fission Gas Swelling and Release in Oxide Nuclear Fuel and Application to the TRANSURANUS Code*. PhD thesis, Politecnico di Milano, March 2012.

[20] A.E. Isotalo, J. Leppnen, and J. Dufek. Preventing xenon oscillations in Monte Carlo burnup calculations by enforcing equilibrium xenon distribution. *Annals of Nuclear Energy*, 60:78–85, May 2013.

[21] Giovanni Pastore, Lelio Luzzi, valentino Di Marcello, and Paul Van Uffelen. Physics-based modelling of fission gas swelling and release in UO $_2$ applied to integral fuel rod analysis. *Nuclear Engineering and Design*, 256:75–86, 2013.

[22] Y. Rashid, R. Dunham, and R. Montgomery. Fuel analysis and licensing code: FALCONMOD01, volume 1: Theoretical and numerical bases, technical report EPRI 1011307. Technical report, Electric Power Research Institute, 2004.

[23] K. Forsberg and A.R. Massih. Diffusion theory of fission gas migration in irradiated nuclear fuel UO $_2$. *Journal of Nuclear Materials*, 135:140–148, May 1985.

[24] R.J.White and M.O.Tucker. A new fission-gas release model. *Journal of Nuclear Materials*, 118:1–38, April 1983.

[25] D. E. Cullen. Application of the probability table method to multigroup calculations in neutron transport. *Nuclear Science and Engineering*, 55:387, 1974.

[26] F. Gleicher, M. Rose, B.W. Spencer, S.R. Novascone, R.L. Williamson, R. Martineau, T. Downar, and B. Collins. Coupling the core analysis program DeCART to the fuel performance application BISON. In *Proceedings of the International Conference on Mathematics and Computational Methods Applied to Nuclear Science and Engineering*, Sun Valley, ID, May 2013. American Nuclear Society. CD-ROM.

[27] D.D. Lanning, C.E. Beyer, and C.L. Painter. FRAPCON-3: Modifications to fuel rod material properties and performance models for high-burnup application (NUREG/CR-6534 volume 1). Technical Report PNNL-11513, Pacific Northwest National Laboratory, October 1997.

[28] Standard review plan for the review of safety analysis reports for nuclear power plants: LWR edition (NUREG-0800, formerly issued as NUREG-75/087). Technical report, Nuclear Regulatory Commission, 2016.

[29] MOOSE Team. MOOSE Framework public website, July 2014. www.mooseframework.org.

[30] R. E. Alcouffe, E. W. Larsen, W. F. Miller Jr, and B. R. Wienke. Computational efficiency of numerical methods for the multigroup, discrete-ordinates neutron transport equations: The slab geometry case. *Nuclear Science and Engineering*, 71(2):111–127, 1979.

[31] D.A. Knoll and D.E. Keyes. Jacobian-free newton-krylov methods: a survey of approaches and applications. *Journal of Computational Physics*, 193:357–397, 2004.

[32] MOOSE Team. MOOSE Framework: `LayeredAverage` class reference, June 2015. http://www.mooseframework.org/docs/doxygen/moose/classLayeredAverage.html.

[33] MOOSE Team. MOOSE Systems: `MutliApps` class reference, November 2016. http://mooseframework.org/wiki/MooseSystems/MultiApps/.

[34] Wolfgang Wiesenack, Terje Tverberg, Margaret McGrath, Erik Kolstad, and Stephan Beguin. Rod overpressure/lift-off testing at halden in-pile data and analysis. *Nuclear Science and Technology*, 43(9):1037–1044, 2006.

[35] MPACT Team. MPACT 47-group transport library v4.1m3, March 2015. In MPACT repository: `MPACT/MPACT_Extras/xslibs/mpact47g_71s_v4.1m3_03192015.fmt`.